



PONTIFICIA UNIVERSIDAD CATOLICA DE CHILE
ESCUELA DE INGENIERIA

C_n^2 PROFILER FOR A MULTI- CONJUGATED ADAPTIVE OPTICS SYSTEM

ANGELA JOHANNA CORTÉS CARVALLO

Thesis submitted to the Office of Research and Graduate Studies in partial fulfillment of the requirements for the Degree of Doctor in Engineering Sciences

Advisor:

ANDRÉS GUESALAGA MEISSNER.

Santiago de Chile, August, 2014

© XXIV, Angela Johanna Cortés Carvallo



PONTIFICIA UNIVERSIDAD CATOLICA DE CHILE
ESCUELA DE INGENIERIA

C_n^2 PROFILER FOR A MULTI-CONJUGATED ADAPTIVE OPTICS SYSTEM

ANGELA JOHANNA CORTÉS CARVALLO

Members of the Committee:

ANDRÉS GUESALAGA M.

MIGUEL ATILLIO TORRES T.

CRISTIAN RODRIGO ESCAURIAZA M.

MICHEL CURÉ O.

CRISTIAN VIAL E.

BENOIT NEICHEL

Thesis submitted to the Office of Research and Graduate Studies in partial fulfillment of the requirements for the Degree of Doctor in Engineering Sciences

Santiago de Chile, August, 2014

© XXIV, Angela Johanna Cortés Carvallo

A Pierre Haguenuer

ACKNOWLEDGEMENTS

According to an apocryphal story
Werner Heisenberg was asked what he would
ask God, given the opportunity. His reply was:
"When I meet God, I am going to ask him two questions:
Why relativity? And why turbulence?
I really believe he will have an answer for the first."

Este trabajo ha sido posible gracias a la colaboración de muchas personas, lo cual es injusto de acotar en algunas palabras, ya que el espacio es finito y la memoria frágil, pero espero haber podido demostrar, sino en palabras aquí, pero en mi corazón y ojalá en persona.

Sin embargo, a quien debo mencionar en primer lugar, es a mi profesor supervisor, Andrés Guesalaga, quien no solo me aceptó sin conocerme, sino que fue un mentor y guía, fue quien creyó en mí, mas de lo que yo creía, y que además ha sido un ejemplo como persona y como profesional.

También debo agradecer a mi pareja, esposo y el amor de mi vida, quien no solo fue un constante apoyo, sino que fue quien estuvo de acuerdo en un principio, cuando decidí embarcarme en esta odisea, dándome cada día ánimo y aliento. A la posibilidad que me dieron en mi ex-trabajo, gracias a Andreas Kaufer que además del apoyo, me dio alguno que otro consejo, a Benoit Neichel quien acepto a que trabajara con ellos.

Tampoco habría sido esto posible sin el apoyo de CONICYT, que consideraron que era apta y me otorgaron una beca. También agradezco a la gente de Durham, principalmente a Richard Myers y Tim Morris, que además de tenerme paciencia, y enseñarme muchas cosas, me acogieron e hicieron sentir integrada al equipo y me enseñaron como funciona un gran equipo de gente que hace investigación. Otras personas que me apoyaron en cuanto a comentarios y guías, agradezco a Andrei Tokovinin, Tim Butterley, James Osborne, Richard Wilson, Dani Guzman.

Lo mejor, fueron los viajes a los observatorios de Chile, incluido Santa Martina, donde me mori de frio, el viaje a la nieve que nunca hicimos.

Les agradezco a mis amigos que fueron parte de este camino, Israel Blanchard, Nicole David, Aglae Kellerer, James. A las infinitas tardes de alineación de la mesa óptica con Nicole, los infinitos coffee-breaks, a la música, y a mi autor favorito, Haruki Murakami.

Y finalmente, quiero agradecerle a mi abuela, Ana Contreras, que sin ella, quizás que no habría llegado hasta donde estoy, fue su apoyo constante y amor quien me han convertido en una sobreviviente.

TABLE OF CONTENTS

	Pág.
DEDICATORIA	ii
Acknowledgements.....	iii
List of tables.....	vi
List of figures.....	vii
RESUMEN	xii
ABSTRACT.....	xiii
1. Introduction.....	14
1.1 Motivation.....	14
1.2 Project Description.....	17
1.2.1 General Objectives	17
1.2.2 Specific Objectives.....	17
1.2.3 Synopsis.....	18
2. Theory.....	19
2.1 Atmospheric Turbulence.....	21
2.1.1 Kolmogorov Turbulence	23
2.1.2 Von Karman Turbulence	26
2.1.3 Seeing and atmospheric parameters	27
2.1.4 Inner Scale and Outer Scale.....	29
2.2 Frozen Flow Hypothesis	30
2.3 Correcting for the effect of the atmosphere: Adaptive Optics (AO).....	34
2.3.1 History	34
2.3.2 Definition and components.....	36
2.3.3 The Single Conjugated Adaptive Optics (SCAO).....	41
2.3.4 Multi-Conjugated Adaptive Optics (MCAO).....	42
2.3.5 Ground Layer Adaptive Optics (GLAO).....	44
2.3.6 Multi-Object Adaptive Optics (MOAO)	45
2.3.7 Laser Tomography Adaptive Optics (LTAO).....	46

2.3.8	Extreme AO (ExAO)	46
2.4	Instruments to measure the atmospheric turbulence	47
2.4.1	Differential image motion monitor (DIMM)	47
2.3.9	Multi-aperture scintillation sensor (MASS)	48
2.3.10	The lunar scintillation system (LUSCI)	50
2.3.11	Scintillation detection and ranging (SCIDAR)	51
2.3.12	Slope detection and ranging (SLODAR)	54
3.	GeMS and the adapted SLODAR	57
3.1	GeMS Instrument Description	57
3.2	Data Format	63
3.3	The SLODAR approach modified for multiple LGS	66
4.	Simulations	71
4.1	Simulating the turbulence	71
4.2	Simulating the WFS of GeMS	74
5.	The method: SLODAR for MCAO with multiple LGSs	76
5.1	Estimating the Cn2 in altitude (turbulence profiling)	81
5.2	Absolute profile	84
5.1	The unsensed turbulence	85
6.	Wind Profiler	88
7.	Calibrations	92
5.2.1	Deformable Mirror and quadcell	92
8.	Data analysis	98
8.1	Results and discussion	105
8.2	Good and bad profiles	106
8.3	Validation of the techniques	107
9.	Conclusions and Future Work	111
	BIBLIOGRAPHY	114

LIST OF TABLES

	Pág.
Table 1: Deformable mirrors characteristics.....	61
Table 2: Altitude of the sampling and number of overlapping subapertures. The first overlap corresponds to the subapertures without masking, and then the overlaps corresponding between two in the edges (WFS1-4), and then overlap between the center and the edge (WFS1-0).	70
Table 3: Main parameters used for modeling the GeMS telescope.	71

LIST OF FIGURES

	Pág.
Figure 1-1: Images of IO (Jupiter’s satellite). Left: image taken by Keck without AO; middle: image taken by Keck with AO (K-band); right: image (visible light) taken with Galileo spacecraft orbiter.....	15
Figure 2-1: Turbulence generated by the wind and the hill. The structure of the dome also interferes increasing the wind flow over the telescope.....	20
Figure 2-2: Development of the turbulence from the injection of the energy until the dissipation into heat. Re_L : Large Reynold number.	24
Figure 2-3: Typical Cn2 Turbulence profile measured at La Palma (García-Lorenzo & Fuensalida, 2011).....	25
Figure 2-4: Spatial frequency for the different models of turbulence, Kolmogorov, Von Karman and Tatarskii.....	27
Figure 2-5: Isoplanatic angle is the maximum angular separation of two stars that shares almost the same turbulence.....	29
Figure 2-6: Shack Hartmann WFS diagram. The wavefront is measured by the small area of each subaperture of the lenslet. When the wavefront is plane (undistorted), each lenslet forms a spot on the detector, and all of them will form a regular grid of spots. But when the wavefront is distorted, the lenslet will create a spot a bit displaced from its original position and this provides a measure of the local wavefront.....	37
Figure 2-7: A quadcell consists of four photodiodes. An inconvenient of such a cell is that the precision in the centering depends on the spot size, and it is thus affected by the seeing, and the sodium layer in our case.....	38
Figure 2-8: Two types of DM’s, one (left) corresponds to a single thin surface, that can be modeled to the desired shape by the actuators, and the other (right) corresponds to a segmented mirror (3 actuators per segment) where the actuators control the position (piston, tip and tilt) of the each small section of the full mirror.	39
Figure 2-9: The cone effect refers to the different turbulence sampled by a NGS and a LGS. Here the two areas in red are not sampled by the LGS.	41
Figure 2-10: Diagram of an Adaptive Optic (AO) System. The light from the source is first reflected by the DM and then split between the scientific camera and the WFS. The WFS measures the atmospheric distortions and the control system sends the corrections to shape the DM.	42
Figure 2-11: Comparison between a field of stars: without correction (left), corrected only in one direction (center) and with large field MCAO correction (right). As shown in the central image, the correction is successful over the limited central patch around the single guide star.	43
Figure 2-12: Example of MCAO Field, showing how different WFS sample different atmospheric volumes. At ground layer all WFSs sample the same ground-layer turbulence, at mid-altitude the common areas decrease and eventually vanishes at high altitude. 1,2 and 3 are different GS on the sky.....	43

Figure 2-13: MCAO design. The distortions are measured on several GS along different directions, the turbulence is tomographically reconstructed and the distortions are then corrected by several DMs conjugated to different altitudes.	44
Figure 2-14: GLAO diagram, using several WFS but only one DM that is conjugated to the ground layer turbulence, which is generally the dominant layer.	45
Figure 2-15: MOAO is similar to having several SCAO systems across the field (one per DM), but it works in open loop and estimates by tomographic reconstruction the turbulence along the direction corrected by the DM.	46
Figure 2-16: DIMM optical scheme. (Sarazin & Roddier, 1990).....	48
Figure 2-17: MASS instrument concept.	49
Figure 2-18: Simplified optical diagram of MASS detector.....	50
Figure 2-19: The principle of LuSci. Diagram adapted from Tokovinin’s paper (A Tokovinin, Bustos, & Berdja, 2010).....	51
Figure 2-20: Schematic principle of SCIDAR.....	52
Figure 2-21: SLODAR principle (L. Wang, 2007). It samples the wavefront of two NGS. Top: there is only one layer of turbulence, and the offset is determined by cross-correlating the two wavefront measurements, as the displacement of the peak will determine the altitude of the layer. Bottom: Shows how the same principle works with two layers of turbulence, the cross-correlation will have as many peaks as layers of turbulence, and they will move away from the center, for higher altitudes.....	55
Figure 3-1: Gemini Telescopes. Left: Gemini North, at Mauna Kea (4213 m), Right: Gemini South at Cerro Pachón (2722 m altitude) (Pictures from Gemini website). ...	57
Figure 3-2: GeMS and CANOPUS, simplified diagram. The telescope observes three NGS and 5 LGS, and sends the light to CANOPUS. It uses 3 DMs to correct over a FoV of 60 arcseconds. The corrected wavefront is fed to two instruments (Flamingos2 or GSAOI).....	58
Figure 3-3: 3-D diagram of CANOPUS. The light path from the telescope to the instrument is shown as white, with the light sent to the LGS-WFS (orange) and the NGS-WFS. The red beam corresponds to the scientific image that goes to the instrument. Image from GeMS website.	59
Figure 3-4: Layout of the DMs, black crosses show valid actuators, blue crosses show slave actuators (top: DM0; center: DM4.5; bottom: DM9). From the Gemini website (http://www.gemini.edu/?q=node/11751).....	62
Figure 3-5: Left: Asterism on sky of the 5 LGS. Right: WFS geometry, the red are the 204 valid subapertures.	63
Figure 3-6: Generic WFS-i, the slopes are separated in x and y, the blue squared are the 240 valid subapertures.	65
Figure 3-7: Distribution of the layers in the modified SLODAR, using LGS. N is the number of subapertures.....	66
Figure 3-8: Angular separations at GeMS. The red arrows correspond to the high resolution, and the blue arrows correspond to the low resolution. The arrows indicate the different baselines, the blue arrows correspond to the shorter baseline and the red, the larger baseline.	68

Figure 3-9: Fratricide effect. The yellow lines are the LGS beams, and the red subapertures are the contaminated subapertures on each WFS.	69
Figure 3-10: Masks defined for each WFS, to eliminate the problematic subapertures. From left to right: M-WFS1, M-WFS2, M- WFS0, M-WFS4 and M-WFS3. Masking reduces the valid subapertures from 204x5 to 640.	69
Figure 4-1: Phase Screen generated using the Kolmogorov PSD (left) and the phase in 3D (right).	72
Figure 4-2: Von Karman phase screen (left) and the phase in 3D (right). $L_0=125$ m.	73
Figure 4-3: Ground layer turbulence (layer 0). Left: the full phase screen, the red square is the sampled area for one frame. Middle: the metapupil for the ground layer, i.e. only the pupil had all WFS are looking at the same area. Right: WFS0.	73
Figure 4-4: High layer turbulence (layer 11). Left: full phase screen, the red square is the sampled area for one frame. Middle: the metapupil, here in blue are the 5 squares corresponding to each WFS. Right: WFS0 corresponding to the center blue square. .	74
Figure 4-5: Fried Geometry, where the arrows are the slope measurements, and points represent the grid.....	75
Figure 5-1: Cross-correlation of the measured slopes, for layer 4. The slopes are sorted like X0,X1,X2,X3,X4,Y0,Y1,Y2,Y3,Y4 (see Figure 3-6). The diagonal line corresponds to the autocorrelation. It can also be seen that the image is conformed by four squares, the first left-top correspond to the cross-correlation between X-X (WFS1-5), the right-top correspond to the cross-correlation between X-Y, the left-bottom correspond to the cross-correlation between Y-X, and finally the right-bottom correspond to the cross-correlation between YY.....	77
Figure 5-2: Covariance matrix for layer 7. The relevant data in the technique correlation between measurements on the same axis (X with X, and Y with Y). This symmetrical matrix contains 10x10 submaps. The diagonal correspond to autocorrelations for each of the five WFSs	78
Figure 5-3: Covariance map corresponding to Y1-Y2 (red squared submap on previous figure), beginning with layer 0 in the top-left corner and ending with layer 15 in the bottom-right corner.	80
Figure 5-4: A section of the same submap Y1-Y2 from Figure 5-3, all superimposed. A decrease in the maximum intensity is observed for upper layer together with a displacement from the center.	81
Figure 5-5: At the left is the submap M0,10sim, and at the right, the submap M6,10sim.	82
Figure 5-6: Fitting of the data on-sky, corresponding to March 25, 2011 at 06:36:59.....	84
Figure 5-7: Autocovariance submap cross-section, X direction. Theoretical versus measured.	86
Figure 6-1: Variance of a data set, X values at the top, Y values at the bottom. The white area correspond to “hot” spots, and due are presented in all WFSs, this would be due turbulence at the ground layer.....	90
Figure 6-2: Turbulence generated by the DM independently and the profile obtained with the wind profile method. Here it can be seen that the spot of the correlation peak is broader for the DM9 than in the others, affecting the profile measurement. Left: DM0, middle: DM45, right: DM9.....	91

Figure 6-3: Estimation of the turbulence altitude and direction and velocity of the wind. .	91
Figure 7-1: Fitting works perfectly for simulated data.	92
Figure 7-2: Estimated profile using the calibration source and excitation of DM at 4.5 km	93
Figure 7-3: Result of the wind profiler for a turbulence generated at DM4.5 with a wind speed of 30 ms^{-1} in the X direction.	93
Figure 7-4: Open loop versus POL. The thin line is the ideal relationship that should be obtained; the thick line is a fourth-order polynomial fit to the data (dot cloud). Left- hand panel: WFS0 subaperture 1; right-hand panel: WFS1, subaperture 57.....	95
Figure 7-5: Left: Covariance map for exciting the DM0, right: Theoretical covariance map for layer 0.	96
Figure 7-6: Left: Covariance map for exciting the DM9, right: Theoretical covariance map for layer 6.	97
Figure 7-7: Profiles obtained (blue) when the turbulence was introduced by each DM (red dashed line) independently. First altitude average was 636m for the DM located at 0km, second was 4.477km for the DM located at 4.5 km, and the third was 9.242 km for the DM located at 9km.	97
Figure 8-1: Standard deviation of the WFS2 (left) and WFS0 (right). The low values correspond to the fratricide effect, that is saturated, and the high values correspond to the subapertures that are partially illuminated.	98
Figure 8-2: The 5 WFS subaperture intensity in presence of clouds. (Rigaut & Neichel, 2011).	99
Figure 8-3: Two examples of sub-aperture slopes, top: a good set of data; bottom: a bad example of data set with high variance.	100
Figure 8-4: Right: Wind Profiler results, for baseline WFS1&2 and WFS4&3 (High Resolution). Left and center: temporal cross-correlation for $t=0\text{s}$, and for $t=40\text{s}$	100
Figure 8-5: Right Wind Profiler results, for baseline WFS0&2 and WFS4&0 (Low Resolution). Left and center: temporal cross-correlation for $t=0\text{s}$, and $t=25\text{s}$	101
Figure 8-6: Top: Covariance submap section, where the non-Kolmogorov shape can be seen. Files observed on: (left) Nov 28 th 2011 at 11:44, (middle) Dec 13 th 2011 at 00:30 and (right) Dec 14 th 2011 at 00:01. Bottom: zoom of the same data.	102
Figure 8-7: Top: Covariance submap section, where the non-Kolmogorov shape can be seen. This generated a problem for the fit, creating some negative values in the layers profile to compensate for this weird shape. Files observed on: (left) Dec 14 th 2011 at 04:35, (middle) Dec 14 th 2011 at 23:59 and (right) Feb 10 th 2012 at 20:53. Bottom: zoom of the same data.	102
Figure 8-8: Examples of good profiles. When the covariance submap had this shape, the wind profiler had no problems finding a good fit. For these cases, we can say that the turbulence follows a Kolmogorov model.	103
Figure 8-9: Different covariance maps, left corresponds to a normal map, the one in the center shows a very high value at the center that represent strong noise, and the one at the right presents a problem with the WFS4 (bottom left corner).	104

Figure 8-10: Left: Fitting of on-sky data from March 23 rd 2011 at 02:26, CB close loop. Right: Fitting of on-sky data from March 27 th 2011 at 01:02, best on-sky set. The values on the x axis correspond to the number of the layer.....	104
Figure 8-11: Good Profile example: here we have a strong turbulence in the ground layers that decay rapidly with the altitude giving a Fried parameter of 11.4 cm.	105
Figure 8-12: Left: central slice of the theoretical and measured submap X direction. Right: Estimated profile. RTD data, Jan 12 th 2012 – 03:10:43.....	105
Figure 8-13: Left: central slice of the theoretical and measured submap X direction. Right: Estimated profile (good measurement here). RTD data, Jan 12 th 2012 at 03:12:30..	106
Figure 8-14: Left: central slice of the theoretical and measured submap X direction. Right: Estimated profile (good measurement here). CB data, Jan 12 th 2012 at 00:12:27. ...	106
Figure 8-15: Weird data, observed on November 15 th 2011 at 20:29. Left: Cross section of the autocovariance submap, Right: Obtained profile.....	107
Figure 8-16: Gemini Telescope pointing in one direction (orange line), and MASS/DIMM pointing in another direction (blue line), showing how different the sampled turbulence could be, even being at close location.....	108
Figure 8-17: Comparison between MASS/DIM accumulative profile and spatial cross-correlation High Resolution accumulative profile. They show a good agreement at lower layers. But it is important to mention that they were observing different stars on sky. Data from April 15th, 2011, 23:55.	109
Figure 8-18: Comparison between the profiler obtained with the SLODAR method (left), and obtained with the Wind Profiler (right).....	110

RESUMEN

Esta tesis presenta un método pionero e innovador para la medición de la distribución vertical del perfil de turbulencias atmosférica, en sistema de óptica adaptativa de campo amplio. Con la capacidad de proporcionar en tiempo real las mediciones para instrumentos de óptica adaptativa (OA), durante las observaciones astronómicas.

La OA nos permite compensar los efectos negativos que tiene la turbulencia de la atmosfera sobre la calidad y la resolución de las imagines tomadas para astronomía. Hoy en día, se ha optado por aumentar el tamaño de los telescopios ópticos para poder cumplir con los objetivos científicos y la OA ha desarrollado importantes nuevos avances.

Mientras que el perfil de turbulencias no es algo nuevo, los sistemas desarrollados no proporcionan toda la información requerida por la ciencia, ya que se encuentran en un telescopio separado y por ende, independiente del instrumento de OA.

El objetivo de esta nueva técnica es usar directamente los datos ya observados de un sistema de OA multi-conjugado, de modo de medir directamente la turbulencia que afecta al telescopio usado para la ciencia, sin la necesidad de un sistema externo. Además puede ser usada para la evaluación misma del sistema de OA y además se descubrió que nos permite la estimación de la intensidad del “*seeing*” dentro de la cúpula del telescopio.

El método es la adaptación de una técnica conocida (SLODAR) para la medición del perfil vertical de turbulencia, pero en lugar de usar estrellas naturales, usa estrellas generadas con un láser. En principio se simularon datos para validar el perfil reconstruido y que nos permitiera identificar los parámetros importantes. El método fue primero implementado y calibrado en el sistema multi-conjugado de Gemini sur (GeMS), para ser finalmente validado con los datos tomados de observaciones reales en el cielo. El método encontró algunos factores limitantes, como el efecto “*fratricida*” proveniente de la dispersión del laser en la atmosfera y de la existencia del “*seeing*” presente en la cúpula, pero ambos efectos fueron identificados y mitigados.

En una segunda aproximación para la reconstrucción del perfil, fue la implementación de técnicas de correlaciones temporal, llamada “*perfil del viento*”, la que nos proporciono, no solo el perfil vertical de turbulencias, sino que proporciona la dirección y velocidad del viento para cada capa, proporcionando un mayor desempeño ya que se ajusta automáticamente a la turbulencia, y condiciones como cambios de la escala externa (“*outer scale*”), ruido del sensor de frente de onda o la fuerza de la turbulencia no le afecta.

Mejoras futuras de la técnica desarrollada, podrían beneficiar métodos de control predictivo, al compensar del los retrasos inherentes al ciclo de OA, al proporcionar información de velocidad y dirección del viento.

Esta técnica fue inicialmente desarrollada para GeMS, pero es en la actualidad probada en al menos otros tres instrumentos del mejor nivel,

Palabras Claves: Óptica Adaptativa, Perfil de turbulencia, Multi-Conjugated Adaptive Optics (MCAO), Evaluación de sitios, Cn2, SLODAR.

ABSTRACT

This thesis presents an innovative and pioneering method for measuring the vertical profile of the atmospheric turbulence in wide field adaptive optics (AO). It is meant to provide real time information for AO instruments during scientific astronomical observations.

AO allows for compensating the negative effects of the turbulence on the quality and resolution of the images. Today, with the ever-growing size of the telescopes in the optical domain, important technology developments are done in new AO techniques.

While atmosphere profiling is not new, the numerous systems developed until now provide only part of the required information, and are generally separated from the telescope and AO instruments. This innovative technique aims at using the data from a multi-conjugate AO system directly, sensing the same part of the atmosphere that the telescope sees without the need for an additional external probing system. It can also be used to evaluate the performance of the AO system and was found that also allows to the estimation of the dome seeing strength.

The method adapts a well known technique (SLODAR) to measure the vertical profile using laser guide stars instead of bright natural binary stars. Using simulated data, allowed us to validate the profile reconstruction and identifying the important parameters. The method implementation and calibration on the Gemini south multi-conjugate system (GeMS) is the first step, before a complete validation with on-sky data. The limiting factors of the method, like fratricide effects from laser beam scattering and the existence of dome seeing, are identified and mitigated.

A second approach used to solve the profiling method, was the implementation of a temporal cross-correlation technique called “wind profiler”, that provides not only the turbulence profile but also the wind direction and speed for each layer, giving a better performance as it self-adjusts to turbulence conditions such as changing outer scales, wavefront sensor noise and turbulence strength.

Future upgrades of the technique could benefit from the information of the wind speed and direction, by specifically implementing predictive control methods that compensate for the delays inherent to AO loops.

This technique initially developed for GeMS, is now being tested for its use in at least three other world class telescopes.

Keywords: Adaptive Optics, Turbulence profiler, Multi-Conjugated Adaptive Optics (MCAO), Site Testing, Cn2, SLODAR.

1. INTRODUCTION

For centuries, humanity has been contemplating the skies, watching the stars and trying to unravel their mysteries, studying the trajectory of the planets, and observing their moons. With each technology development, we have been able to get our knowledge further and deeper, step by step, trying to understand one of the most marvelous mystery of all: where do we come from, how did the universe starts, and maybe answering the philosophical question on why are we here.

1.1 Motivation

In the last decade, astronomy, and specifically telescope design have reached a dead end. The will to see always further and with always a better resolution, has required to keep increasing the size of the collecting area (primary mirror) in the telescopes designs. But soon it was found that the resolving power of the ground based telescopes in the visible and near infrared spectra was limited because of the effects of the atmospheric turbulence. With bigger telescopes, one could gather more photons, but the resolution was not following what optics theory had promised.

Adaptive Optics (AO) systems were thus developed, with the purpose of correcting the effect of turbulence that causes wavefront distortions of the light of the stars when propagating through the Earth's atmosphere. Sending the telescope in space to avoid the atmosphere is one way to overcome the limits brought by the turbulence, but the cost and technical difficulties of this option has motivated the research for systems that can correct the effect of the atmosphere for ground telescopes. The Hubble Space Telescope (HST) initial cost was around 2.5 billion USD (Lallo, 2012). But after having been placed in orbit around the Earth on April 25th, 1990 (STS-31), it was found that the telescope was suffering from spherical aberration from its primary mirror. The outer edges

were around $2\ \mu\text{m}$ too flat, a quarter of an average human hair (ESA, n.d.). To fix this, another space mission became necessary, and was launched in 1993 (STS-61). It consisted in installing a set of mirrors, called COSTAR (for “Corrective Optics Space Telescope Axial Replacement”). In comparison, the Very Large Telescope (VLT) project had an estimated cost of 450 million USD (ESO, n.d.). This means that for a quarter of the cost of one telescope of 2.4-m in space, one could get four 8-m telescopes and four smaller 1.8-m telescopes on Earth. And the difference between the investments in space and ground is not reducing for the new astronomy projects: the estimated cost for a 40-m ground telescope is 1.2 billion USD, and the cost for the 6.5-m James Webb Space Telescope is 8 billions USD (Ashcroft, 2013).

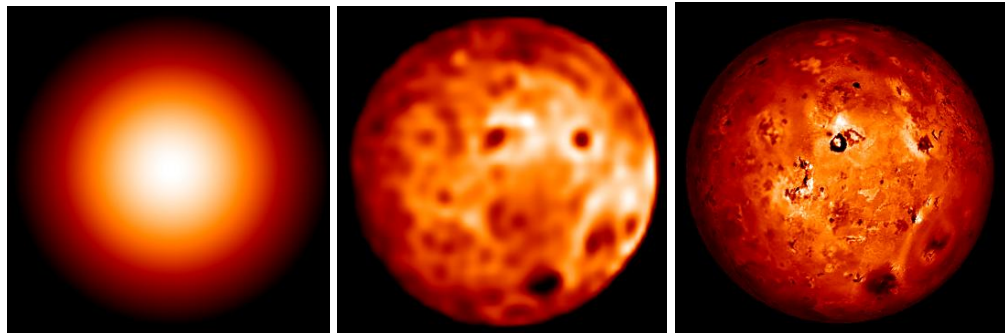


Figure 1-1: Images of IO (Jupiter’s satellite). Left: image taken by Keck without AO; middle: image taken by Keck with AO (K-band); right: image (visible light) taken with Galileo spacecraft orbiter.

Now that we have understood why we have to observe the space from the Earth, it also becomes obvious that it was necessary to understand and solve the problem of observing the space through the atmosphere. Figure 1-1 illustrates the problem with images of the IO satellite taken with different methods and telescopes, showing the evident advantage of correcting the turbulence effect allowing to recover details that could normally only be seen from space (provided that the same resolution is available).

Understanding the behavior of the atmosphere has always been a big puzzle for people studying turbulent fluids, either for weather forecast or aircraft design. In the astronomy field, we do not need a prediction for days in advance, we just need to measure the actual distortion and correct its impact as fast as possible.

In the search for the best places to install the telescopes on Earth, the researchers have designed instruments to measure the intensity of the distortions from the atmosphere. And in the recent years, this field has become more and more important, as we are entering in the era of what we know as Extremely Large Telescopes (ELTs, size above 30 meters for the primary mirror); the knowledge of the distribution of the turbulence in the atmosphere will be absolutely necessary to reach the expected performances.

Nowadays, when the biggest telescopes are of the 8-meter class, we are still using only small telescopes to measure the turbulence (25 cm MASS-DIMM in Tololo, and 35 cm MASS-DIMM in Paranal), giving thus a smaller resolution when sampling the turbulence (because they are a dedicated and small telescope, to reduce cost).

The work presented here proposes a different way to use the existing technology, applying previous works on turbulence measurement, and extending the theory beyond these instruments to sample the turbulence with a better resolution and at no extra cost. At the moment this thesis is written, there is only one telescope in operation in the whole world that provides 5 lasers and a primary mirror of 8 meters, and is located in the Gemini South Observatory, near La Serena, Chile. Similar technology is being developed for the VLT at Paranal Observatory, with an implementation soon to be started. Understanding and monitoring the behavior of the turbulence will be a key for the design of the future ELTs, and knowing the profile of the atmosphere layers is needed to design and dimension the future instruments.

1.2 Project Description

The work presented in this thesis has been done in collaboration with the Gemini South Observatory. The work was divided in three main parts, starting first with research on the method to be used to measure the turbulence together with the related theory; the second part consisted in adapting the theory to the data available from the telescope; and third, validating the method through the analysis of the data obtained.

1.2.1 General Objectives

This research is focused on developing an algorithm that allows determining the strength of the turbulence at different altitudes, using measurements made with laser guide stars.

1.2.2 Specific Objectives

The following objectives were set for the research topics developed in this thesis:

- Study and implement an algorithm that estimate slopes for turbulences at different altitudes.
- Develop a model for turbulence and implement it the Gemini multi-conjugate adaptive optics system (GeMS).
- Process bench calibration data and on-sky data gathered from the GeMS facility instrument.
- Analyze real data obtained on sky with the instrument GeMS.
- Perform statistical analysis on the data if possible.

1.2.3 Synopsis

In chapter 2, the theoretical background on adaptive optics and turbulence estimation are presented together with the existing instruments related to turbulence profiling, so that the reader can understand the work done.

In chapter 3, the focus is explaining the GeMS instrument facility, which provided this research with data to work on, and review the SLODAR technique, used as basis for the implementation of the work. It is also presented what was necessary to be modified from the SLODAR method, in order to use it with laser guide stars, instead of natural guide stars.

Chapter 4 contains the simulations developed during the work, and the method developed to measure the turbulence profile from the data obtained with GeMS.

Chapter 5 explains another method, the wind profiler, also tested with the GeMS data, used as a comparative method.

Chapter 6 and 7 containing the data analysis, discussion and conclusions of the thesis.

2. THEORY

In the imaging process, the light from the object (or the light reflected by the object) must travel along a path from its origin to the eye or detector. The optics rules of refraction and reflection of the light (electromagnetic waves) are needed in order to explain how an image is formed and predict its characteristic.

When observing the stars from the Earth, their light has to cross the entire atmosphere to reach us, and the atmosphere consists of a mixture of gases. The energy reaching the atmosphere comes primarily from the Sun, though interactions with the land and the ocean are also important (David G. Andrews, 2010), see Figure 2-1.

The atmosphere is generally close to hydrostatic balance in the vertical direction, except on small scales. It means that it can be divided in levels that are supported by difference in pressure between their lower and upper surfaces. And the gravity will produce density stratification in the atmosphere. The thermodynamic principles are essential for describing many of the atmospheric process, and the kinetic theory of gases will explain the transfer of momentum by molecules. For bigger motions we can use the dynamical process, considering the atmosphere as a continuous fluid. Movements on a very big scale, like Coriolis effect, can be explained by the rotation of the earth.

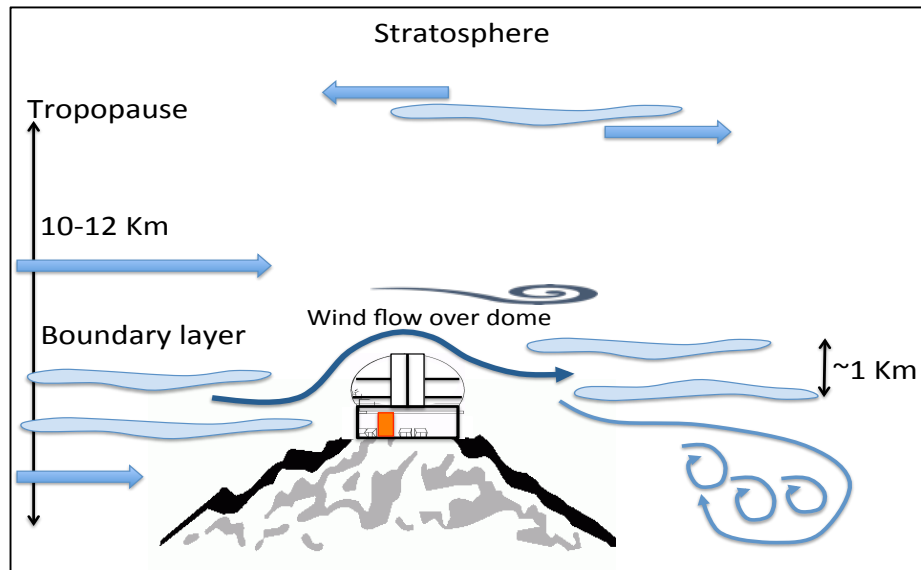


Figure 2-1: Turbulence generated by the wind and the hill. The structure of the dome also interferes increasing the wind flow over the telescope.

The atmospheric turbulence had mainly two big impacts in astronomy. One is due to the absorption of light by the atmospheric gases, which defines certain windows for the possible observing wavelengths. The second main problem, when studying the stars from the Earth, is the effect on the light from the observed object when travelling through the atmosphere, reducing the angular resolution given by the telescope (which is not anymore diffraction limited¹). The variations of refraction index will change the direction of the light.

A brief resume of the concepts, together with models and hypothesis related to the dynamics of the atmosphere will be presented in this chapter.

The refraction index of air depends on the ambient air pressure, temperature, humidity, carbon dioxide level, and air dust density (Owens, 1967). Moreover, the condition of the air in the atmosphere is not homogeneous. An increase in temperature at a land surface, which receives direct sunlight, causes a non-uniform temperature distribution above the ground. Then, temperature distribution generates air convection, which makes the distribution unsteady.

¹ The diffraction limit is the ultimate angular resolution limit imposed by the laws of optics and is equal to the ratio of the observing wavelength to the telescope diameter.

Refraction of light occurs at a border between two different materials. The light will travel on a curved line in a medium like air, which changes its relative refraction index non-uniformly and continuously. The atmosphere moves by convection or wind, which changes the curved line along with the movement of the air (Shimizu, Yoshimura, Tanaka, & Okutomi, 2008).

As the appearance of the image depends strongly on the aperture of the telescope, in a small pupil the effect is not perceived. In a larger aperture however the effect of the atmospheric turbulence will spread and blur the image. A speckle structure is often observed (F. Roddier, 1981).

Turbulence was defined by Taylor and Von Karman (Karman, 1937) as an “irregular motion”. Some of the key elements of turbulence, are that it occurs over a large range of length and time scales, at high Reynolds number², and is fully three-dimensional and time-dependent (Celik, 1999). A Fluid that is not turbulent is called laminar flow.

2.1 Atmospheric Turbulence

The atmospheric turbulence is created by fluctuations in the air refractive index, spatially and temporally. This is directly related to the temperature of the air. Stars are very far away, but when their light goes through the atmosphere, it will cross a section of height H , where the refractive index will be changing with the altitude. We can assume that it is possible to divide the full atmosphere in several small layers, of thickness δh , in which the refractive index remains the same. This means that we can ignore the diffraction effects within the layer (F. Roddier, 1981). Hence, the final phase $\phi(\varepsilon)$ will be the integral effect of the refractive index for all the layers:

² Parameter that characterizes a flow of a viscous fluid, that only depends on the geometry of the flow, Reynolds found that when this number was greater than ≈ 13000 , the flow stops to be laminar (Saint-Jacques, 1998).

$$\phi(\varepsilon) = k \int_h^{h+\delta h} n(h, \varepsilon) dh \quad (2.1)$$

where k is the wave number, $2\pi/\lambda$, with λ being the wavelength of the light and ε is a spatial parameter.

Recalling that the refractive index is a function of the temperature and the atmospheric pressure (Hecht, 2002):

$$n(h) \equiv (n - 1) \times 10^6 \quad (2.2)$$

$$n(h) = 77.6 \cdot \left(1 + \frac{7.52 \times 10^{-3}}{\lambda} \right) \times \left(\frac{P}{T} \right) \quad (2.3)$$

Since the aberrations generated by the turbulence are a random process, they can be described using statistical estimates such as variance or covariance's (F. Roddier, 1981). These aberrations are non-stationary random processes. The refractive index of the air is the parameter of importance in optical astronomy, and it follows the statistical inhomogeneity of the temperature of the atmosphere, which are governed by Kolmogorov-Obukhov law of turbulence (F. Roddier, 1999).

A turbulence model is defined as a set of equations that will determine the turbulent transport terms in the mean flow equations and thus close the system of equations. As atmospheric researchers cannot perform controlled experiments, they use standard "scientific models", formulating hypothesis, testing them by experiment and then formulating revised hypotheses. As these descriptors cannot be applied directly, one uses models of the process that causes a certain phenomena and then compares it with real data. These models are usually formulated in terms of highly non-linear mathematical equations, and then solved them by numerical computation. The performance of the model is judged by comparing the model's behavior with the real behavior of the atmosphere.

There are two main branches to study the turbulence. One is using the mathematical equations for modeling, like Navier Stokes, that are defined for fluid motion, using the Lagrangian perspective, but this solutions are unstable at large Reynolds number and sensitive to the boundary and initial conditions. The other branch, more widely used in astronomy, uses the statistical behavior of the atmosphere turbulence.

The focus of the modeling is based on statistical analysis because it is impossible to instantaneously describe the behavior of the refractive index, as there are too many random behavior and variables.

2.1.1 Kolmogorov Turbulence

One of the most popular model, and widely used for the atmospheric turbulence was proposed by Kolmogorov (Kolmogorov, 1941) and developed later by Tatarskii (V. Tatarskii, 1961).

It considers the atmosphere as a fluid flow that has a large Reynolds number (Re), and can be described by the general equations of hydrodynamics: Navier-Stokes equations and the equations of continuity (V. I. Tatarskii, 1971).

This model assumes that energy is added to a fluid medium in form of large spatial scale disturbances called eddies, which are then break down into smaller structures decreasing the Reynolds number. When this number drops below a certain critical value, the fractioning process stops and the kinetic energy that was originally contained in the big eddies is then dissipated into heat by viscous friction. Kolmogorov used the hypothesis that the small structure of the motion is locally homogeneous and isotropic. The scale size at which dissipation starts is called the “*inner scale*” of turbulence (l_0). In the troposphere, l_0 is on the order of a few millimeters (F. Roddier, 1981; Shöck, 1998). The outer scale is the largest spatial scale of the turbulence on which the energy is introduced into the system (Tyson, 2011).

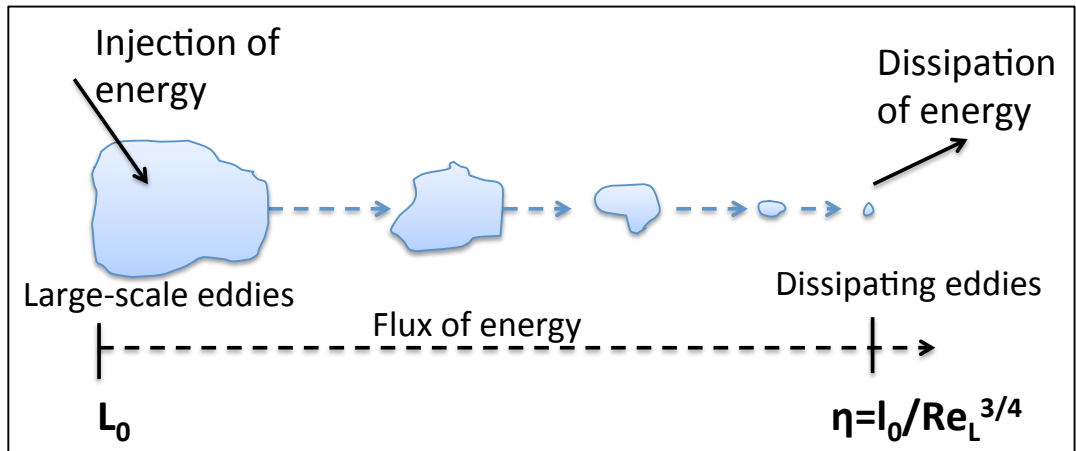


Figure 2-2: Development of the turbulence from the injection of the energy until the dissipation into heat. Re_L : Large Reynold number.

The kinetic energy of a fluid in motion is proportional to v^2 , the square of the mean velocity, which in turns is proportional to the $l^{2/3}$, where l is the scale size. For spectral analysis, the kinetic energy is written as a function of wave-number vector κ . Because $\kappa \propto 1/l$, the energy $E(\kappa)d\kappa$ between κ and $\kappa + d\kappa$ is then described by:

$$E(\kappa) \propto \kappa^{-5/3} \quad (2.4)$$

In the isotropic case (proved by Taylor, 1938) and considering the three-dimensional energy, if we integrate over all directions of the energy, we obtain:

$$E(\kappa) = 4\pi\kappa^2 E(\vec{\kappa}) \quad (2.5)$$

So then:

$$E(\vec{\kappa}) \propto \kappa^{-11/3} \quad (2.6)$$

The Kolmogorov model describes the behavior on spatial scales in the “inertial subrange” between the “outer scale” (L_0) and the “inner scale” mentioned before.

The refractive index can also be described by a structure function:

$$D_n(\Delta\vec{x}) = \langle [n(\vec{x}) - n(\vec{x} + \Delta\vec{x})]^2 \rangle_{\vec{x}} \quad (2.7)$$

where $n(x)$ is the refractive index at point x , and the value of $D_n(\Delta\vec{x})$ is a measure of the variance of the refractive index fluctuations between the points separated by $\Delta\vec{x}$. The structure functions are a “statistical measure of random fields and closely related to auto-correlations” (Schmidt, 2010).

The refractive index structure function for Kolmogorov turbulence is then:

$$D_n(\Delta x) = C_n^2(h)\Delta x^{2/3} \quad l_0 < \Delta x < L_0 \quad (2.8)$$

Where $C_n^2(h)$ is the “refractive index structure constant” that describes the strength of the atmospheric turbulence as a function of the altitude h .

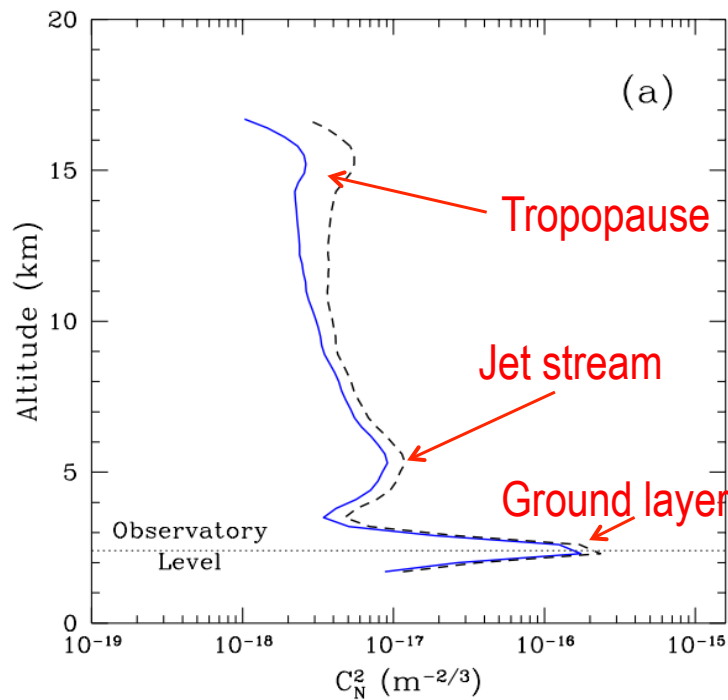


Figure 2-3: Typical C_n^2 Turbulence profile measured at La Palma (García-Lorenzo & Fuensalida, 2011)

The power spectral density (PSD) of the refractive index fluctuations is given by:

$$\Phi_n(\xi) = 0.033C_n^2(h)\xi^{-11/3} \quad (2.9)$$

where $\xi = 2\pi/\Delta x$ is the angular spatial frequency. This equation is only valid in the inertial range, which is between $2\pi/L_0 \leq \xi \ll 2\pi/l_0.z$

The PSD of the optical phase fluctuations $\phi(r)$ as a function of the wave-number and the Fried parameter (described later, section 2.1.3) is given by:

$$\Phi_\phi(\kappa') = 0.023(\kappa')^{-11/3} \cdot r_0^{5/3} \quad (2.10)$$

where $\kappa' = 2\pi/|r|$, and r is a two dimensional vector of the position, and r_0 correspond to the coherence length.

The Fried parameter or coherence length r_0 (Fried, 1965), describe the total strength of the atmospheric turbulence and is given by:

$$r_0 = \left(\frac{2.91}{6.88} k^2 (\cos\gamma)^{-1} \int_0^\infty C_n^2(h) dh \right)^{-\frac{3}{5}} \quad (2.11)$$

where γ is the zenith angle, and $k = 2\pi/\lambda$. The Fried parameter is thus proportional to the wavelength $r_0 \propto \lambda^{6/5}$. This means that for short wavelength (like visible or UV) the distortions are larger on average than for long wavelength (like radio waves or infrared). Typical values of r_0 are between 5 and 20 cm at visible wavelength, and from 20 to 120 cm in the infrared (Lukin, Fortes, & Physicist, 2002).

2.1.2 Von Karman Turbulence

As some measurements suggested that the atmosphere was not always following the Kolmogorov power law of $-11/3$, like was presented in equation 2.10, other models emerged, like the generalized spectrum proposed by Boreman and Dainty (Boreman & Dainty, 1996), with a power spectrum of $-9/3$.

The Von Kármán model follows the same power spectrum as the Kolmogorov one, but has two cuts, one given by the outer scale, and the other given by the inner scale. The equation to generate the power spectral density $\Phi_n(\xi)$ for the Von Kármán model is:

$$\Phi_n(\xi) = \frac{0.033C_n^2}{(\xi^2 + \xi_0^2)^{11/6}} \quad (2.12)$$

where $\xi_0 = 2\pi/L_0$ for $0 \leq \xi \ll 1/l_0$ (Schmidt, 2010).

The comparison between the different models can be seen in Figure 2-4:

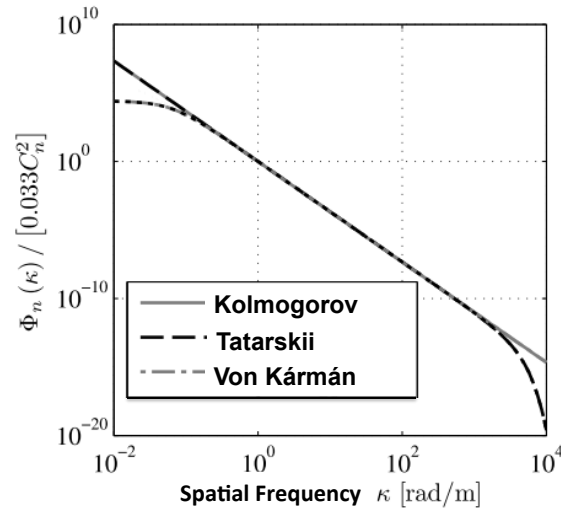


Figure 2-4: Spatial frequency for the different models of turbulence, Kolmogorov, Von Karman and Tatarskii.

2.1.3 Seeing and atmospheric parameters

A widely used parameter in optical astronomy is the one called seeing, corresponding to the maximum angular resolution of an object observed through the atmosphere without correction, i.e. the angular size of the image produced by an optical system (telescope) degraded by the atmospheric turbulence (A Tokovinin, Kellerer, & Coudé Du Foresto, 2008).

$$seeing = 0.98 \cdot \frac{\lambda}{r_0} \quad (2.13)$$

Without the turbulence, the image would have an angular resolution, defined by the aperture of the system, usually circular for a telescope, and given by:

$$R = 1.22 \cdot \frac{\lambda}{D} \quad (2.14)$$

where R is the minimum angular distance between two resolved point sources of equal magnitude, D is the diameter of the circular aperture, λ is the wavelength.

The *Strehl ratio* is a measure of how close the image is to the diffraction limit. A Strehl ratio of 100 percent means perfectly diffraction limited. Regular “seeing-limited” images obtained in the near-infrared with state-of-the-art large telescopes (8-meters), typically show Strehl ratios of about 1 percent³. In the search of always-larger collecting area for the telescopes, it quickly became obvious that one needed to correct for the effect of the atmosphere to reach the maximum resolution of the telescope. This has led to the development of the field of adaptive optics (AO). At the Gemini South telescope (8-m diameter), using an AO system on December 18th 2011, the observing team obtained images with an angular resolution down to 0.049 arcsecond and Strehl ratios up to 40 percent at 1.65 microns wavelength.

The *Coherence time* (τ_0) corresponds to the duration before one can consider that the wavefront phase has changed significantly. It can be seen as the maximum time during which one can consider to have the same turbulence. It obviously depends on the velocity (v) of the turbulence across the pupil:

$$\tau_0 = 0.314 \frac{r_0}{v} \quad (2.15)$$

This time has also been called Greenwood time delay (D. L. Fried, 1990; F. Roddier, 1999). The Greenwood frequency is a measure of the rate at which the Kolmogorov atmospheric turbulence changes with time.

³ <http://www.gemini.edu/node/11718>

$$f_G = 2.31\lambda^{-6/5} \left[\sec\beta \int_0^L C_n^2(z) v_w^{5/3}(z) dz \right]^{3/5} \quad (2.16)$$

And when the wind is constant, this frequency can be approximated by (Tyson, 2011):

$$f_G = 0.43 \frac{v_w}{r_0} \quad (2.17)$$

The angle θ_0 is known as the “*isoplanatic angle*” and is the separation between two light paths when their mean wavefront difference is 1 rad (the anisoplanatic error is 1 rad²). If we consider h as the height of a turbulent layer, for a single layer the equation for the isoplanatic angle will be:

$$\theta_0 = 0.314(\cos\theta) \frac{r_0}{h} \quad (2.18)$$

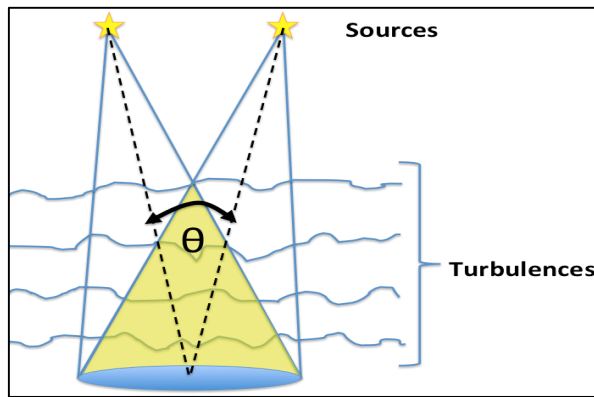


Figure 2-5: Isoplanatic angle is the maximum angular separation of two stars that shares almost the same turbulence.

2.1.4 Inner Scale and Outer Scale

As explained before, the Earth is heated during the day by absorption of the Sun radiation energy, and then gets cooler at night. This cycle causes large-scale temperature variations of the atmosphere, creating the wind and convection. The different temperatures mixes, creating sections of air called

eddies. The biggest eddy corresponds to the “outer scale” (L_0), which is thus the largest spatial scale of the turbulence on which the energy is introduced into the system. It therefore corresponds to a cut-off in the turbulence spectrum at low frequencies. The smallest eddy corresponds to the “inner scale” (l_0), that is the scale size at which dissipation of energy starts. This parameter characterizes the dissipation of kinetic energy in a turbulent layer. All the effects concerning the transport of heat and momentum (dissipation and viscosity) take place at a small eddy size (high spatial frequency) (Masciadri & Vernin, 1997).

The Kolmogorov spectrum assumes an inner scale equal to zero and an infinite outer scale. In reality, the Kolmogorov spectrum is valid but only for the range of spatial frequencies $1/L_0 < \kappa < 1/l_0$ constituting the inertial subrange. Within this range, the atmosphere can be considered as statistically homogeneous and isotropic, meaning that the velocity and refractive index have stationary increments (Schmidt, 2010).

A finite L_0 reduces the variance of the low order modes of the turbulence, and in particular decreases the image motion (the tip-tilt). The result is a decrease of the full width half maximum (FWHM) of the point spread function (PSF).

Typical values for the outer scale may vary between 1m and 100m, and for the inner scale, this can be between 1mm and 10mm. Usual values used in the field for simulations, are 20 m and 5 mm respectively (Osborn, 2010).

2.2 Frozen Flow Hypothesis

The present work considers as a main assumption (as many other related works in the area), the frozen flow hypothesis (FFH) (Taylor, 1938) to describe the temporal development of the atmospheric turbulence on short time scales. The FFH assumes that the atmospheric turbulence is located in independent horizontal layers, and each one of these layers is assumed to be “frozen” for the time it takes to travel across the telescope pupil and to move with a constant

speed, the wind speed (M Schöck & Spillar, 2000; Matthias Schöck, 1998). The following equation expresses the phase delay $\phi(x,t)$ at time t and position x , in the aperture plane, due the atmospheric turbulence:

$$\phi(x,t) = \sum_i \phi_i(x,t) \quad (2.19)$$

$$\phi(x,t + \Delta t) = \sum_i \phi_i(x - v_i \cdot \Delta t, t) + \varepsilon(x,t, \Delta t) \quad (2.20)$$

where $\phi_i(x,t)$ corresponds to the phase delay caused by the layer i , v_i correspond to the velocity in that layer, and $\varepsilon(x,t, \Delta t)$ represents the deviation from the frozen flow.

We can define the spatial normalization operator $*$ as (Shöck, 1998):

$$f^*(x,t) \equiv \frac{f(x,t)}{\sigma_f(t)} \quad (2.21)$$

where $\sigma_f(t) = \sqrt{\langle f^2(x,t) \rangle_x}$ is the spatial standard deviation of $f(x,t)$ at a time t . $\langle \rangle_x$ denotes the average over all x . Then, we will have at any time t , $\langle [f^*(x,t)]^2 \rangle_x = 1$.

And using the autocorrelation function of the normalized wavefront phases in the pupil plane, considering the atmospheric turbulence as homogeneous:

$$\Gamma_{\phi^*}(\Delta x, \Delta t) = \langle \phi^*(x,t) \phi^*(x + \Delta x, t + \Delta t) \rangle_{x,t} \quad (2.22)$$

Using the definition of (2.21) on (2.19), we get:

$$\phi^*(x,t) = \sum_i \frac{\sigma_{\phi_i}(t)}{\sigma_{\phi}(t)} \phi_i^*(x,t) \quad (2.23)$$

And using the definition of (2.21) for (2.20), we get

$$\begin{aligned}
\phi^*(x + \Delta x, t + \Delta t) &= \sum_i \frac{\sigma_{\phi_i}(t)}{\sigma_{\phi}(t + \Delta t)} \phi_i^*(x + \Delta x - v_i \Delta t, t) \\
&\quad + \frac{\varepsilon(x + \Delta x, t, \Delta t)}{\sigma_{\phi}(t + \Delta t)}
\end{aligned} \tag{2.24}$$

With (2.23) and (2.24), we have the autocorrelation function.

Defining $C_i^2(\Delta t) \equiv \left\langle \frac{\sigma_{\phi_i}(t)^2}{\sigma_{\phi}(t) \cdot \sigma_{\phi}(t + \Delta t)} \right\rangle_t$, and assuming that the layers are

independent and that the error term $\varepsilon(x + \Delta x, t, \Delta t)$ is a random function with zero mean, we can re-write the equation (2.22) as:

$$\Gamma_{\phi^*}(\Delta x, \Delta t) = \sum_i C_i^2(\Delta t) \langle \phi_i^*(x, t) \phi_i^*(x + \Delta x - v_i \Delta t, t) \rangle_{x,t} \tag{2.25}$$

If all turbulent layers follow the same statistics, the term $\langle \phi_i^*(x, t) \phi_i^*(x + \Delta x, t) \rangle_{x,t}$ in the previous equation is constant.

Defining:

$$\gamma_{\phi^*}(\Delta x) \equiv \langle \phi_i^*(x) \phi_i^*(x + \Delta x) \rangle_{x,t} \tag{2.26}$$

we get:

$$\Gamma_{\phi^*}(\Delta x, \Delta t) = \sum_i C_i^2(\Delta t) \gamma_{\phi^*}(\Delta x - v_i \Delta t) \tag{2.27}$$

When considering the case when $\Delta t = 0$, the error term $\varepsilon(x, t, \Delta t) = 0$, and we will have:

$$\Gamma_{\phi^*}(\Delta x, 0) = \gamma_{\phi^*}(\Delta x) \tag{2.28}$$

As Roddier showed (F. Roddier, 1981), $\gamma_{\phi^*}(\Delta x)$ corresponds to the theoretical shape of the correlation function of the atmospheric wavefront distortions at any given time.

As shown by Schöck (M Schöck & Spillar, 2000), for a perfect FFH the error $\varepsilon(x, t, \Delta t) = 0$, and the sum $\sum_i C_i^2(\Delta t)$ stays constant and equal to unity for all Δt .

Then $C_i^2(\Delta t)$ can be measured by deconvolving the experimentally determined autocorrelation function using $\gamma_{\phi^*}(\Delta x)$ as the kernel:

$$\Gamma_{\phi^*}^{deconvolved}(\Delta x, \Delta t) = \sum_i C_i^2(\Delta t) \delta(\Delta x - v_i \Delta t) \quad (2.29)$$

where $\delta(x)$ is the delta Dirac function.

The equations obtained before, can be used to quantify the FFH, by using the wavefront phase data from on-sky data. But as mentioned by Shöck (M Schöck & Spillar, 2000; Matthias Schöck & Spillar, 1999), it can be also calculated using the wavefront gradient data, highly convenient for this work, as the data used here was only the gradient. Performing this change will merely change the shape of the autocorrelation function $\gamma_{\phi}(x)$. It is important to mention, that it is convenient to remove the tip and tilt from the probed wavefront (slopes). This will reduce losses in correlations and errors associated to tracking and vibrations from the telescope.

Schöck (Matthias Schöck, 1998) derived an equation for the autocorrelation function $\gamma_{\phi}(x)$, using gradients with tilt removed data, for x and y :

$$\alpha(x, y) = -\frac{\lambda}{2\pi} \frac{\partial}{\partial x} \phi(x, y) \quad (2.30)$$

$$\beta(x, y) = -\frac{\lambda}{2\pi} \frac{\partial}{\partial y} \phi(x, y) \quad (2.31)$$

with this, we obtain:

$$\Gamma_{\alpha}^{SE}(\Delta x, \Delta y) = \sigma_{\phi}^2(0) \gamma_{\alpha^*}^{SE}(\Delta x, \Delta y) \quad (2.32)$$

$$\Gamma_{\beta}^{SE}(\Delta x, \Delta y) = \sigma_{\phi}^2(0) \gamma_{\beta^*}^{SE}(\Delta x, \Delta y) \quad (2.33)$$

$$\Gamma_{\alpha}^{SE}(\Delta x, \Delta y) = \frac{\lambda^2}{8\pi^2} \quad (2.34)$$

$$\cdot 6.88r_0^{-5/3} \left[\frac{5}{3}(\Delta x^2 + \Delta y^2)^{-1/6} - \frac{5}{9}\Delta x^2(\Delta x^2 + \Delta y^2)^{-7/6} - 2D^{-1/3} \right]$$

$$\Gamma_{\beta}^{SE}(\Delta x, \Delta y) = \frac{\lambda^2}{8\pi^2} \quad (2.35)$$

$$\cdot 6.88r_0^{-5/3} \left[\frac{5}{3}(\Delta x^2 + \Delta y^2)^{-1/6} - \frac{5}{9}\Delta y^2(\Delta x^2 + \Delta y^2)^{-7/6} - 2D^{-1/3} \right]$$

The superscript SE stands for the short exposure. D corresponds to the diameter of the telescope, r_0 corresponds to the Fried parameter, and λ is the wavelength of observation. With the last equations it is possible to estimate the Fried's parameter r_0 at time offset $\Delta t = 0$. For positive time offsets, the experimental autocorrelation is a sum of functions $\gamma_{\alpha^*}^{SE}(\Delta x, \Delta y)$, that have been displaced by the wind in a distance $v_i \Delta t$.

Since $\gamma_{\alpha^*}^{SE}(\Delta x, \Delta y)$ is strongly peaked at the origin, at a fixed Δt , can be measured the distance $v_i \Delta t$, and then determined the individual layer wind speed v_i .

2.3 Correcting for the effect of the atmosphere: Adaptive Optics (AO)

2.3.1 History

The astronomer Horace Babcock (Babcock, 1953), was the first to suggest that it could be possible to compensate the effect of the atmosphere by introducing in the light path a mirror whose shape can be modified mechanically and controlled

by a feedback system: currently known as “deformable mirror”. By measuring and correcting for the wavefront distortions, one can improve the image quality, providing a smaller PSF. But it took a long time from the idea of Babcock to the first AO system, as the needed technology was not available until years later.

The first AO system was designed by the U. S. Department of Defense in the 1970’s, driven by a large research program on methods to keep the laser beam shape focused in the atmosphere. The only previous experiments with adaptive correction dates back to 1936 where a tip/tilt correction had been used to improve the quality of a long exposure image by actively adjusting the position of the target and centering it on the slit of a spectrograph, in order to improve its efficiency for long exposures. Linnik, in 1957 (Hardy, 1998; Linnik, 1994), proposed to use a segmented mirror and to apply a “piston” motion to each segment, so that the image would be close to the diffraction limit imaging. But it was only in the 1980’s that the technology allowed bringing his idea to life, in what today we know as an AO system.

Nowadays, two kinds of correction for the deformations of the wavefront can be distinguished: one is called “Active Optics“, and the other is called “Adaptive Optics“. The main difference between the two is the frequency (speed) of the correction. For the first one, the corrections are sent at about 0.05 Hz or less, mainly to correct for mechanical deformations in the telescope structures, thermal deformations, optical manufacturing errors, and any other slowly evolving aberrations or problems whose evolutions are not too fast for low frequency corrections. For adaptive optics systems, it is imperative to go faster, as fast as the atmosphere is changing, i.e. with frequencies around 100-1000 Hz, and depending also of the observed wavelength (X. Wang, 2013).

2.3.2 Definition and components

An AO system is essentially a control loop in which parameters are adjusted as a function of measurements. The system consists of three main subsystems: the wavefront sensor (WFS), the deformable mirror (DM) and the control system (a computer – the brain).

The WFS is a device for measuring the aberrations of an optical wavefront. Its measurement frequency should equal the frequency of the needed correction loop. The WFS is the key element of an AO loop, as its sensitivity, speed and measurement errors determine the accuracy of the corrections. The measurements provided by the WFS feed the controller, which sends commands to the DM that is located in the pupil plane and corrects the cumulative turbulence along the optical axis (case for a single DM and one guide star also known as single conjugate adaptive optics, SCAO).

The correction may be done either in open or in closed loop. The most common or traditional way is the closed loop approach; this means that the WFS probes the atmosphere and corrections are then calculated to be applied to the DM. In open loop the effects of the applied corrections are not seen by the WFS.

2.3.2.1. WFS requirements

The wavefront sensor is a main part of an AO system; its function is to measure the wavefront distortions. The main requirements of WFS are:

- It needs to use the photons efficiently.
- Ideally it should be linear over the full range of atmospheric distortions
- As the atmospheric turbulence evolve fast, the sensing needs to be done quickly.

There are mainly three different families of WFS used in astronomy: Shack-Hartmann WFS, Curvature WFS, and Pyramid WFS. The most

widely used is the first one, the SH-WFS, and as it is the type of WFS used on work presented here, I will be explaining only this one.

The SH-WFS consists of an array of lenslet positioned in a pupil plane, The wavefront sensor measures the tilt over each aperture of the lenslet by comparing the measured positions of the diffracted spots to the positions of the diffracted spots for a reference input beam, converting the wave-front of the incoming light into a vector of local gradients. The displacements are measured relative to the reference positions obtained on a plane wavefront. The pupil plane is divided into several subapertures, defined by a lenslet array, all focusing on the same detector (see Figure 2-6). The size of the subapertures should be equal or smaller to the equivalent Fried parameter in the pupil.

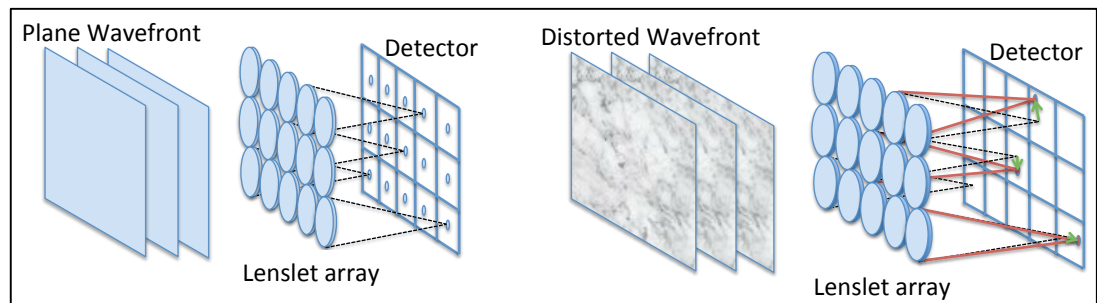


Figure 2-6: Shack Hartmann WFS diagram. The wavefront is measured by the small area of each subaperture of the lenslet. When the wavefront is plane (undistorted), each lenslet forms a spot on the detector, and all of them will form a regular grid of spots. But when the wavefront is distorted, the lenslet will create a spot a bit displaced from its original position and this provides a measure of the local wavefront.

WFS Detector

The WFS use a detector to measure the wavefront, and this will determine its sensitivity. The error will depend on the detector noise, coherent optical crosstalk between diffracted spots from different apertures, and digitization error.

The WFS detector in our case was a quadcell or segmented position sensing photodiode (PSD) consists of four photodiodes separated by a small gap, which share a common substrate. Their main advantage is that their noise is independent of the SNR of the system. But the disadvantage is that the precision in the determination of the spot center depends on the size of the spot β . Further the measurement error is non linear.

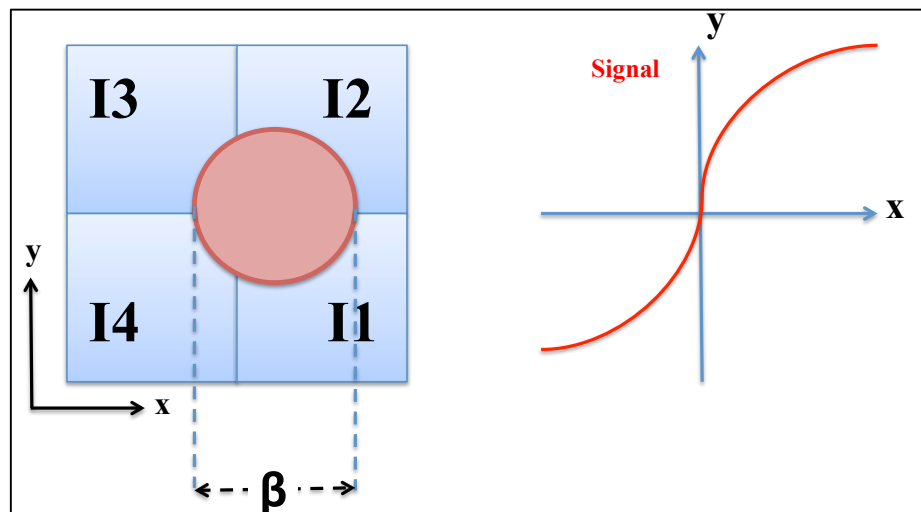


Figure 2-7: A quadcell consists of four photodiodes. An inconvenient of such a cell is that the precision in the centering depends on the spot size, and it is thus affected by the seeing, and the sodium layer in our case.

The centering of the spot on x and y are:

$$x = \frac{\beta}{2} \frac{(I_1 + I_2 - I_3 - I_4)}{(I_1 + I_2 + I_3 + I_4)} \quad (2.36)$$

$$y = \frac{\beta}{2} \frac{(I_2 + I_3 - I_1 - I_4)}{(I_1 + I_2 + I_3 + I_4)} \quad (2.37)$$

where I_x correspond to the intensity measured by the photodiode x , and β is the diameter of the spot.

The linear dynamic range of the quadcell is limited to $\pm\beta/2$.

2.3.2.2. Deformable Mirror (DM)

The DM is a mirror whose surface can be shaped in order to correct the distortions of the wavefront introduced by the atmosphere.

Some of the key parameters of the design of a DM are the number of actuators, the pitch (distance between actuators centers) and the stroke (maximum possible actuator displacement in microns, giving also the maximum amplitude of the distortions that can be corrected).

A schematic view of the DM is presented on Figure 2-8. The actuators are located below the reflecting surface. The mirror is either a thin continuous layer that can be deformed without being broken or it is a segmented mirror (where each segment is typically controlled by one or three actuators). The thin layer can be an unimorph mirror (monolithic), using piezoelectric actuators bonded to the back side of the mirror, it can be of the bimorph type where two or more layers forming the substrate of the mirror act contracting or expanding in opposite directions to generate a local bending.

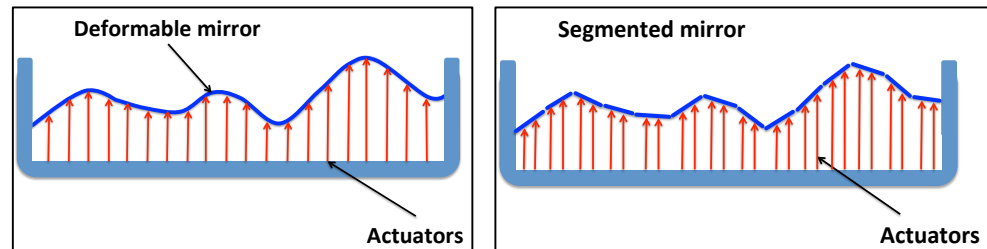


Figure 2-8: Two types of DM's, one (left) corresponds to a single thin surface, that can be modeled to the desired shape by the actuators, and the other (right) corresponds to a segmented mirror (3 actuators per segment) where the actuators control the position (piston, tip and tilt) of the each small section of the full mirror.

One important characteristic of a DM is that some of them suffer from hysteresis and creep. Hysteresis is a non-linear effect that decreases the precision of the response, and it is therefore better to characterize it. The creep corresponds to a slow drift or permanent deformation under the influence of mechanical stresses, due to a constantly applied voltage.

2.3.2.3. Laser Guide Stars (LGS)

The AO systems need a bright star on sky, because the control system has to run faster as the atmosphere changes and the integration time should thus be short. A star with a R-band magnitude brighter than 18 (around 100 photons per r_0 element) (Morris, 2005) insures sufficient flux, i.e. sufficient signal-to-noise ratios. The star also needs to lie close to the observed target,, to be within the same isoplanatic angle. Sadly we know that the sky is not very generous in providing natural stars to be used as beacons. The solution is then to generate an artificial star in the sky. For the moment, there are two methods, and both use the laser technology. One LGS technology is called “Sodium LGS”, and the other “Rayleigh LGS”.

The Sodium LGS is generated by a powerful laser operated at 589 nm. The power (around 5-10W) is sufficient to reach the layer at about 100 km altitude, where there is a small layer of sodium that can be excited by the laser photons and re-emit light, which constitutes the artificial laser guide star.

The Rayleigh LGS is generated by laserlight, which is elastically backscattered by molecules in the atmosphere (considering that the scattering is proportional to λ^{-4}). As this forms a bright line in the sky, the laser is pulsed and synchronized with the camera, in such a way that the camera sees a spot at a given altitude. By example, the Nd:YAG laser

with a pulse of 120 ns is commonly used. As the photon return depends in this case on the molecular density of the atmosphere, the maximum altitude for this kind of laser is around 35 km, but generally effective under 16 km.

An important problem of the LGS is the “cone effect”, produced because the LGS are focused at a finite altitude above the ground as opposed to natural stars that can be considered at infinity. Figure 2-9 illustrates the difference between LGS and NGS and the cone effect:

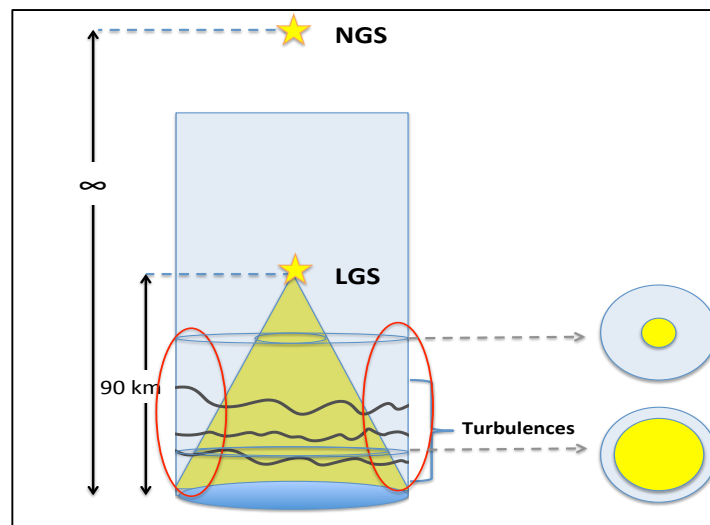


Figure 2-9: The cone effect refers to the different turbulence sampled by a NGS and a LGS. Here the two areas in red are not sampled by the LGS.

2.3.3 The Single Conjugated Adaptive Optics (SCAO)

SCAO corresponds to the classic form of AO, it consists in a closed loop between one deformable mirror (DM) conjugated to the ground layer (positioned in the pupil plane) and a wavefront sensor (WFS). One (guide) star is used to measure the distortions of the atmosphere and the applied corrections are valid within the isoplanatic patch centered on that star. SCAO corrects the integrated turbulence along the line of sight.

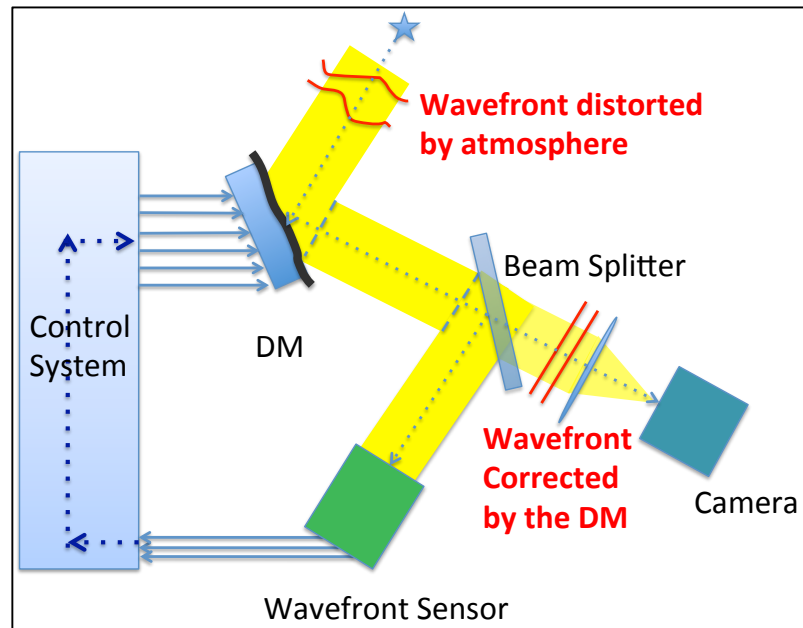


Figure 2-10: Diagram of an Adaptive Optic (AO) System. The light from the source is first reflected by the DM and then split between the scientific camera and the WFS. The WFS measures the atmospheric distortions and the control system sends the corrections to shape the DM.

2.3.4 Multi-Conjugated Adaptive Optics (MCAO)

MCAO correct a larger field of view by using several deformable mirrors conjugated to different altitudes. This allows estimating the 3-dimensional volume of turbulence above the telescope and instantaneous wavefront deformation, thus a wider field can be optically corrected.

MCAO works in a similar way to the classic AO, but needs more than one star to measure the turbulence along several directions (see Figure 2-12), and to tomographically reconstruct the phase of turbulence. The effects of correcting the full field of view can be seen on Figure 2-11.

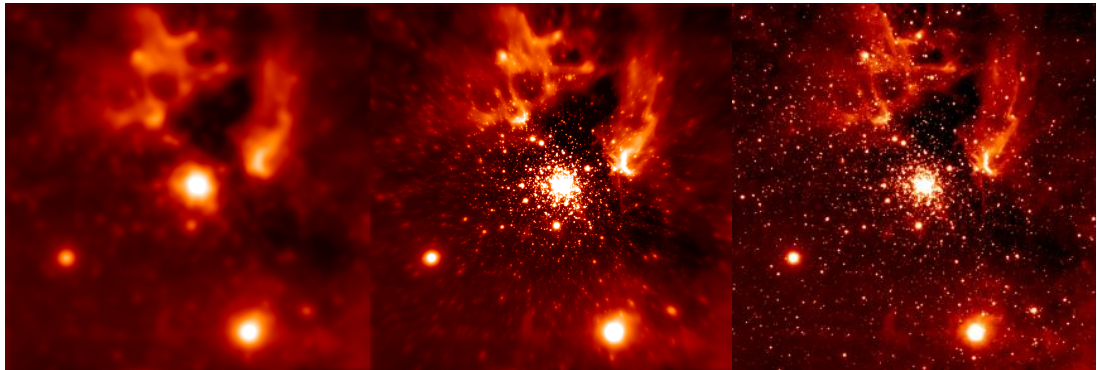


Figure 2-11: Comparison between a field of stars: without correction (left), corrected only in one direction (center) and with large field MCAO correction (right). As shown in the central image, the correction is successful over the limited central patch around the single guide star.

To be able to correct in more than one plane, MCAO needs more than one DM. A MCAO is thus usually an expensive system, as it requires multiple WFSs and DMs. Its design and operation mode shall therefore allow for an extensive use, for as much as possible scientific targets. Due to the low availability of bright guide stars in the sky, MCAO also usually works with several LGS to increase its sky coverage.

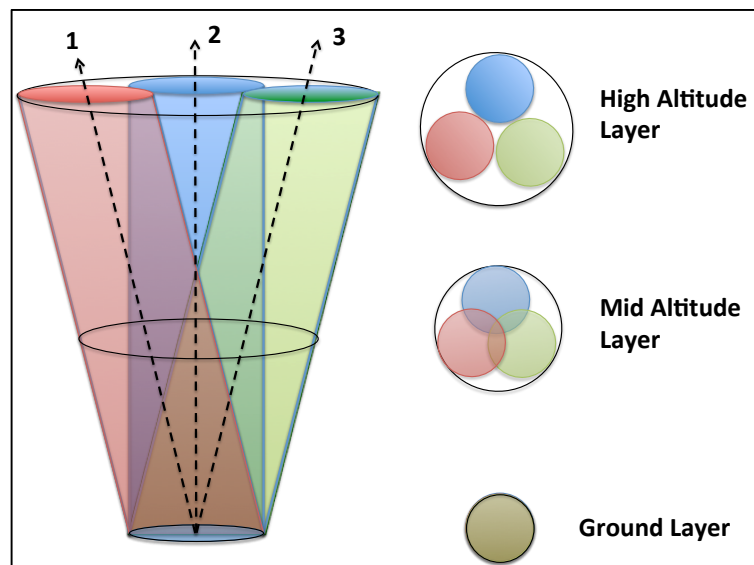


Figure 2-12: Example of MCAO Field, showing how different WFS sample different atmospheric volumes. At ground layer all WFSs sample the same ground-layer turbulence, at mid-altitude the common areas decrease and eventually vanishes at high altitude. 1,2 and 3 are different GS on the sky.

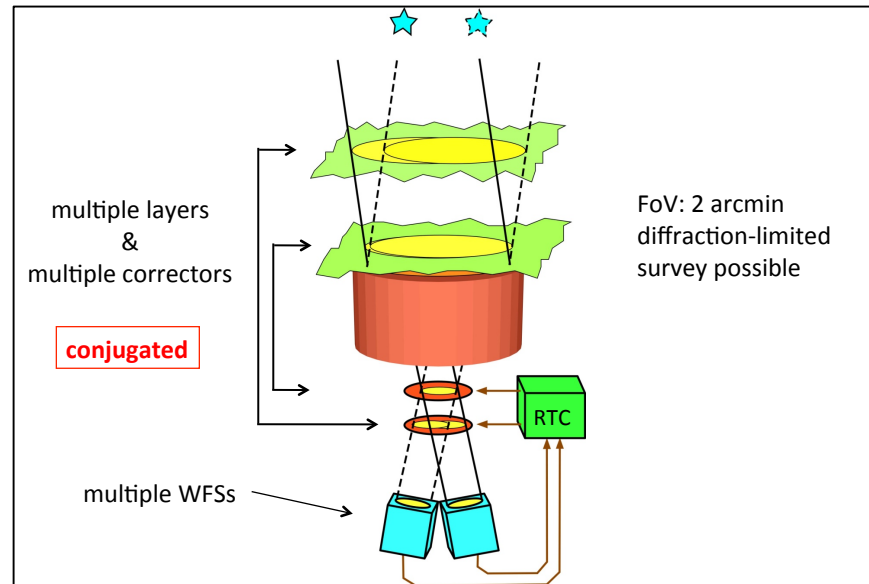


Figure 2-13: MCAO design. The distortions are measured on several GS along different directions, the turbulence is tomographically reconstructed and the distortions are then corrected by several DMs conjugated to different altitudes.

2.3.5 Ground Layer Adaptive Optics (GLAO)

GLAO is a technique used to correct only the lowest layers of the turbulence. It has been developed to decrease the cost of the MCAO and correct the most energetic part of the turbulence. The extension of the “ground layer” varies among sites. For example, at Cerro Paranal it lies around 100m, while at La Palma it can go up to 500m (Morris, 2005). The cost can be reduced, as this system will only require Rayleigh LGS (but still can use the sodium LGS), which are cheaper than the Sodium ones. This configuration can have several WFSs but only one DM is needed, which can even be a deformable secondary mirror.

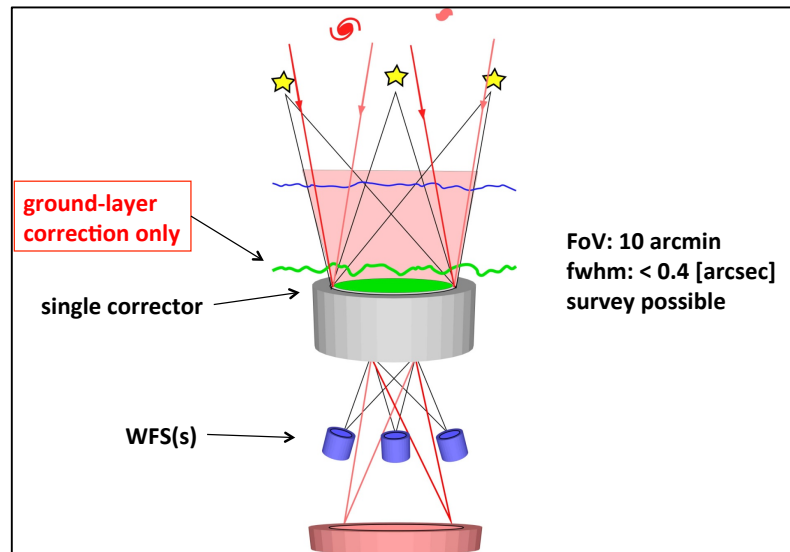


Figure 2-14: GLAO diagram, using several WFS but only one DM that is conjugated to the ground layer turbulence, which is generally the dominant layer.

2.3.6 Multi-Object Adaptive Optics (MOAO)

MOAO works in a similar way as MCAO, but instead of having big DM's to correct the turbulence in tomographic altitude, it corrects only small areas of the FoV, for each of the several targets where the DM is positioned (corrects the distortions in only the direction of one target). The advantage is that it can use smaller and cheaper DMs. The disadvantage is that it operates in open loop.

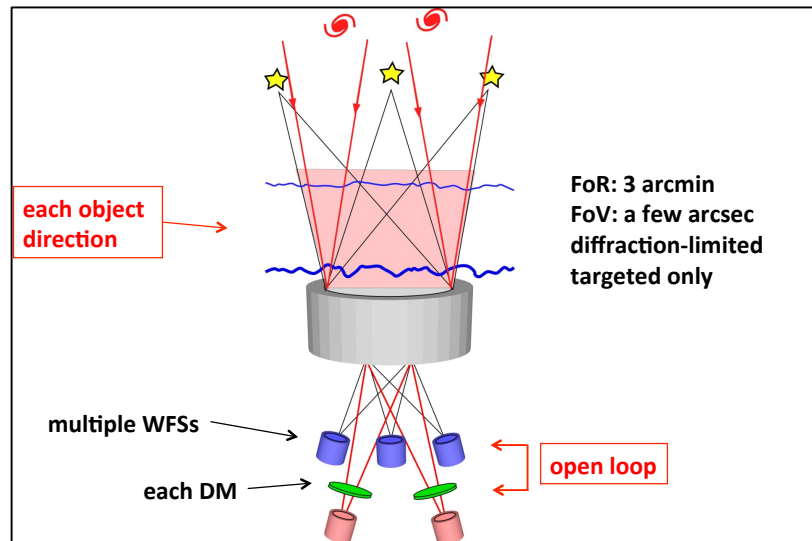


Figure 2-15: MOAO is similar to having several SCAO systems across the field (one per DM), but it works in open loop and estimates by tomographic reconstruction the turbulence along the direction corrected by the DM.

2.3.7 Laser Tomography Adaptive Optics (LTAO)

LTAO utilizes the WFS measurements from multiple LGS and tip-tilt measurements from one or more NGS. It uses a single DM, with only one single direction for the science target, but this can be located anywhere within the constellation of laser beacons on the sky. It is like SCAO, but with the difference that as it has more than one star and corresponding WFS, and can thus estimate tomographically the turbulence for the science target.

2.3.8 Extreme AO (ExAO)

ExAO is one of the most recent concept of AO, with the goal of achieving high-contrast imaging that feed spectroscopic system to be able to detect and characterize extra-solar planetary systems (faint targets close to bright sources). To perform this, it is necessary to increase the intensity peak of the target and remove the light scattered by the atmosphere and the telescope optics (Serabyn et al., 2007).

The difference with respect to the last AO concepts, it does not focus on a bigger FoV, but the goal here is to perform the best possible correction in a single point, for a very faint and complex target.

2.4 Instruments to measure the atmospheric turbulence

In this thesis we are exploring the use of a profiler system embedded in the telescope to measure the turbulence. Until now only external and dedicated instruments have been used for this purpose. Having a big constrain in the price, they are installed in small telescopes in almost every astronomical site, and can still be used as an alternative and validation method. The problem is that they are located outside the telescope dome, and usually needs a bright star, which means that they do not observe in the same direction as the scientific telescope, then they will not necessarily measure the turbulence that is observed by the telescope.

2.4.1 Differential image motion monitor (DIMM)

The DIMM is one of the instruments that can simulate the seeing conditions seen by larger telescopes. It was conceived around the 60's for qualitative seeing studies (van der Laan, Ardeberg, Vernin, Weigelt, & Wohl, 1986) and was then used by F. Roddier for quantitative measurements (F. Roddier, 1981; Sarazin & Roddier, 1990).

The instrument measures the differential centroid motion of two images resulting from splitting the light of the same star across two apertures of known separation. The images are taken at high frequency and the variance of the differential images motions is measured in the directions parallel and perpendicular to the aperture alignment. The measurements are insensitive to telescope tracking errors, vibrations or small focus errors. Therefore, the differential motion variance is caused only by the atmospheric turbulence and

can be directly related to r_0 using Tatarskii's model of turbulence (Campbell, 2009).

The problem with the DIMM is that it is not sensitive to the altitude, and thus cannot record C_n^2 profiles. It can only be used to measure the total energy of the turbulence above the telescope for the full atmosphere.

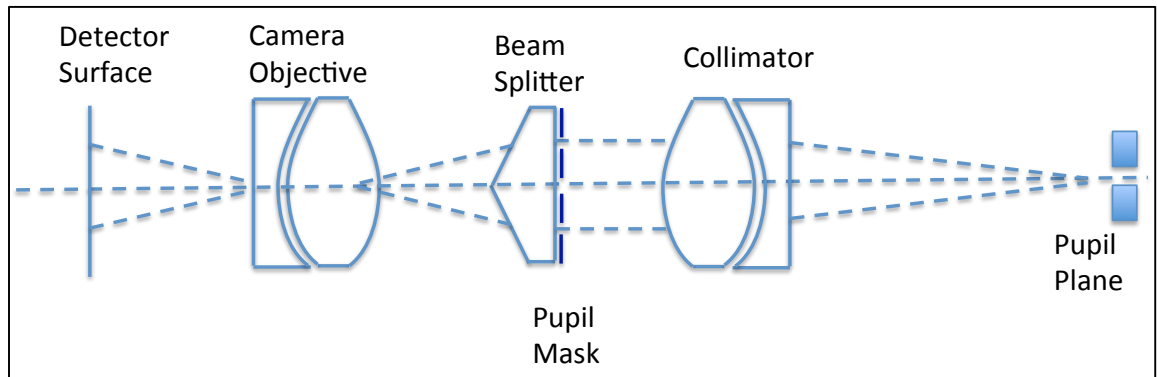


Figure 2-16: DIMM optical scheme. (Sarazin & Roddier, 1990)

2.3.9 Multi-aperture scintillation sensor (MASS)

MASS is an instrument used to measure the vertical distribution of the atmospheric turbulence. It consists of a small reflecting telescope with a detector that measures the scintillations patterns of single stars in four concentric rings of the telescope pupil. With the different ring apertures, it is possible to separate the contributions from different layers. For each ring a “scintillation index⁴” (four normal indices) is computed which is the intensity variance normalized by the square of the average intensity. The indexes are proportional to the intensity of a layer.

The ratio of scintillation index to layer intensity is called weighting function. Then scintillation indices measured by MASS are linear combinations of the layer intensities with the corresponding weighting functions. The turbulence

⁴ Scintillation index is traditionally defined as a variance of light flux normalized by the square of the mean flux or, equivalently, as a variance of relative flux fluctuations.

intensity depends on the distance to the layer as well as on the shape and size of the apertures. This means that it can give the strength of the turbulence at different altitudes.

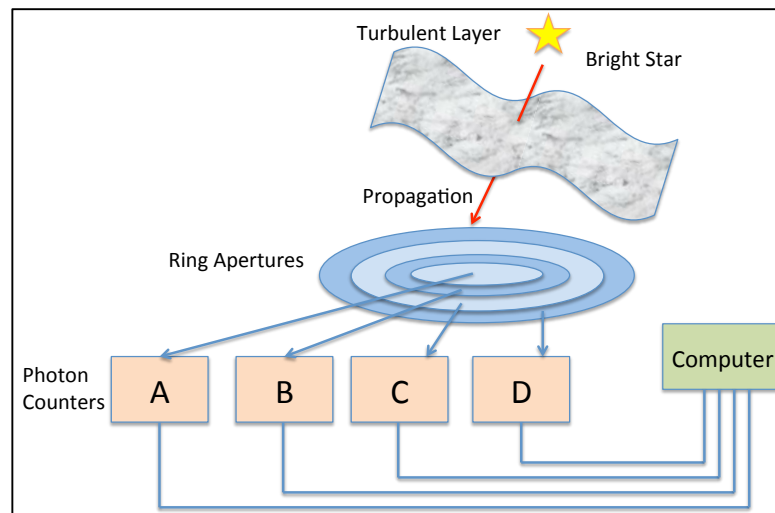


Figure 2-17: MASS instrument concept.

One of the problems of the MASS is its low vertical resolution (Andrei Tokovinin, 2004) and for bad seeing conditions, sometimes the main contribution to the turbulence comes from the higher layers (jet stream). Also the ground-layer turbulence does not produce any scintillation, and is thus not sensed by MASS, therefore underestimating the “real” seeing at such altitude.

The problem with the ground layer can be overcome with a technique that optically conjugates the detector to some negative altitude $-H$, adding a virtual turbulence-free propagation path to the real atmosphere. But this technique is inadequate for large H .

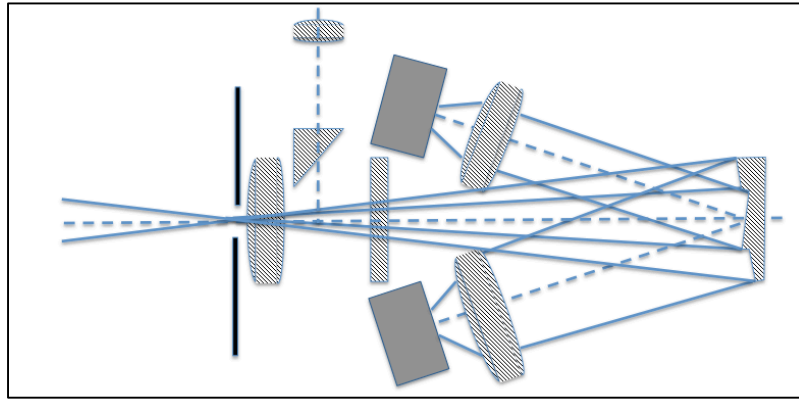


Figure 2-18: Simplified optical diagram of MASS detector.

2.3.10 The lunar scintillation system (LUSCI)

LUSCI has been developed by CTIO (Cerro Tololo Inter-American Observatory) to measure the surface layer turbulence. It consists of 6 photo-diodes of about 1-cm diameter placed in a linear non-redundant baselines configuration. The covariance of the scintillation signals between detectors pairs are averaged in time and fitted to a model of a smooth $C_n^2(h)$ profile with few parameters.

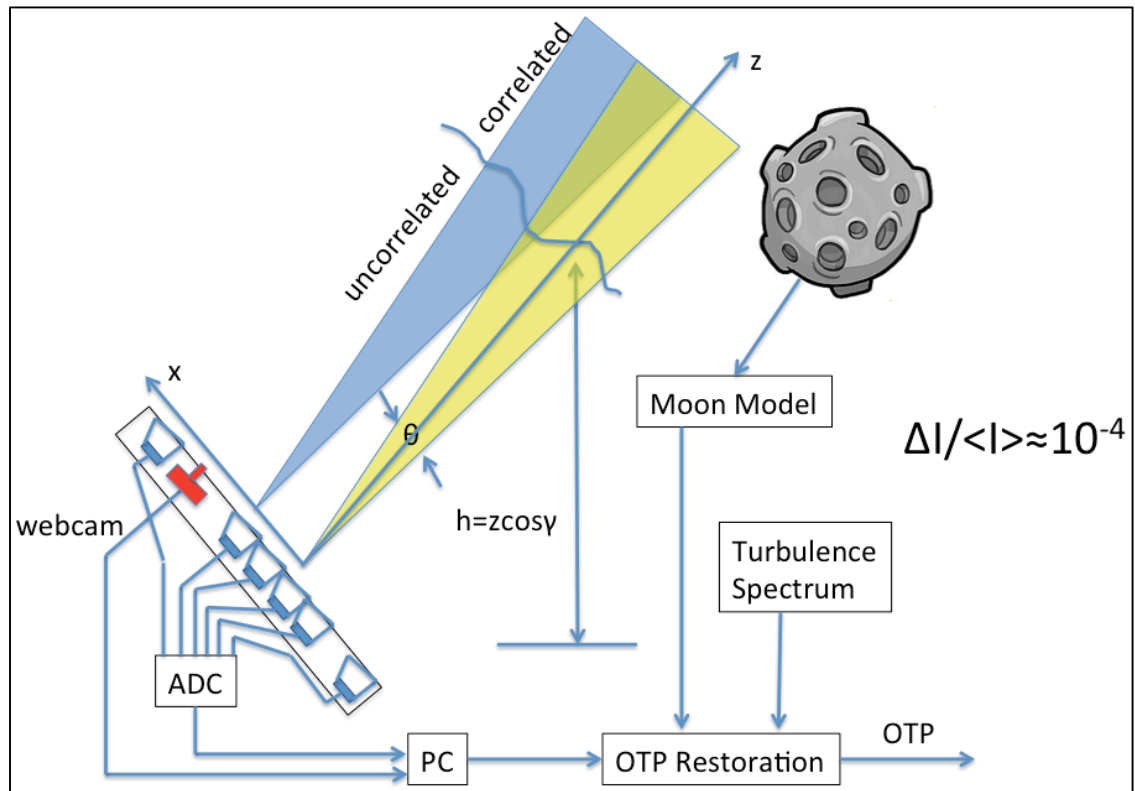


Figure 2-19: The principle of LuSci. Diagram adapted from Tokovinin's paper (A Tokovinin, Bustos, & Berdja, 2010).

It is a simple instrument that calculates the seeing from the scintillation theory and Kolmogorov model, using the covariance of light fluctuations between detectors at different baselines. It does not measure the high turbulences, and its results are sensitive to the outer scale although it cannot measure it.

The scintillation is a direct optical effect; the scintillation of stars originates mostly in high atmospheric layers. In contrast, scintillation of extended sources such as Sun or Moon is dominated by turbulence in the surface layer.

2.3.11 Scintillation detection and ranging (SCIDAR)

SCIDAR is a technique that can be used to measure the strength of the turbulence and its dependence on altitude. The method is based on the analysis of

stellar scintillation images produced from binary stars, by the turbulent layers. This technique has been developed by Vernin and co-workers over a number of years (Rocca, Roddier, & Vernin, 1974; C. Roddier & Roddier, 1975; Vernin & Pelon, 1986; Vernin & Roddier, 1973).

Stellar scintillation is due to spatial differences in refractive index in the atmosphere. An optical wave propagating through the atmosphere will experience fluctuations in the optical path length through different layers due to these refractive variations. On the ground, it produces scintillation patterns that vary on a time scale of the order of a few milliseconds. The undulation in the atmosphere acts as a lens, focusing the starlight to different regions.

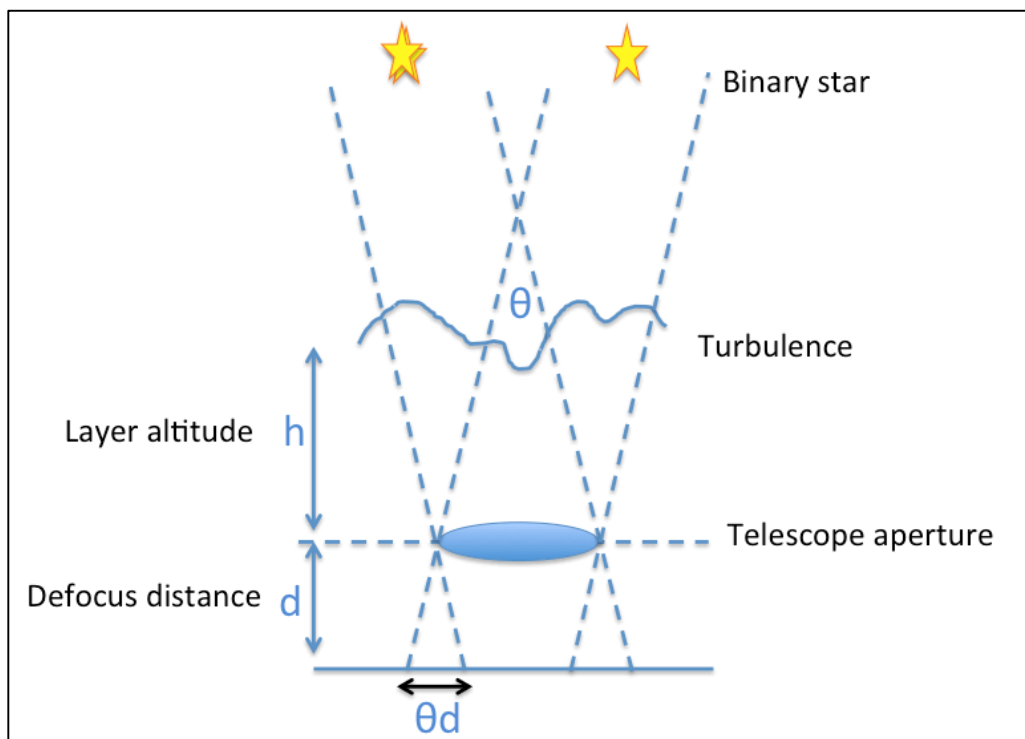


Figure 2-20: Schematic principle of SCIDAR.

SCIDAR works by imaging two stars of a binary system, with an angular separation of θ and at a distance of $d = \theta h$, h in the focal plane. This technique uses scintillation images produced by the binary star targets, and relies on the user being able to locate a suitable binary pair in the direction of interest or near

to it. The autocorrelation function will find the repeating separation pattern between the binary stars over a number of images. The separation of the peaks in the averaged autocorrelation function will yield d , hence the height of the turbulent layer can be found.

This technique also called binary star SCIDAR, the average autocorrelation of a large number of short exposure telescope pupil images for the binary. The theoretical auto-covariance of crossed-beam (binary star) scintillation data, in the case of generalized SCIDAR, is a function of both spatial and angular variables (for SCIDAR only depends of the angular variable) (Johnston, Dainty, Wooder, & Lane, 2002) and is denoted by $C_B(\rho, \theta)$, where:

$$C_B(\rho, \theta) = \sum_h \left(\frac{1 + \alpha^2}{(1 + \alpha)^2} C_s(\rho) + \frac{\alpha}{(1 + \alpha)^2} \times \left\{ \begin{array}{l} C_s[\rho - \theta(h + d)] \\ + C_s[\rho + \theta(h + d)] \end{array} \right\} \right) \quad (2.38)$$

Here $C_s(\rho)$ is the theoretical scintillation autocovariance due to a single star, α is the relative magnitude of the binary star, and $\theta(h + d)$ is the separation of scintillation patterns due to each individual star, where h represents the distance from the turbulent layer to the telescope aperture and d is the distance of defocus of the focus of the telescope. $C_s(\rho)$ is obtained by Hankel transformation of the spatial power spectrum of the scintillation $W_s(f)$, where:

$$W_s(f) = 0.039k^2 f^{-11/3} \int_0^\infty C_n^2(h) \sin(\pi\lambda h f^2) dh \quad (2.39)$$

The refractive index structure, $C_n^2(h)$, is obtained by inversion algorithm, a key parameter both in characterizing the response and in tuning adaptive optics systems in astronomy.

SCIDAR differ from MASS, as this requires binary stars, meaning that MASS has a better sky coverage, but it still needs bright stars.

2.3.12 Slope detection and ranging (SLODAR)

SLODAR is an instrument that measures the atmospheric turbulence profile using binary stars by using the local gradient of the wavefront phase aberration. It works in a similar way to SCIDAR, but instead of measuring the scintillation, it uses a Shack-Hartmann WFS to determine the local gradient of the phase aberrations. A binary star system with an angular separation of θ is used (R. Wilson, 2002). The two stars create two focal spots on each sub-aperture. The binary stars must have a separation large enough so that they are resolved in each sub-aperture. Each sub-aperture is measuring a different turbulence layer of thickness δh , of resolution:

$$\delta h = \frac{\omega_0}{\theta} \quad (2.40)$$

Considering that the number of layers corresponds to the number of subapertures of the SH (n_{sub}), one can calculate the maximum altitude that can be sampled:

$$h_{max} = n_{sub} \delta h = \frac{n_{sub} \cdot \omega_0}{\theta} \quad (2.41)$$

Thus a bigger θ implies a smaller δh , i.e. a better resolution, but a smaller h_{max} .

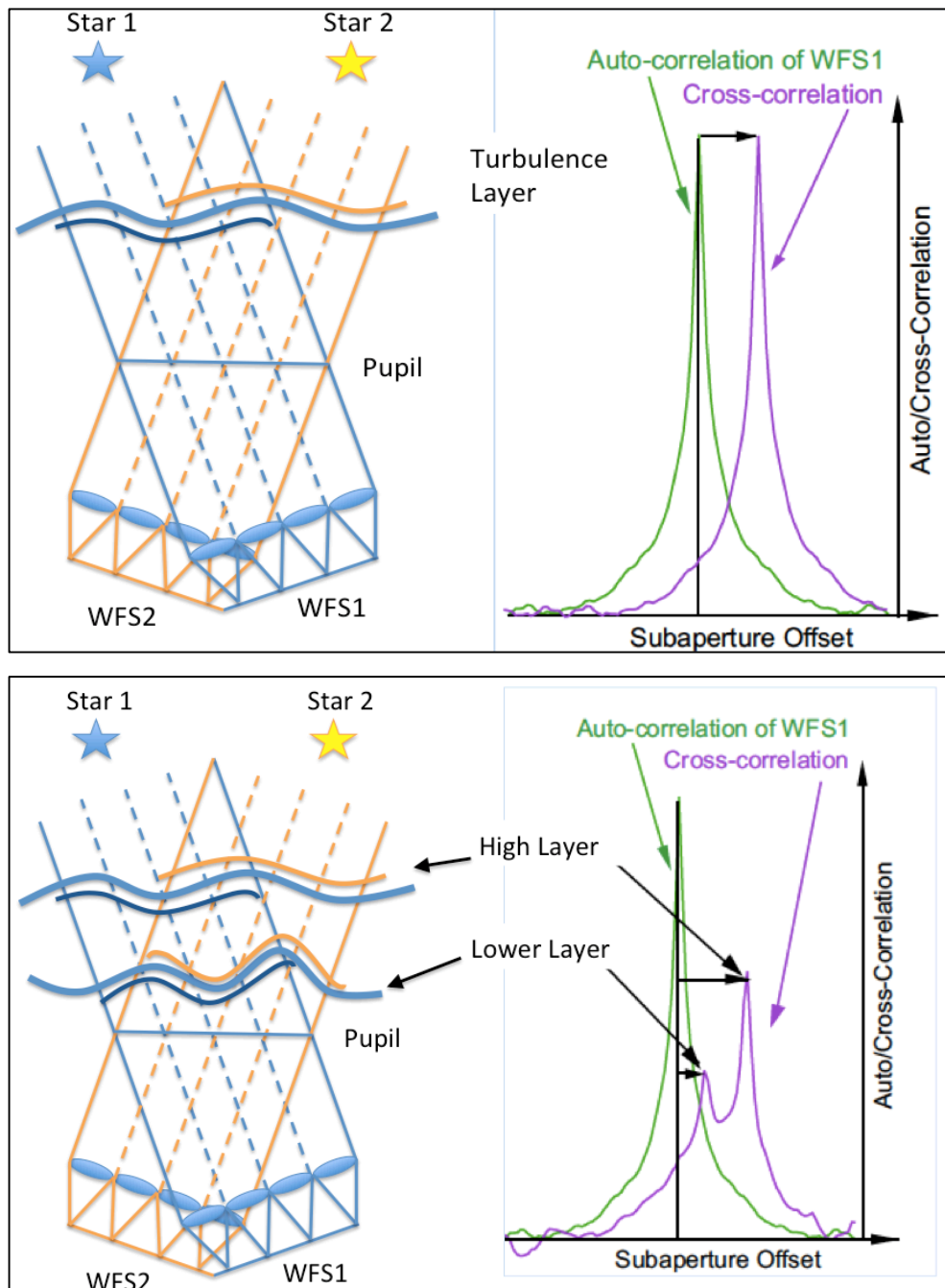


Figure 2-21: SLODAR principle (L. Wang, 2007). It samples the wavefront of two NGS. Top: there is only one layer of turbulence, and the offset is determined by cross-correlating the two wavefront measurements, as the displacement of the peak will determine the altitude of the layer. Bottom: Shows how the same principle works with two layers of turbulence, the cross-correlation will have as many peaks as layers of turbulence, and they will move away from the center, for higher altitudes.

The method consists on determining the cross-covariance as a function of the turbulence altitude. The SH-WFSs measure the slopes on each sub-aperture for both stars, $s_{i,j}^{x(1)}$ and $s_{i',j'}^{x(2)}$.

The cross-covariance for two sub-apertures is (T. Butterley, Wilson, & Sarazin, 2006):

$$C_{i,j,i',j'}^x = \langle s_{i,j}^{x(1)} s_{i',j'}^{x(2)} \rangle \quad (2.42)$$

The angular brackets denote averaging over a large number of independent realizations of the turbulent distortions over the telescope.

The covariance of the slopes across two subapertures can be found via a numerical integral involving the spatial structure function, $D\phi(\omega_0\mathbf{x})$, of the phase aberrations (R. Wilson & Jenkins, 1996).

For a turbulent layer at an altitude H, corresponding to an offset of $\Delta = H\theta/\omega_0$ in the x-direction (in units of ω_0), the covariance of the slopes, assuming that the double star is aligned along the axis of the WFS in the x-direction, is given by:

$$C'_{i,j,i',j'}^x(\Delta) = \langle (s_{i,j}^{[1]} - \overline{s^{[1]}}) (s_{i'+\Delta,j'}^{[2]} - \overline{s^{[2]}}) \rangle \quad (2.43)$$

$$C'_{i,j,i',j'}^x(\Delta) = \langle s_{i,j}^{[1]} s_{i'+\Delta,j'}^{[2]} \rangle - \langle s_{i,j}^{[1]} \overline{s^{[2]}} \rangle - \langle \overline{s^{[1]}} s_{i'+\Delta,j'}^{[2]} \rangle + \langle \overline{s^{[1]}} \overline{s^{[2]}} \rangle \quad (2.44)$$

Where the $\overline{s^{[1]}}$ is the averaged slope over all subapertures for star 1.

The response of the SLODAR to a turbulent layer at altitude H is described by:

$$X_L(\Delta, \delta i, \delta j) = \frac{1}{N_{cross}} \sum_{valid\ i,j,i',j'} C'_{i,j,i',j'}^x(\Delta) \quad (2.45)$$

Where N_{cross} is the number of such existing subaperture pairs for a given:

$$(\delta i, \delta j) = (i' - i, j' - j) \quad (2.46)$$

As the covariance function is just in the x-direction, $j' = j$.

3. GEMS AND THE ADAPTED SLODAR

The Gemini Observatory groups seven partner countries, each represented by a national office. It is operated by the Association of Universities for Research in Astronomy (AURA), Inc., under a cooperative agreement with the National Science Foundation on behalf of the Gemini partnership.

Gemini observatory consists of twin 8.1-meter diameter telescopes located on two of the best observing sites on the planet. One is located on a Hawaiian mountain (Mauna Kea), and the other in Cerro Pachón in Chile.

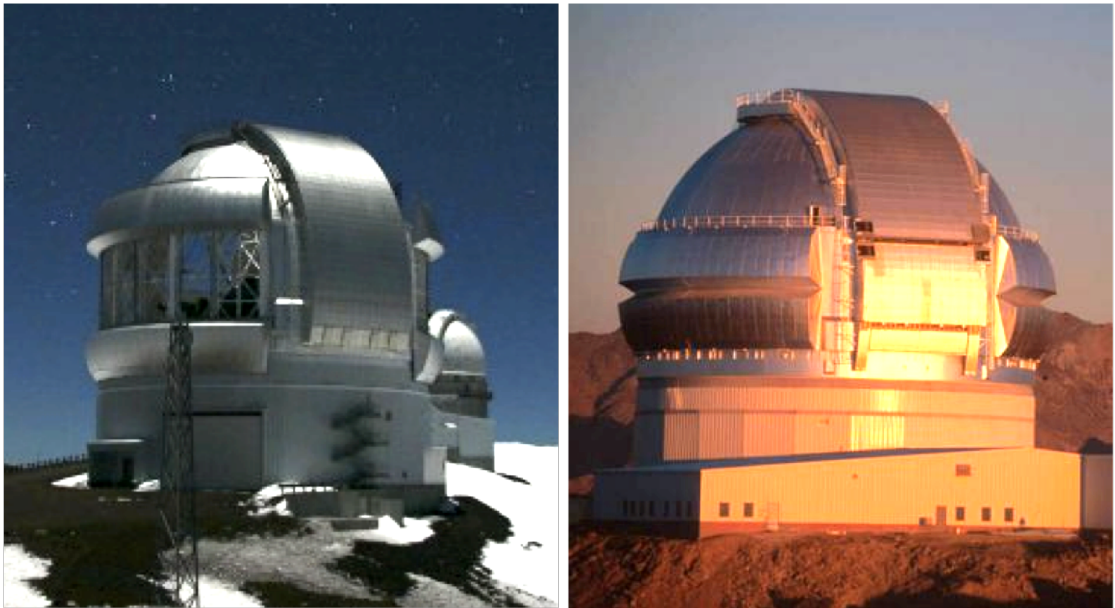


Figure 3-1: Gemini Telescopes. Left: Gemini North, at Mauna Kea (4213 m), Right: Gemini South at Cerro Pachón (2722 m altitude) (Pictures from Gemini website).

3.1 GeMS Instrument Description

The Gemini multi-conjugate adaptive optics system (GeMS) is a facility instrument for the Gemini-South telescope. The design was a programmed upgrade to the Gemini-south adaptive optics (GSAO) system to provide uniform, diffraction-limited image quality at near IR wavelengths over an extended field-of-view.

GeMS is the first and only one currently in operation MCAO system using LGSs. MAD (MCAO prototype instrument) at ESO pioneered MCAO for nighttime astronomy (Marchetti et al., 2007), but was using only NGSs (Rigaut & Neichel, 2012) and currently not in operations.

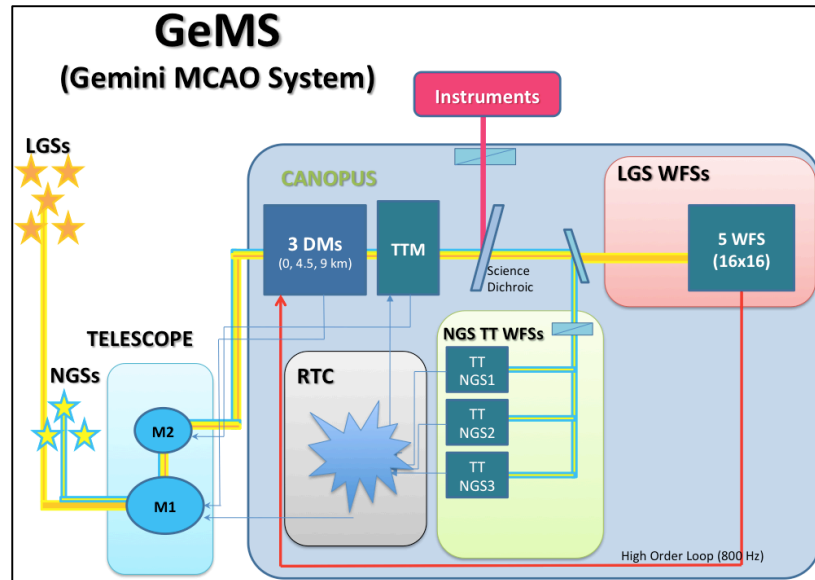


Figure 3-2: GeMS and CANOPUS, simplified diagram. The telescope observes three NGS and 5 LGS, and sends the light to CANOPUS. It uses 3 DMs to correct over a FoV of 60 arcseconds. The corrected wavefront is fed to two instruments (Flamingos2 or GSAOI).

CANOPUS is the AO bench of GeMS and consists of the opto-mechanical components of the AO module (AOM) and the associated sensors, DMs, mechanisms and motors.

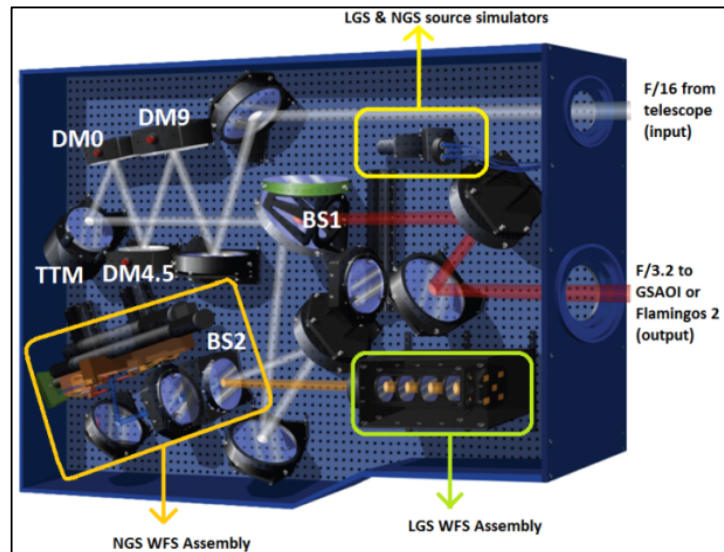


Figure 3-3: 3-D diagram of CANOPUS. The light path from the telescope to the instrument is shown as white, with the light sent to the LGS-WFS (orange) and the NGS-WFS. The red beam corresponds to the scientific image that goes to the instrument. Image from GeMS website⁵.

From Figure 3-3, it can be seen that the beam from the telescope (white), is split inside Canopus into three main components: two sensing paths and the output corrected science beam. The light from the laser constellation (589nm) is directed to five Shack-Hartman wavefront sensors (light is the orange beam, and the WFS are inside the green square) (EEV-39 80x80 CCDs read at 800Hz). Each sub-aperture uses a quadcell, with 1.38 arcsec/pixels (2.76 arcsec field of view). The visible light from the natural guide stars is sent to three independent sensors arrays (inside the orange square) (SCPM AQ4C Avalanche Photodiodes modules in quad cell arrangement) via optical fibers mounted on independent stages and a slow focus sensor (E2V-57 back-illuminated CCD). The infrared corrected beam (red beam) exits Canopus and goes to instrumentation for science (Bec et al., 2008).

⁵ <http://www.gemini.edu/sciops/instruments/gems/introduction-gems/?q=node/11751>

The design includes:

- Three deformable mirrors (DM), optically conjugated to ranges of altitude of 0, 4.5, and 9.0 kilometers with respectively 293, 416 and 208 actuators (Bec et al., 2008). Since the end of 2011, only two DMs are in operation due to degradation on one of them. However in this thesis the three of them are considered, since most of the data was acquired with the full configuration.
- Five 10-Watt-class (50 W in total) sodium laser guide stars (LGSs) from Lockheed Martin coherent technologies (LMCT), projected from a laser launch telescope located behind the telescope secondary mirror,
- Five Shack-Hartmann LGS wavefront sensors of 16 by 16 sub-apertures, and a maximum frame-rate of 800 Hz (Ellerbroek, 2003).
- And three natural guide star (NGS) wavefront sensors to measure tip/tilt (TT) (each one is a quadcell detector using avalanche photodiodes (APDs)) and tilt anisoplanatism wavefront errors.

The three DMs have different sizes (clear aperture diameter) as they are conjugated at different altitudes. The actuators of the DM are not seen completely by the SH, but can also be moved to minimize the error of the fitting between the measured wavefront and the real one. The valid actuators are the one seen by the SH; the other ones are called slaves (see the Table 1 and Figure 3-4). The DMs are based on a piezo-stack technology (developed by CILAS). During the first commissioning periods of the instrument, issues were discovered with the DM0, and the configuration was changed to a double DM system, replacing the DM0 with the DM4.5, so a final configuration with a DM conjugated at 0 km, and the other at 9 km altitude (Rigaut & Neichel, 2012).

Table 1: Deformable mirrors characteristics

	Clear aperture diameter	Number of actuators	Valid actuators	Actuator spacing	Maximum stroke average	Mechanical coupling average	Differential stroke average	Mirror surface roughness
Dm0	80 mm	293	240	5 mm	8.20 μm @ 800 V PV	23 %	2.41 μm @ 800 V PV	0.728 nm
DM4.5	106 mm	416	324	5 mm	7.71 μm @ 800 V PV	24 %	2.39 μm @ 800 V PV	0.849 nm
DM9	132 mm	208	120	10 mm	4.71 μm @ 800 V PV	22.2 %	2.68 μm @ 800 V PV	0.834 nm

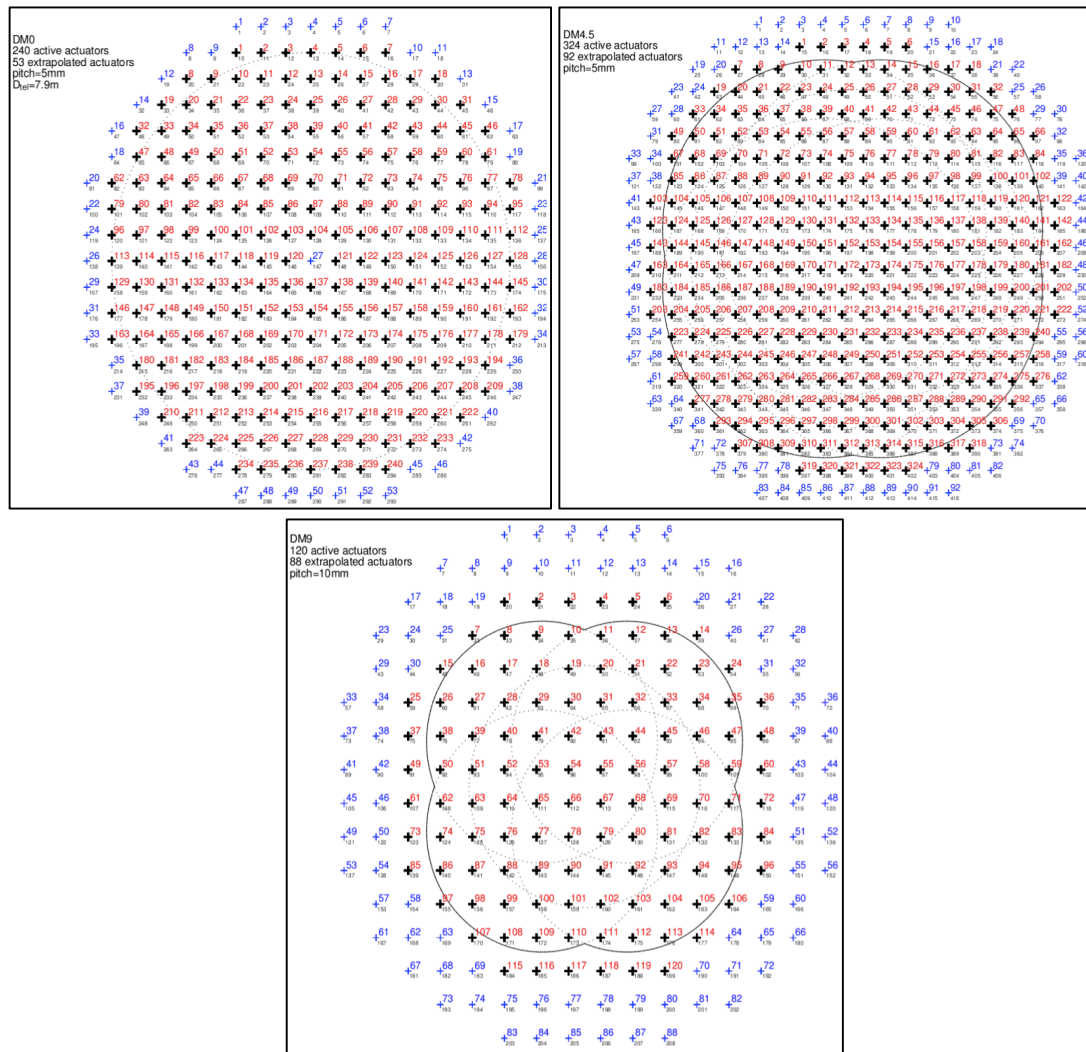


Figure 3-4: Layout of the DMs, black crosses show valid actuators, blue crosses show slave actuators (top-left: DM0; top-right: DM4.5; bottom: DM9). From the Gemini website (<http://www.gemini.edu/?q=node/11751>)

Because of the variations in altitude of the LGS (varies from 90km (at zenith) to 180km (at 60 degrees from zenith)), plus the natural variation of the sodium layer altitude, adjustments for the LGS WFS were needed. The LGS WFS zoom and translation stepper motors accomplish this.

The NGS and LGS sources simulators (calibrations sources, see Figure 3-3), correspond to five laser guide sources of 0.8'' (500 [μm] in the f/16 entrance focal plane), that can be inserted in the optical axis, to simulate sources from

90km to 160km. Six natural guide sources of 0.6'' (300 [μm]) and conjugated to infinity are used for the calibration of the NGS-WFS. Twenty-four diffraction limited NGS (10 [μm]), can be used for the calibration of the non-common path aberrations (NCPA) calibrations and performance evaluation.

3.2 Data Format

GeMS uses a CCD-based Shack-Hartmann WFSs made of quad-cells. The dynamic range of the distortions measured by each sub-aperture is so large for the open-loop data that the WFS will work in the non-linear zone with highly saturated regime (Matthias Schöck, Le Mignant, Chanan, Wizinowich, & van Dam, 2003). For the TT closed loop, the distortions measured by the WFS are small, and it operates in the linear or close-to-linear regime.

The five WFS are identical: 16x16 sub-apertures (256), 204 of them being fully illuminated at any time (valid) (see Figure 3-5). It produces 2040 values of slopes, considering it delivers the slopes on x-axis and y-axis. The pixel size is about 1.38 arcsec.

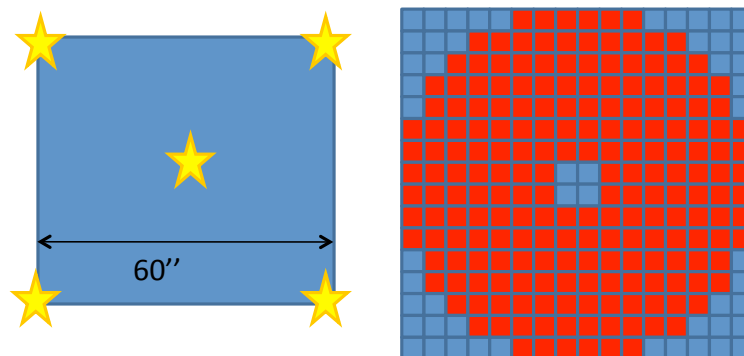


Figure 3-5: Left: Asterism on sky of the 5 LGS. Right: WFS geometry, the red are the 204 valid subapertures.

As we mentioned before, GeMS can operate at a frame-rate of 800 Hz, but the data provided by GeMS for this work are at lower frequencies and come in two types: the “circular buffer” (CB) that stores up to 24000 frames (data stored between 200-800 Hz), and the C_n^2 data (or RTD) that stores up to 3000 frames

(and data is stored at around 40 Hz). The CBs contains all system data for periods of 30 seconds.

Due to the photon return needed to operate the system, the operation frequency varies according to this flux and can decrease down to 200 Hz. The system works typically with about 140 photons/subaperture/frame at 200 Hz. This corresponds to 35 photons/pixel/frame, as the WFS are quadcell with a readout noise of 3.5 electrons. For the slower frame-rates, a large servolag error was obtained (Rigaut & Neichel, 2012).

Because we need to work within the linear range of the WFSs, the only useful data are the ones obtained in close loop. The measured slopes will thus only contain the residuals after correction. The SLODAR method needs to measure the full slopes to be able to measure the turbulence, so a reconstruction of the slopes is needed. This is done through the pseudo open loop (POL) reconstruction, which consists in adding the slopes of the residuals to the DM voltages projected into the slope domain by means of the interaction matrix (static response of an AO system) of the system. The equation that does this is:

$$S_{POL}(t) = S_{res}(t) + iMat \cdot V_{act}(t - 1) \quad (3.1)$$

where t correspond to each individual frame for the discrete time, and V_{act} is the command sent to the DM. Then, for the CB data we need at least 3 files: the one that stores the commands for the DM, the one that samples the slopes and the one that contains the interaction matrix. The vectors slopes $S_{res}(t)$ and voltages $V_{act}(t)$ for a given frame t are column vectors with the following structure:

$$S_{res}(t) = \begin{pmatrix} x_{WFS0}(t) \\ x_{WFS1}(t) \\ \vdots \\ y_{WFS0}(t) \\ y_{WFS1}(t) \\ \vdots \end{pmatrix} \quad (3.2)$$

$$x, y_{WFSi}(t) = \begin{pmatrix} Xslope\ 1, WFSi(t) \\ \vdots \\ Xslope\ 240, WFSi(t) \end{pmatrix} \tag{3.3}$$

$$V_{act}(t) = \begin{pmatrix} Voltage_{1,DM0}(t) \\ \vdots \\ Voltage_{240,DM0}(t) \\ Voltage_{1,DM4.5}(t) \\ \vdots \\ Voltage_{324,DM4.5}(t) \\ Voltage_{1,DM9}(t) \\ \vdots \\ Voltage_{120,DM9}(t) \end{pmatrix} \tag{3.4}$$

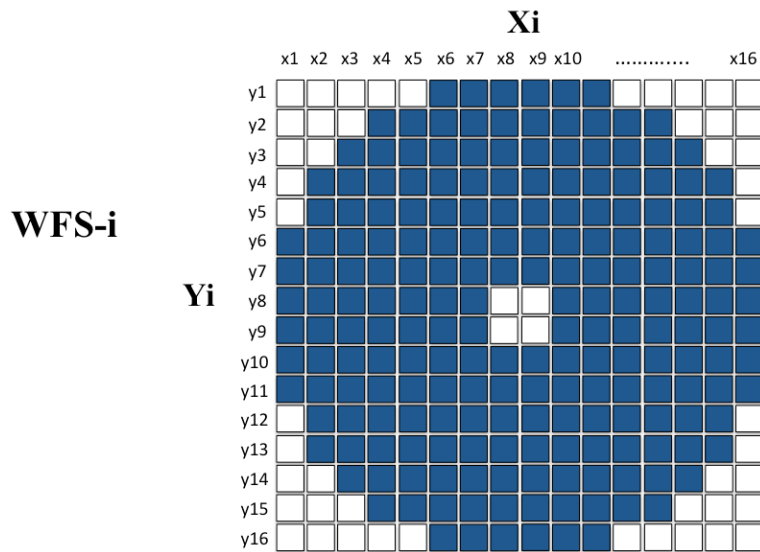


Figure 3-6: Generic WFS-i, the slopes are separated in x and y, the blue squared are the 240 valid subapertures.

For the RTD, the data is stored in two files one containing the slopes and commands and the other containing the interaction matrix.

The number of actuators for the DM, if we consider only the valid actuators from Table 1, is 684. Then the size of the interaction matrix is 2024 x 684. It reflects

the effect on the measured slope when a unit control signal is applied to the corresponding actuator, that is, it characterizes the mapping between the DMs and the WFSs.

3.3 The SLODAR approach modified for multiple LGS

As it was the most convenient method for MCAO system using the LGS constellation, we based the work on the SLODAR technique to measure the turbulence by triangulation of the layers. Due to the finite distance of the artificial stars, we have to consider the altitude z (90km) in the equation to describing the profile vector, and by an elemental trigonometric law, (see Figure 3-7) the layers move closer to each other for increasing altitudes.

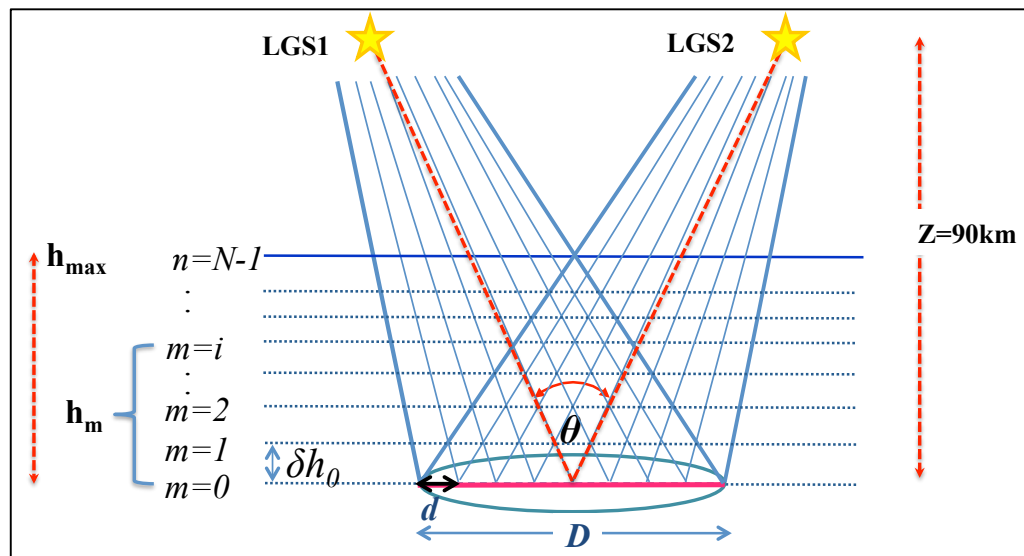


Figure 3-7: Distribution of the layers in the modified SLODAR, using LGS. N is the number of subapertures.

The altitude of these discrete layers for a pair of LGSs differ from the normal SLODAR, and when is pointing to the zenith, considering that angular distance of the LGSs is θ , the equation is given by:

$$h_m = \frac{mdz}{z\theta + md} \quad (3.5)$$

where m is an integer between 0 and the number of subapertures minus one, d is the size of the sub-aperture at the ground level, z is the altitude of the LGS, and θ is the relative angular separation of the two stars see Figure 3-7 . If we compare this equation with the usual equation for the SLODAR (2.39), it is easy to see that the sampled altitudes are lower, and the separation between layers is approximately:

As the stars are located at a finite distance (assumed at 90 Km), the light from the star cannot sample the full turbulence that is seen by the natural stars, located far enough to be consider at infinity, the finite distance to the stars means that the light from the guide stars forms a cone. This cone effect reduces the area illuminated by the guide star at higher altitudes. According to equation (3.5), this effect also reduces the separation of layers (δh_m) for the higher bins. By differentiating equation (3.5), it can be shown that this separation or bin width can be approximated to:

$$\delta h_m = \frac{dz^2\theta}{(z\theta + md)^2} \quad (3.6)$$

As it was pointed out before, the resolution for the sampling in altitudes depends on the angular separation of the stars in the sky. In GeMS configuration, we have three different angular separations: the main separation is 60 arcseconds, and the secondary's are 84.9 arcseconds and 42.4 arcseconds, as shown on Figure 3-8.

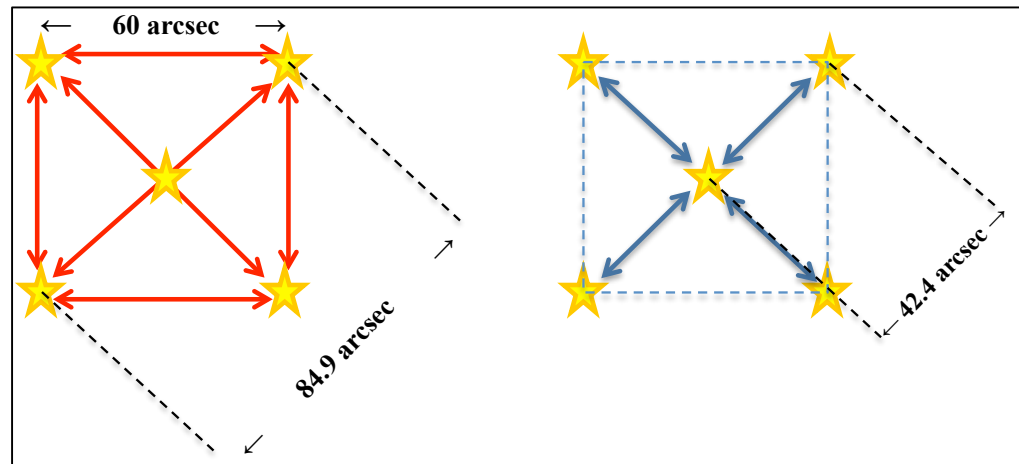


Figure 3-8: Angular separations at GeMS. The red arrows correspond to the high resolution, and the blue arrows correspond to the low resolution. The arrows indicate the different baselines, the blue arrows correspond to the shorter baseline and the red, the larger baseline.

In Cortes et al. (2012), the three different angular separations leads to only two resolutions, that we will call high resolution (for the angular separation of 60 and 84.9 arcseconds) and the low resolution for the angular separation of 42.4 arcseconds. From these two resolutions, we can only sample the turbulence up to 32 km in the low resolution case and up to 20 km in the high resolution case.

Another problem related to multiple LGSs systems is the so called “fratricide effect” (L. Wang, Otarola, & Ellerbroek, 2010), is a phenomena, where one WFS can see the Rayleigh scatter of the adjacent LGSs. This occurs as all the LGSs are launched from a common point behind the M2. The following figure shows the fratricide effect in red:

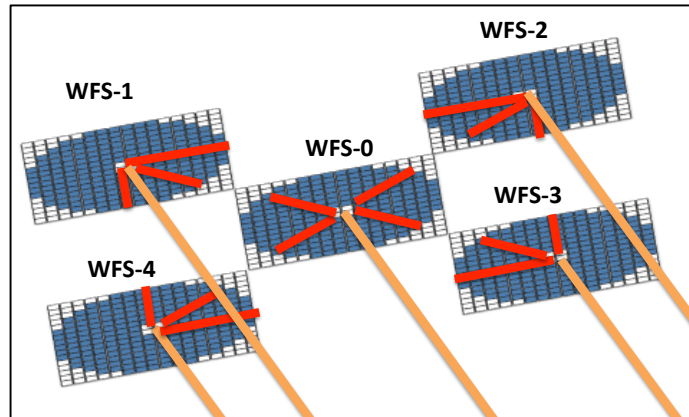


Figure 3-9: Fratricide effect. The yellow lines are the LGS beams, and the red subapertures are the contaminated subapertures on each WFS.

The problem with this fratricide effect is that the saturated subapertures cannot be used for data analysis. There is also a problem with the subapertures on the outer ring of each WFS, which are partially illuminated, creating unreliable measurements. In order to mitigate this problem, a mask is applied to each WFS to eliminate these subapertures.

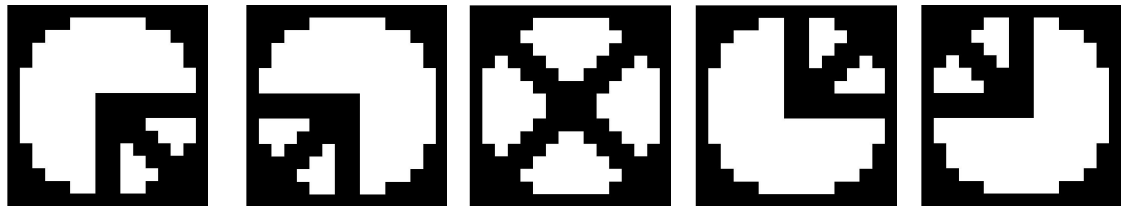


Figure 3-10: Masks defined for each WFS, to eliminate the problematic subapertures. From left to right: M-WFS1, M-WFS2, M-WFS0, M-WFS4 and M-WFS3. Masking reduces the valid subapertures from 204x5 to 640.

When reducing the number of valid subapertures, we also reduced the number of possible correlations, hence decreasing the maximum altitude that can be sampled.

Table 2 gives the altitudes for each layer, the number of possible correlated subapertures considering only the valid subapertures, the number of possible correlated subapertures considering the mask for two WFS of the corners, and the number of possible correlated subapertures considering the WFS from one

corner and the middle one. This gives us the maximum of altitude that we can probe, considering the fratricide effect and the problem of the partially illuminated subapertures of the outer ring.

Table 2: Altitude of the sampling and number of overlapping subapertures. The first overlap corresponds to the subapertures without masking, and then the overlaps corresponding between two in the edges (WFS1-4), and then overlap between the center and the edge (WFS1-0).

Layer	Altitude $H_{res}[m]$	Altitude $L_{res}[m]$	Overlap	Overlap WFS1-4	Overlap WFS1-0
0	0	0	204	108	92
1	1687	3311	186	94	80
2	3311	6387	168	82	68
3	4877	9252	152	74	54
4	6388	11928	136	66	34
5	7845	14432	120	55	24
6	9253	16780	104	40	18
7	10613	18987	90	35	18
8	11928	21064	80	28	16
9	13201	23024	70	23	8
10	14432	24875	56	20	2
11	15625	26627	44	17	0
12	16781	28728	32	12	0
13	17901	29862	22	6	0
14	18987	31358	12	0	0
15	20042	32782	6	0	0

After the previous masking of the data, the time-average of the centroids and piston voltages were moved, to get rid of the tip-tilt, guiding errors or windshake effects. Focus was already removed from the data (Neichel et al., 2012).

4. SIMULATIONS

In this chapter, the methods and algorithms used in the process for simulating the atmospheric turbulence and the telescope are explained.

The computational software used to run the simulations is MATLAB. An important step corresponded to testing what results would be expected with the analysis of real data. We first need to model the system and to simulate its response, without having to enter immediately in the expensive process of using a real AO system.

The parameters used to model the telescope were the ones that characterize GeMS and the Gemini South Telescope:

Table 3: Main parameters used for modeling the GeMS telescope.

Parameter	Value
Size of the primary mirror	8 [m]
Wavelength of the laser	0.589e-6 [m]
Number of subapertures	16
Separation between stars on sky	60 arcseconds, 30 arcseconds
Altitude of the laser star	90000 [m]

This important step corresponded to being able to simulate and predict the behavior of the system.

4.1 Simulating the turbulence

Phase screens were generated to simulate the turbulence. The most basic approximation corresponds to a single phase screen located at the entrance pupil of the system. This basic model would work for a SCAO system, but for a MCAO one needs to consider the non-isoplanatic effects, and will thus require several phase screens, at least one for each layer must be considered. As was explained before, we assumed the concept of frozen flow turbulence, requiring several numbers of discrete layers, with no turbulence between layers.

We created a phase screen for each layer given in Table 2. For each phase screen, we generated a matrix filled with Gaussian random numbers, with zero mean and unit variance, then multiplied it by the square root of the PSD (2.10). The piston was set to zero ($\Phi_\phi(\kappa) = 0$, for $\kappa = 0$). The discrete Fourier transform of the matrix was computed, and the real component used as the phase screen (McGlamery, 1976). To compute the discrete FTs, we used the Fast Fourier Transform (FFT), which required the size (dimension) of the matrix to be a power of two.

$$\varphi(r) = F^{-1} \left[H(f)F(f)^{1/2} \right] \quad (4.1)$$

were $r = (x, y)$ is the spatial vector and $f = (f_x, f_y)$ is the frequency vector, $\varphi(r)$ is the simulated phase screen, H is the complex hermitian (0,1) random noise.

The size of the screen should be large enough to simulate several data sampling, while moving across the screen and simulating the wind direction. Generating big phase screens was also necessary to overcome the problem of periodicity of the FFT (Assémat, Wilson, & Gendron, 2006), solved by using only a small region of the screen.

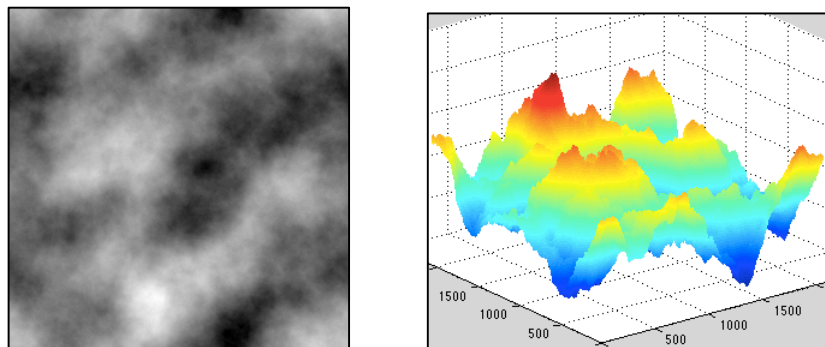


Figure 4-1: Phase Screen generated using the Kolmogorov PSD (left) and the phase in 3D (right).

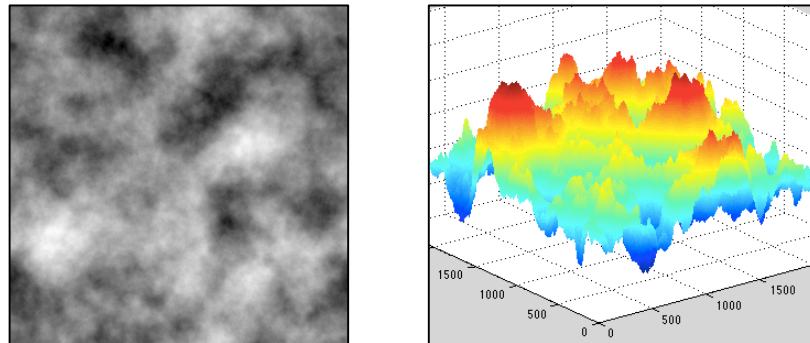


Figure 4-2: Von Karman phase screen (left) and the phase in 3D (right). $L_0=125$ m.

In Figure 4-1 and Figure 4-2, we show two different phase screens generated with the PSD of Kolmogorov (Figure 4-1), and Von Karman (Figure 4-2) with an outer scale of 125 m and both with $r_0 = 20$ cm at 500 nm.

For the simulations of the altitude layers in MCAO system, we had to increase the size of the pupil, now called meta-pupil, to consider the separations between what each WFS sees, as represented in Figure 2-12. For our specific case, with square detectors observing in the asterism configuration presented in Figure 3-5, Figure 4-4 is showing the example of the sampled area and meta-pupil for the altitude layer 11.

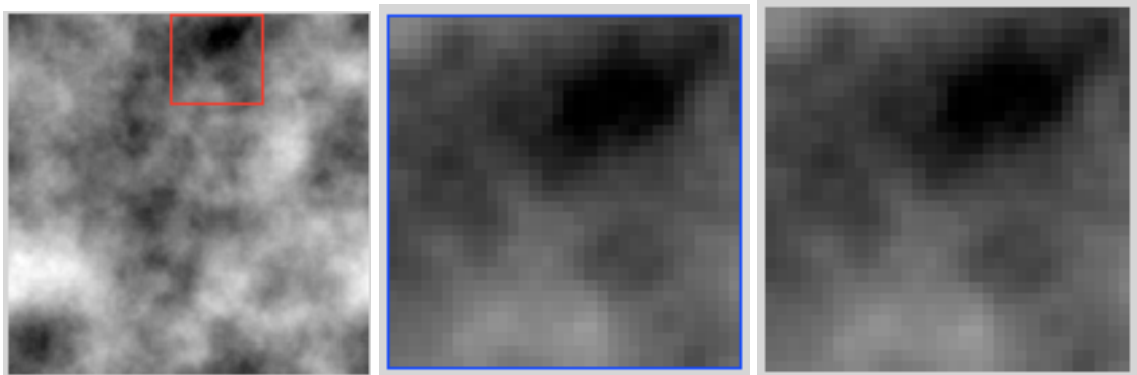


Figure 4-3: Ground layer turbulence (layer 0). Left: the full phase screen, the red square is the sampled area for one frame. Middle: the metapupil for the ground layer, i.e. only the pupil had all WFS are looking at the same area. Right: WFS0.

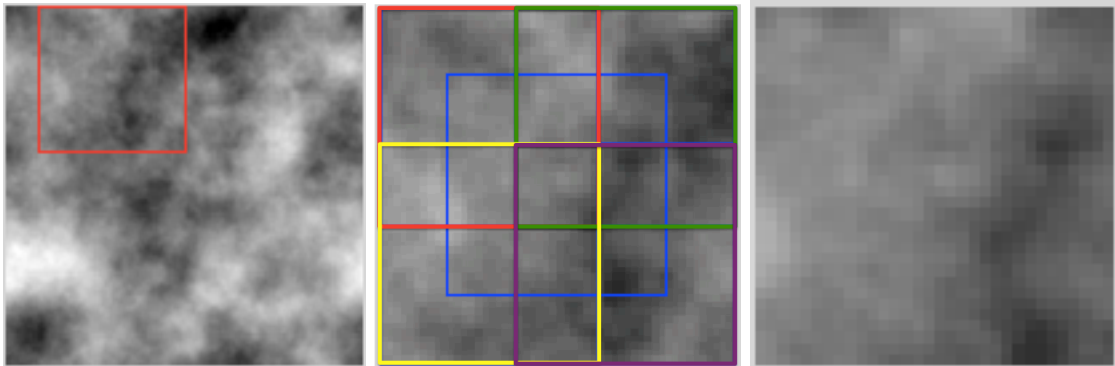


Figure 4-4: High layer turbulence (layer 11). Left: full phase screen, the red square is the sampled area for one frame. Middle: the metapupil, here in blue are the 5 squares corresponding to each WFS. Right: WFS0 corresponding to the center blue square.

4.2 Simulating the WFS of GeMS

The GeMS' WFSs are made of quadcells, and the turbulence has thus to be divided in at least 2×2 pixels per sub-aperture. The size of each WFS is 16×16 sub-apertures. We generated a phase screen of 32×32 pixels for each individual frame for the turbulence at the ground layer, and then increased by two pixels on each side for every following layer (see Figure 4-3 and Figure 4-4).

We then transform the turbulence into slopes, representing the phase difference across the sub-aperture, as measured by a quad-cell. For this we used the Fried's geometry in arcseconds (see Figure 4-5). One can note here that there are other models available, like the Hudgin geometry and the Southwell geometry (Zou & Rolland, 2006). A total of 10000 frames of slopes are generated for each simulation of layers, and for each one of the 16 layers. This process is computationally intensive, depending on the machine used. This can be improved in the future using parallel programming in a computer with multi-core.

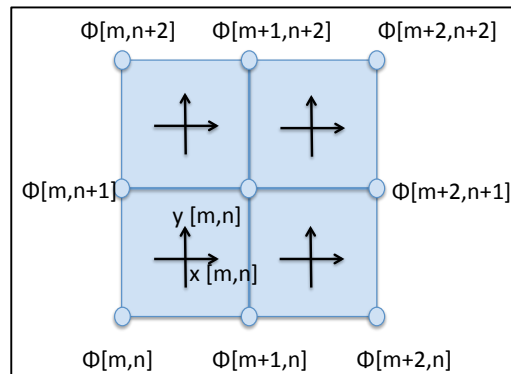


Figure 4-5: Fried Geometry, where the arrows are the slope measurements, and points represent the grid.

5. THE METHOD: SLODAR FOR MCAO WITH MULTIPLE LGSS

The method is based on the SLODAR proposed by Wilson (R. Wilson, 2002), and it consists of by optical triangulation, determine the strength of turbulence as a function of the altitude. A pair of stars are observed by a WFS, the images are cross-correlated, in this case we cross-correlate the slopes of five WFSs. The resulting cross-correlation is equal to the turbulence profile convolved with a response function. And then, deconvolving or fitting to this response function can recover it.

Then, the first step corresponds to the generation of the theoretical cross-correlation, using the simulated slopes of the previous section, generated with a simulated Kolmogorov turbulence and the GeMS geometry.

The theoretical cross-correlation matrix is a matrix (2040 x 2040) that corresponds to the impulse response function. As this matrix is redundant, we remove the repeated values to reduce the calculation time, creating the theoretical covariance map (the same process is performed for the measured slopes).

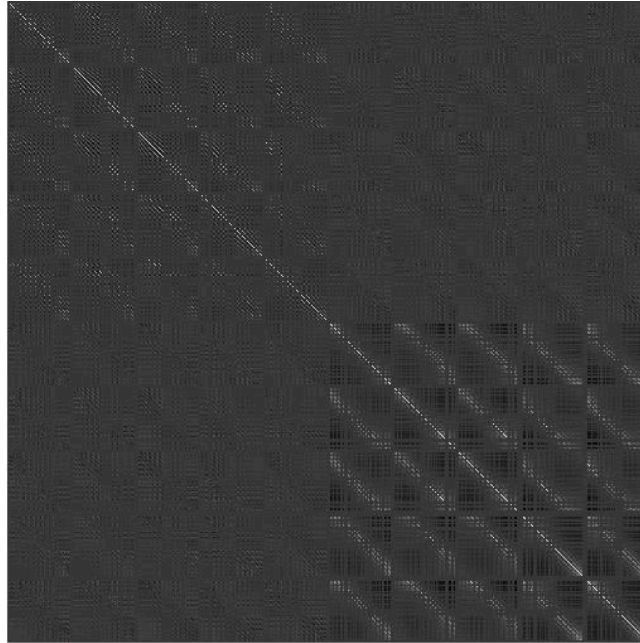


Figure 5-1: Cross-correlation of the measured slopes, for layer 4. The slopes are sorted like $X_0, X_1, X_2, X_3, X_4, Y_0, Y_1, Y_2, Y_3, Y_4$ (see Figure 3-6). The diagonal line corresponds to the autocorrelation. It can also be seen that the image is conformed by four squares, the first left-top correspond to the cross-correlation between X-X (WFS1-5), the right-top correspond to the cross-correlation between X-Y, the left-bottom correspond to the cross-correlation between Y-X, and finally the right-bottom correspond to the cross-correlation between YY.

The cross-correlation of the slopes (Figure 5-1) can be reduced, by grouping the data that are spatially redundant, using the covariance maps (Vidal et al., 2010) (see Figure 5-2). This gives is a smaller matrix (330 x 330) that is easier to manipulate and allows also a more intuitive representation.

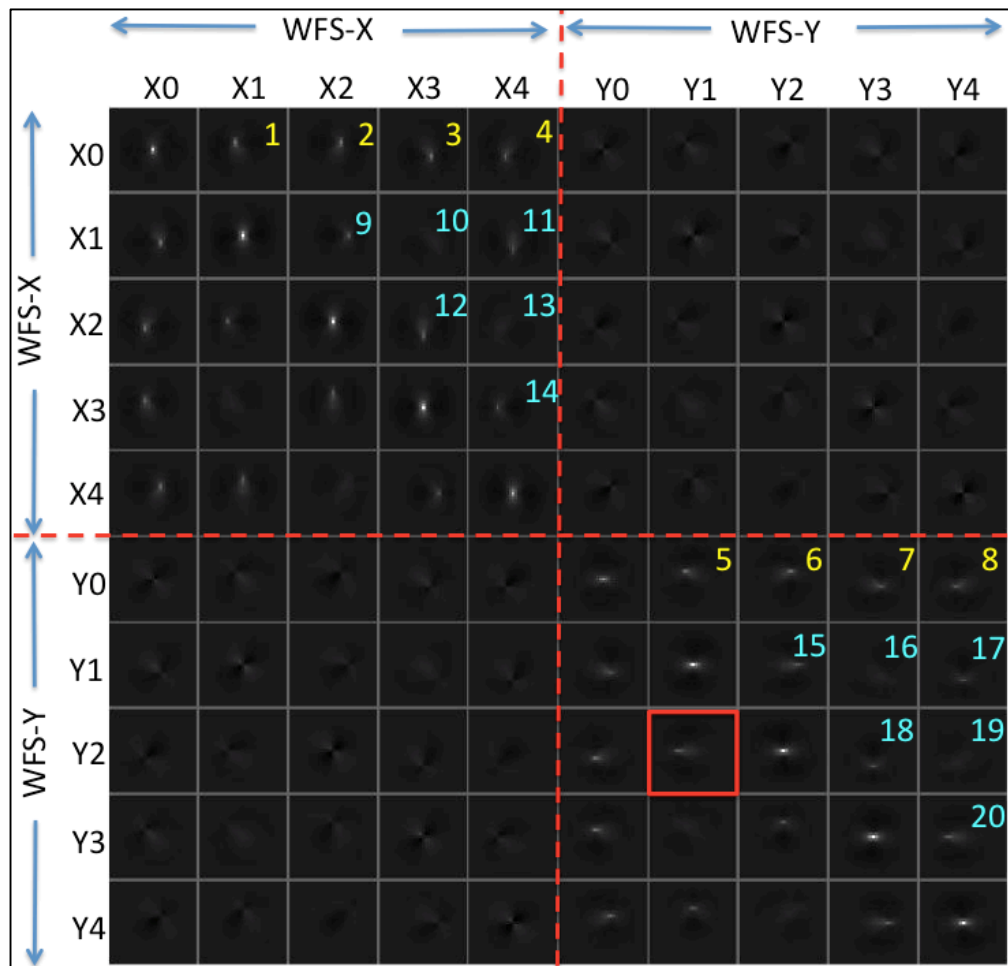


Figure 5-2: Covariance matrix for layer 7. The relevant data in the technique correlation between measurements on the same axis (X with X, and Y with Y). This symmetrical matrix contains 10x10 submaps. The diagonal correspond to autocorrelations for each of the five WFSs

The covariance map shows us the impulse response of the altitude of the layer. Figure 5-2, shows the covariance matrix for the layer 7; the corresponding altitudes are 10.6 km for the HR combinations and 19 km for the LR pairs. The diagonal groups correspond to autocorrelations for each of the five WFSs and the off-diagonals contain the cross-correlations of each of the WFS slopes with every other WFS slope. Two characteristics are clear from the figure: (i) due to a smaller optical overlapping between WFSs, the magnitude of the correlation peaks reduces for the cross-correlations in comparison to the auto-correlations;

and (ii) the peaks in the cross-correlations are displaced from their center according to the relative positions (baseline) of the correlated WFSs, that is, for the theoretical submap corresponding to bin 0, the peaks are all centered, whereas the submaps corresponding to the layer 7 (for example) have a peak displaced from the center by 6 pixels in the direction relative to the two WFSs.

The submaps of interest are those that correlate slopes in the same direction (i.e. X with X and Y with Y). Cross-correlations between X and Y slopes are generally weaker and they are not considered in this work.

Due to symmetry there are only 20 non-redundant submaps that we use (numbered in Figure 5-2). These submaps are grouped in two sets: the low altitude resolution submaps (LR submaps 1–8) and the high altitude resolution submaps (HR submaps 9–20). The LR submaps correspond to the shorter baselines in the asterism (42.4 arcseconds, see Figure 3-8).

So if we take by example only submap, and compare it for all the layers, we can see how it responds (see Figure 5-3).

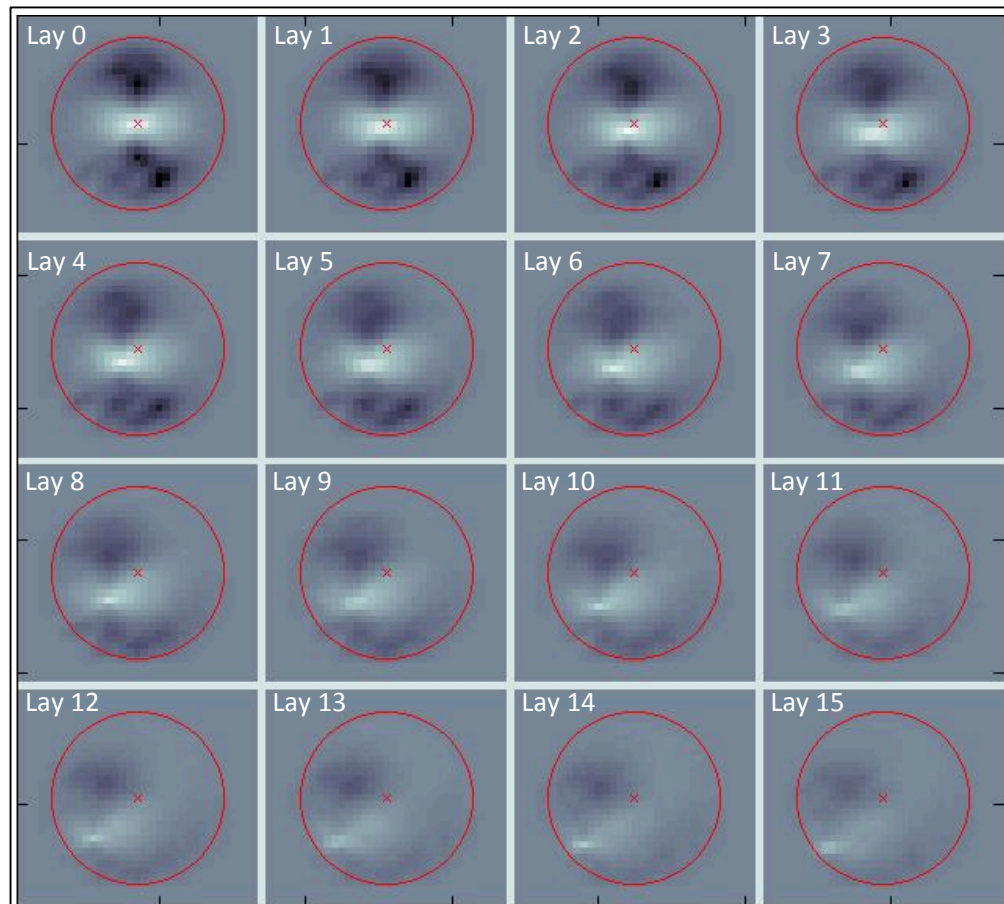


Figure 5-3: Covariance map corresponding to Y1-Y2 (red squared submap on previous figure), beginning with layer 0 in the top-left corner and ending with layer 15 in the bottom-right corner.

The previous figure shows how, for the turbulence at ground layer 0, the first submap correspond to a peak in the center (this is true for all submaps), and how it is moving far from the center as we increase in altitude. The intensity of the peaks also decreases as the number of correlated subapertures decreases (see Figure 5-4). You may also notice that the displacement direction is according to the relative position between the correlated WFS (baseline), and the displacement of the turbulence.

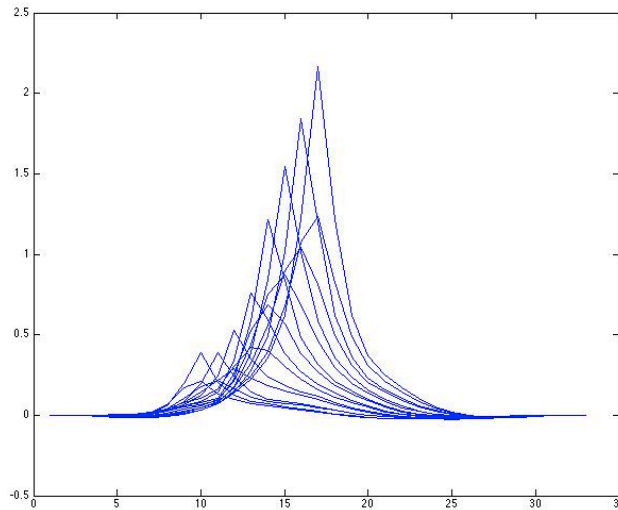


Figure 5-4: A section of the same submap Y1-Y2 from Figure 5-3, all superimposed. A decrease in the maximum intensity is observed for upper layer together with a displacement from the center.

From the covariance map (Figure 5-2), we only selected the 20 submaps that are non-redundant, keeping only the ones that are numbered in the figure. The low resolution submaps correspond to the short baseline, i.e. between the center WFS and the ones in the corners (the blue arrows in Figure 3-8). These are represented by the numbers in yellow from 1 to 8, $M_{lay,LR}^{sim} = \{M_{lay,1}^{sim}, \dots, M_{lay,8}^{sim}\}$. The HR submaps correspond to the longer baselines in the asterism (red arrows in Figure 3-8). They are the correlations of all possible WFS pairs, excluding WFS0, and are represented by $M_{lay,HR}^{sim} = \{M_{lay,9}^{sim}, \dots, M_{lay,20}^{sim}\}$.

5.1 Estimating the Cn2 in altitude (turbulence profiling)

When we fit the impulse response functions to the real data, the resulting weights describe the contribution of each layer to the total turbulence strength measured by the WFSs, that is, the turbulence profile.

To eliminate the noisy subapertures (edge and fratricide), the data is filtered with the previously defined mask. The mean slope is then removed, to cancel the effect of common motions (remaining tip-tilt and guiding errors).

From the measurement data, we get only one covariance map, similar to the one on Figure 5-2, and the submaps will be referred as M_j^{meas} . To get the profile, it is necessary to fit the measured data to the impulse response function calculated previously, getting the weights that will represent the contribution of each layer on the total turbulence strength measured by the WFS.

$$\min_{\omega_{LR}} \sum_{j=1}^8 W_j^\circ \left[\left(\sum_{m=0}^{L_{LR}-1} \omega_m^{LR} M_{m,j}^{sim} \right) - M_j^{meas} \right] \quad (5.1)$$

$$\min_{\omega_{HR}} \sum_{j=9}^{20} W_j^\circ \left[\left(\sum_{m=0}^{L_{HR}-1} \omega_m^{HR} M_{m,j}^{sim} \right) - M_j^{meas} \right] \quad (5.2)$$

where L_{LR} and L_{HR} are the number of the layers considered for the low resolution and high resolution cases (see Table 2), that is, $L_{LR} = 8$ and $L_{HR} = 10$. In the equations above W_j corresponds to a mask for submap j that selects only those values of $M_{m,j}^{sim}$ and M_j^{meas} with high signal-to-noise ratio (the dashed rectangle in Figure 5-5). Vectors ω^{LR} and ω^{HR} contain the coefficients that weigh the theoretical maps for the LR and HR cases, respectively. It must be noted that the operator \circ is a matrix entrywise product.

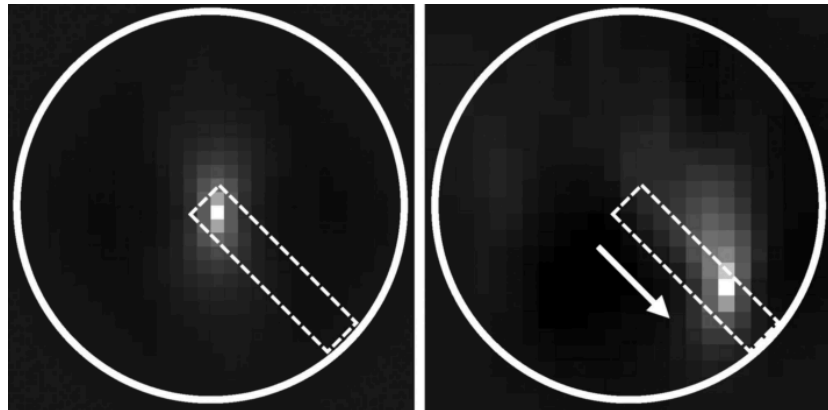


Figure 5-5: At the left is the submap $M_{0,10}^{sim}$, and at the right, the submap $M_{6,10}^{sim}$.

The profile coefficients (ω_m^{LR} and ω_m^{HR}) can be found using minimization methods based on gradient techniques or a matrix inversion approach based on the truncated least-squares technique (Golub & Loan, 1980). We found that the latter approach is faster than a gradient search, and it always converges to a global minimum. A description on how this technique is applied to the minimization problem follows.

Let us define $P_{m,j}$ as a vector containing the result of masking theoretical covariance submap j in bin m as described in Figure 5-5,

$$P_{m,j} = \{W_j^\circ M_{m,j}^{sim}\} \quad (5.3)$$

The parenthesis $\{\}$ indicates that the non-zero elements in the resulting matrix are reordered as a column vector. Vectors $P_{m,j}$ are concatenated vertically according to their submap index and the process is repeated for all simulated layers j that are copied horizontally, resulting in matrices for the LR and HR cases with the form:

$$P^{LR} = \begin{bmatrix} P_{1,0} & \cdots & P_{1,L_{LR}-1} \\ \vdots & \ddots & \vdots \\ P_{8,0} & \cdots & P_{8,L_{LR}-1} \end{bmatrix}; \quad P^{HR} = \begin{bmatrix} P_{9,0} & \cdots & P_{9,L_{HR}-1} \\ \vdots & \ddots & \vdots \\ P_{20,0} & \cdots & P_{20,L_{HR}-1} \end{bmatrix} \quad (5.4)$$

The next step is the construction of the measured covariance maps that follow the same path as the theoretical ones. For a given submap j , the masked measured covariance submap is:

$$Q_j = \{W_j^\circ M_j^{meas}\} \quad (5.5)$$

And the full vector containing all masked submaps is:

$$Q^{LR} = \begin{bmatrix} Q_1 \\ \vdots \\ Q_8 \end{bmatrix}; \quad Q^{HR} = \begin{bmatrix} Q_9 \\ \vdots \\ Q_{20} \end{bmatrix} \quad (5.6)$$

Then, the contribution of each layer to the turbulence profile is:

$$\omega^{LR} = (P^{LR})^{-1} Q^{LR}; \quad \omega^{HR} = (P^{HR})^{-1} Q^{HR} \quad (5.7)$$

If no negativity constraints are imposed on the computation of the resulting profiles ω^{LR} and ω^{HR} , negative values are likely to appear (Cortes et al., 2012).

These are caused by differences in the autocorrelation functions for the measured

and simulated slopes as explained in detail in Wilson et al. (2009). The convenience and correctness about the use of these constraints is not clear for the authors. In this work, no restrictions were imposed on the profile in which the sum of the negative values was consistently less than 3 per cent of the total.

The following image shows an example of the results:

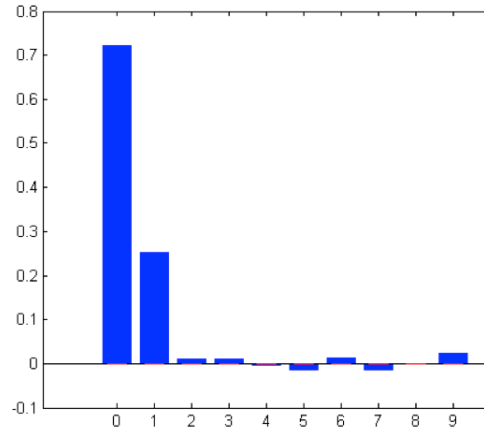


Figure 5-6: Fitting of the data on-sky, corresponding to March 25, 2011 at 06:36:59.

5.2 Absolute profile

The method described above will result in a relative profile. In order to obtain an absolute profile vector in terms of C_n^2 units, the result given by ω_m^{LR} and ω_m^{HR} requires some further processing. We know that for Kolmogorov turbulence (Hardy, 1998), the Fried parameter (r_0) can be converted to C_n^2 by equation (2.11).

The integrated turbulence over layer m is $C_n^2(m)\delta h_m$. Rearranging, we get

$$C_n^2(m)\delta h_m = \frac{2.364 \cos(\gamma) r_0(m)^{-5/3}}{k^2 \rho_m} \quad (5.8)$$

Where ρ_m accounts for the stretching in r_0 at layer m due to the cone effect. This optical spatial expansion is given by:

$$\rho_m = 1 - h_m/z \quad (5.9)$$

We also know (Fried, 1975), that the tilt variance integrated over a subaperture with diameter d is:

$$\sigma_d^2 = 0.179\lambda^2 r_0^{-5/3} d^{-1/3} \quad (5.10)$$

We now define σ_0^2 as the sum of the subaperture variances for the theoretical valid slopes, so by using the result of the minimization in equations (5.1) and (5.2), we can find a formula for the turbulence strength in layer m for the LR and HR cases:

$$C_n^2(m)\delta h_m = \frac{2.37\omega_m}{sec\gamma} \sigma_0^2 \quad (5.11)$$

5.1 The unsensed turbulence

Using the SLODAR technique, it is possible to get estimates for the unsensed turbulence (turbulence above the highest bin) and also for the noise present in the measurements.

Let us define the submaps forming the diagonal of the covariance map in Figure 5-2 as $V^{meas} = \{V_1^{meas}, \dots, V_p^{meas}, \dots, V_{10}^{meas}\}$, where p refers to the position along the diagonal (e.g. V_1^{meas} and V_6^{meas} are the measured autocovariance submaps of WFS0 slopes in the X and Y directions, respectively).

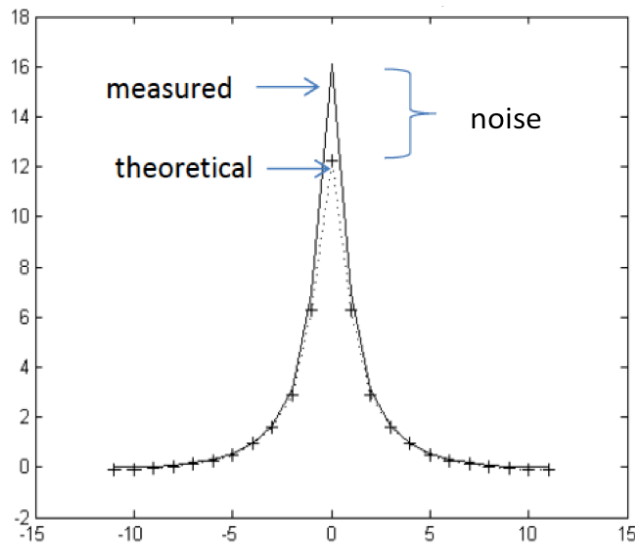


Figure 5-7: Autocovariance submap cross-section, X direction. Theoretical versus measured.

First we find the noise associated with the measurements. The central point of the autocorrelation submaps corresponds to the centroid from each subaperture correlated with itself. As the noise is therefore correlated, the central point will be equal to the slope variance plus the noise variance. As the impulse response functions are noiseless, the difference between these two points (**Figure 5-7**) can give an estimate of the noise variance. This can be estimated by:

$$\min_{\eta} \sum_{p=1}^{10} U_p^0 (\eta V_p^{sim} - V_p^{sim}) \quad (5.12)$$

where V_p^{sim} is the theoretical (simulated) autocovariance submap p and U_p^0 is a mask, that eliminates the central point of the submaps.

By eliminating the noise from the measured autocovariance submaps, we can get the total turbulence above the telescope determined as the slope variance in the five WFSs.

Finding the value of η in equation (5.12), and using equation (5.11), we can determine the total noise-free turbulence seen by the WFSs:

$$\int_0^{\infty} C_n^2(h) dh = \frac{2.37}{\sec\gamma} \eta \sigma_0^2 \quad (5.13)$$

We now subtract the sum of turbulences from the ground up to the highest measured layer (h_{max}) to obtain the unsensed turbulence as:

$$C_{uns} \approx \int_{h_{max+1}}^z C_n^2(h) dh = \frac{2.37}{\sec\gamma} \eta \sigma_0^2 - \sum_m C_n^2(m) \cdot \delta h_m \quad (5.14)$$

where z is the sodium layer altitude. Notice that C_{uns} is different for LR and HR, since m , $C_n^2(m)$ and δh_m are different in each case.

6. WIND PROFILER

Following the same idea as in the previous chapter, but performing temporal cross-correlation instead of spatial cross-correlation, it is possible to track the movement of the centroids of a set of WFS and therefore to determine the velocity of the layer. This technique has been presented in earlier work (L. Wang, Schöck, & Chanan, 2008) and proved to be a powerful method to determine the velocity of a turbulence layer, the direction and the altitude of the layer. Its use also allowed us to validate our previous technique and to get additional information on the turbulence from the same data sets.

Two techniques can be used for this analysis. One was proposed by Wang and recovers the turbulence profile from the spatio-temporal cross-correlation deconvolved by the autocorrelation of the data. The other technique is using the impulse response for a specific statistics of a model of turbulence (T. Butterley et al., 2006). The first technique needed to be modified for its use with multiple LGS/WFS, taking into account all the specificities of the GeMS data, like the fratricide effect and noisy slopes (the same masking process as described before had to be used). The used method consisted of time delayed cross-correlation between two WFS A and B , described by the following equation:

$$T^{AB}(\Delta u, \Delta v, \Delta t) = \frac{\langle \sum_{u,v} S_{u,v}^A(t) \cdot S_{u+\Delta u, v+\Delta v}^B(t + \Delta t) \rangle}{O(\Delta u, \Delta v)} \quad (6.1)$$

where $S_{u,v}^A(t)$ represents the slopes (x and y) of the WFS A, for the subaperture (u, v) at the time t , Δt corresponds to the time between two consecutive samples of data, and $(\Delta u, \Delta v)$ is the relative subaperture displacement in the WFS. $O(\Delta u, \Delta v)$ is the number of overlapping illuminated subapertures for the offset $(\Delta u, \Delta v)$, and the sum is over the all and only valid illuminated subapertures; $\langle \rangle$ represents the time averaging.

For the first method, as explained before, a 2D deconvolution is needed, using the Fast Fourier Transform (FFT), like:

$$FFT^{-1} \left[\frac{FFT[T^{AB}(\Delta u, \Delta v, \Delta t)]}{FFT \left[\frac{1}{2}T^{AA}(\Delta u, \Delta v, 0) + \frac{1}{2}T^{BB}(\Delta u, \Delta v, 0) \right]} \right] \quad (6.2)$$

At $T^{AB}(\Delta u, \Delta v, \Delta t = 0)$, it gives some peaks along the baseline A-B that will represent the turbulence in the corresponding layers. But because we deconvolve the covariance map with the autocorrelation, we only get the relative strength of the turbulence. When increasing the time interval Δt , the peaks will move depending on the wind speed and direction in the layer. Tracking the peaks movements will then provide this information.

The important point here is that we can have two or more layers too close to be separated with the SLODAR technique, but that can be distinguished with this method if they have different velocity vectors. Using this technique had an important implication in our studies of the turbulence profile by distinguishing more layers at the ground level. When analyzing the data, we found very often some peaks that remain steady for a long time, while others were moving. We realized that these steady peaks corresponded to the so-called “dome turbulence” (or dome seeing). This effect was mentioned before by Roddier and others (Timothy Butterley, 2006; F. Roddier, 1999; Shepherd, 2012). Some data set analyzed with the wind profiling technique shows a peak remaining steady in the center, and another peak moving away from the center. As both peaks are starting from the center means that the SLODAR method will detect them as belonging to the same first layer, but with the wind profiler we can identify the one that correspond to the dome seeing.

Figure 6-1 shows how the variance is very high also in the center of the image, which also indicates a strong non-moving turbulence, clearly consistent with what is called dome seeing, as it corresponds to turbulence created inside the dome of the telescope. This could be generated for example by a hot spot due to some electronics. The wind profiler thus also helps to separate effects within the same layer, but which are moving in different directions or at different velocities.

One of the first tests to validate our method was to use the data from the turbulence generated by all the DMs together, and we created a video of the corresponding temporal cross-correlation. The resulting profile was similar to the one obtained with the spatial cross-correlation, but it was easier to see the effect of the DM 9 over the data, with the stronger spot for the peak.

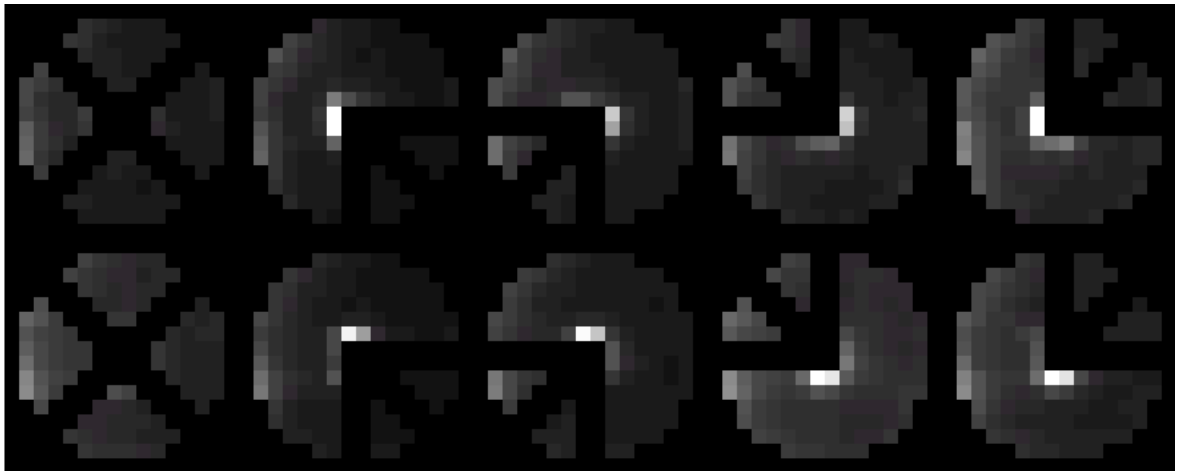
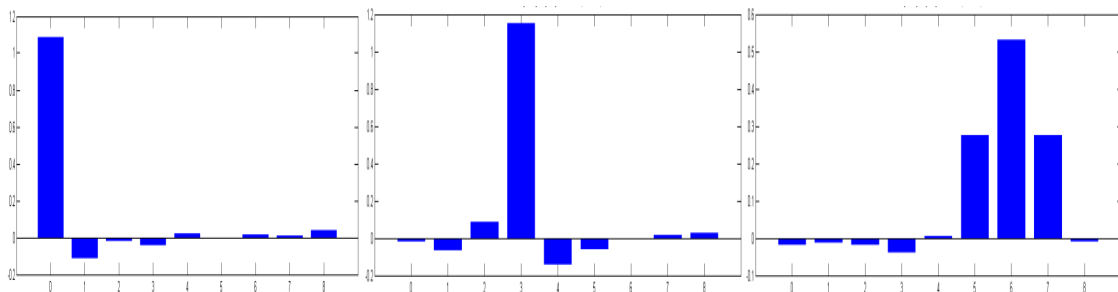


Figure 6-1: Variance of a data set, X values at the top, Y values at the bottom. The white area correspond to “hot” spots, and due are presented in all WFSs, this would be due turbulence at the ground layer.

We also compared the wind profiling method with the results obtained before; when creating the turbulence with the DMs separately and the results we got here were clearer, with an easier identification of the effect of the DM9 over the subapertures (see Figure 6-2):



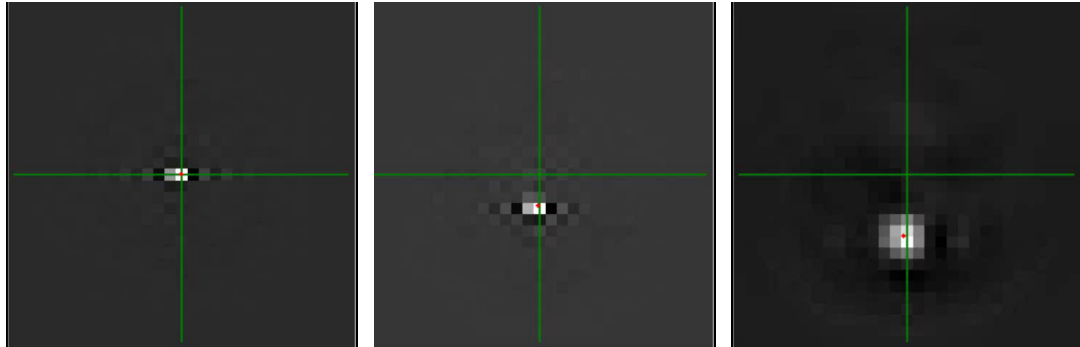


Figure 6-2: Turbulence generated by the DM independently and the profile obtained with the wind profile method. Here it can be seen that the spot of the correlation peak is broader for the DM9 than in the others, affecting the profile measurement. Left: DM0, middle: DM45, right: DM9.

For the wind profiler, the altitude of the layer H will correspond to the position of the peak at time $t=0$, as represented in Figure 6-3. Every pixel will correspond to a layer altitude starting from a central point. Then the direction of movement will depend on the geometry given by the direction of movement of the layer and the relative direction between both WFS. Determining the velocity will depend on the number of frames and the frame rate.

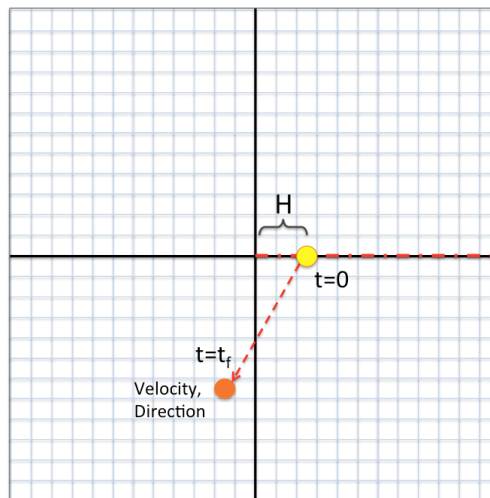


Figure 6-3: Estimation of the turbulence altitude and direction and velocity of the wind.

7. CALIBRATIONS

One of the first calibrations of the method was done with simulated data, to check that the retrieved profile corresponded to the input one. The results are presented on Figure 7-1, where we simulate a combination of layers with 20% in layer 0, 20% in layer 2, 10% in layer 4, 10% in layer 6, 20% in layer 8 and 9. The obtained profile fits perfectly with the introduced profile.

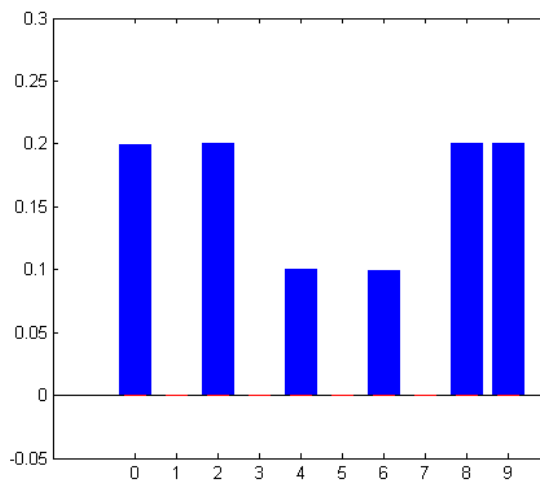


Figure 7-1: Fitting works perfectly for simulated data.

5.2.1 Deformable Mirror and quadcell

Using the CANOPUS internal calibration source and the three DMs to artificially generate turbulence at 0, 4.5 and 9.0 km, we tested the SLODAR and wind profiler in an open and closed loop. A total of 50 runs were implemented with different turbulence settings for wind speed and direction, seeing conditions (r_0) and energy distribution among the three DMs. The estimated wind and turbulence parameters were compared to the ones used to generate the turbulences, getting very good agreement. As an example, Figure 7-2 and Figure 7-3 show the results for a turbulence generated by DM4.5 with wind velocity of 30 ms^{-1} in the X direction and $r_0 = 42.0 \text{ cm}$

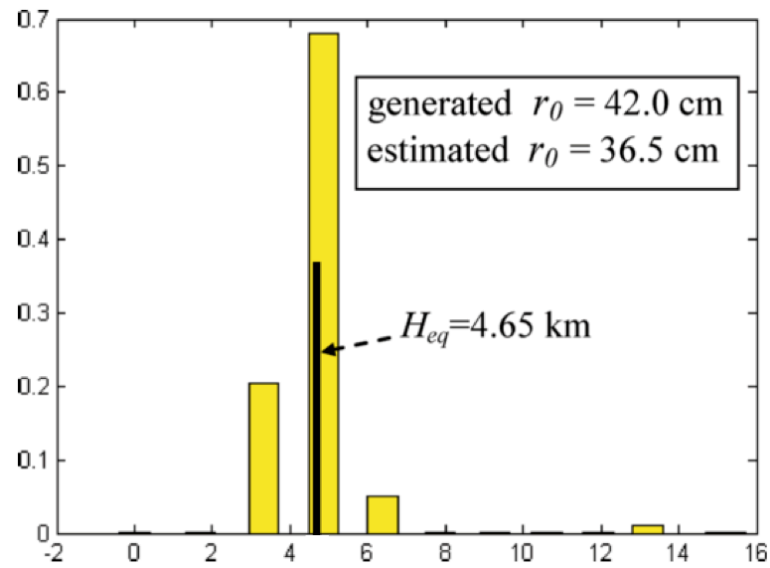


Figure 7-2: Estimated profile using the calibration source and excitation of DM at 4.5 km

The estimated values for this case were an equivalent altitude, H_{eq} , of 4.65 km (obtained as a weighted sum of altitudes), a wind speed of 30.8 ms^{-1} and r_0 of 36.5 cm.

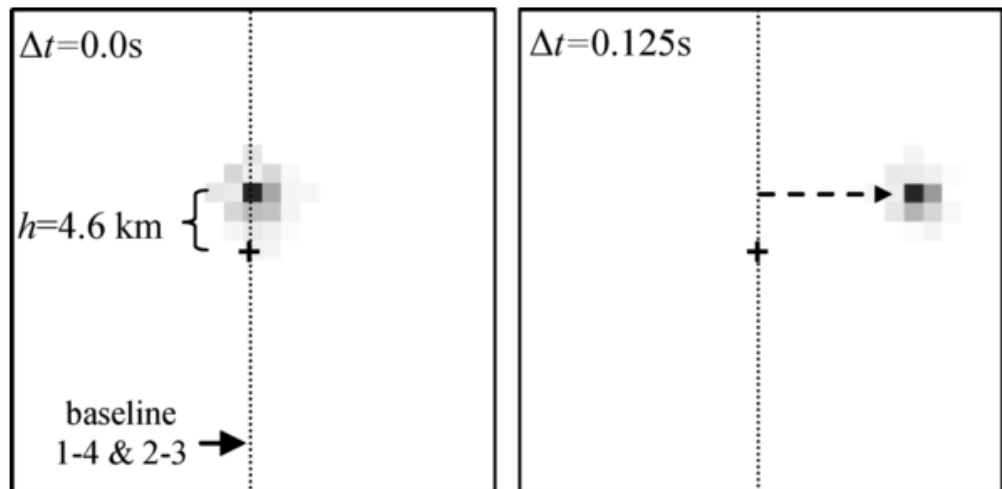


Figure 7-3: Result of the wind profiler for a turbulence generated at DM4.5 with a wind speed of 30 ms^{-1} in the X direction.

The weighted altitude estimation and wind parameters were always estimated with accuracy better than 5 per cent for all runs. However, in the case of Fried's

parameter, this was not the case and in the example presented above (worst case found) errors could exceed 10 per cent. This is thought to be caused by wrong gains in the centroid gains, that is, as stated in equation (3.1), they directly affect the errors of the POL values and hence the measured turbulence. This implies that the centroid gain of the quad cells becomes critical in the effectiveness of the method so an in-depth analysis of their error impact on the fitting accuracy is required.

The use of quadcells requires the knowledge of a calibration factor, the centroid gain, to transform the quadcell signal (unit less) into some meaningful quantity, here the spot position in arcseconds. This centroid gain is proportional to the size of the SHWFS spot, and then it will change according to external parameters such as laser intensity, sodium layer density, zenith angle, etc.

An error in the centroid gain can produce NCPA errors, differential aberrations between the WFSs, large tomographic errors and non-optimal AO loop gains.

Data were taken from the bench in a closed loop but with zero loop gain whilst applying a known turbulence on the DMs. Data in a closed loop were also taken for the same simulated turbulence and the scatter plots for two subapertures in each case are shown in Figure 7-4. A noticeable difference exists in the slope gain with respect to the ideal one and also a non-linear effect due to the quad-cell dynamic range appears at higher values of slope amplitudes. This proved to have a low impact on the results for normalized contributions of each layer to the total turbulence strength.

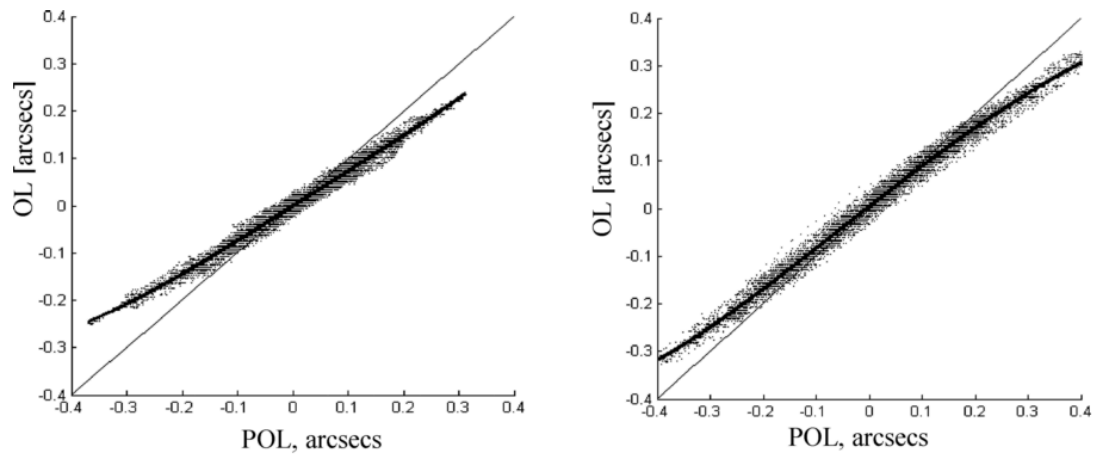


Figure 7-4: Open loop versus POL. The thin line is the ideal relationship that should be obtained; the thick line is a fourth-order polynomial fit to the data (dot cloud). Left-hand panel: WFS0 subaperture 1; right-hand panel: WFS1, subaperture 57.

A simulation analysis was carried out in order to quantify the effect of these mismatches on the fitting of the C_n^2 profile. For the HR case, the errors fell below 3 per cent for deviations in the centroid gain of up to 50 per cent with respect to the correct value. For the LR case, however, these errors jumped to 8 per cent for a 50 per cent deviation.

It is interesting to note that this error had little impact for relative profiles (normalized contributions of each layer to the total turbulence strength), for both HR and LR. Furthermore, the GeMS can calibrate the centroid gains in almost real time during on-sky operation (Gratadour & Rigaut, 2007), so the negative impact can be known and limited.

Simulations were also run for different values of the turbulence outer scale L_0 , but no significant impact was found on the result. This is not surprising, since by eliminating the tip and tilt from the POL slopes, the potential effect of differences between the theoretical and measured submaps of the lower part of the spectrum is greatly attenuated. The optimal masking to be applied to the covariance submaps shown in Figure 5-5 was also a subject of further analysis via simulation and artificially generated turbulences. The best performance in

both instances was found to be a masking that eliminates any submap pixel outside the line describing the baselines between WFSs. Artificial generation of turbulence via DMs is a powerful calibration and validation tool for the method, but it must be kept in mind that the limit imposed by the actuators' pitch over the simulated turbulence spectrum causes the impulse response of the turbulence being different from the Kolmogorov model used for computing the theoretical submaps (T. Butterley et al., 2006; R. W. Wilson et al., 2009; R. Wilson, 2002) This was clearly seen when estimating the profile using DM excitation, where negative values in some of the profile components could be equivalent to up to 2 per cent of the total turbulence.

The covariance map generated by exciting the DMs are presented in Figure 7-5 and Figure 7-6, show the covariance map obtained when exciting the DM conjugated at 0 Km and 9 Km, and what will correspond to the theoretical covariance map (layer 0 and 6). One can see their similarity.

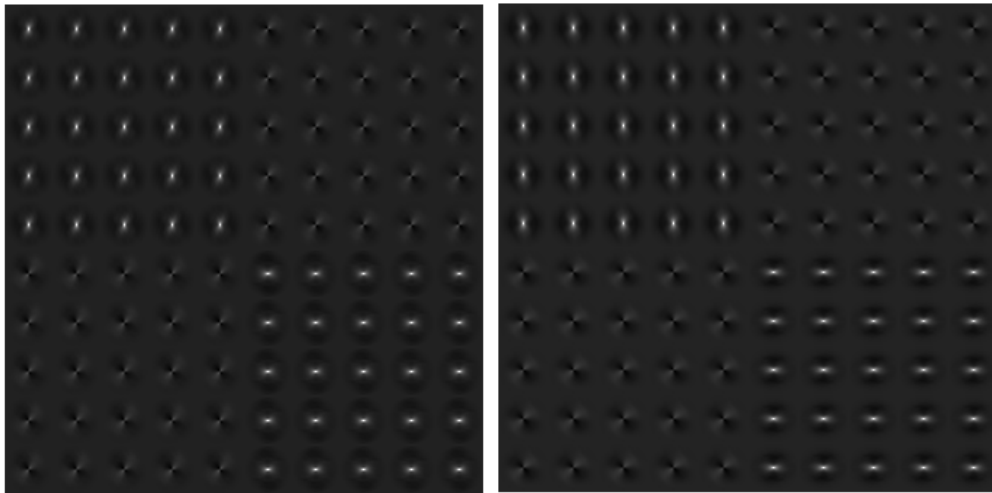


Figure 7-5: Left: Covariance map for exciting the DM0, right: Theoretical covariance map for layer 0.

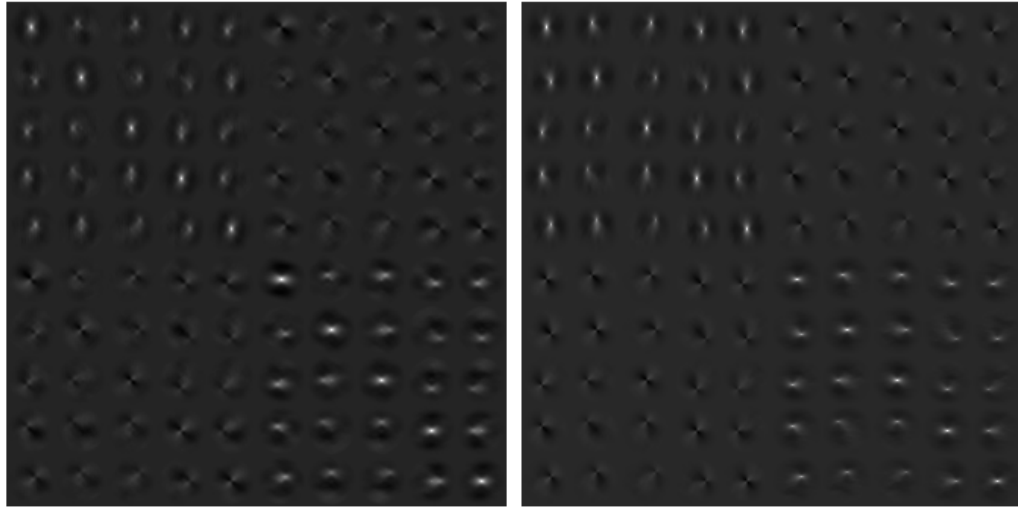


Figure 7-6: Left: Covariance map for exciting the DM9, right: Theoretical covariance map for layer 6.

Figure 7-7 presents the fitting to the data obtained by exciting the different DMs individually (represented by the red line) and the measured profile in blue. Here one can see some effects that we were not expecting: at the higher DM position, we got a broadening from the profile. This was observed neither with simulated data nor with real data.

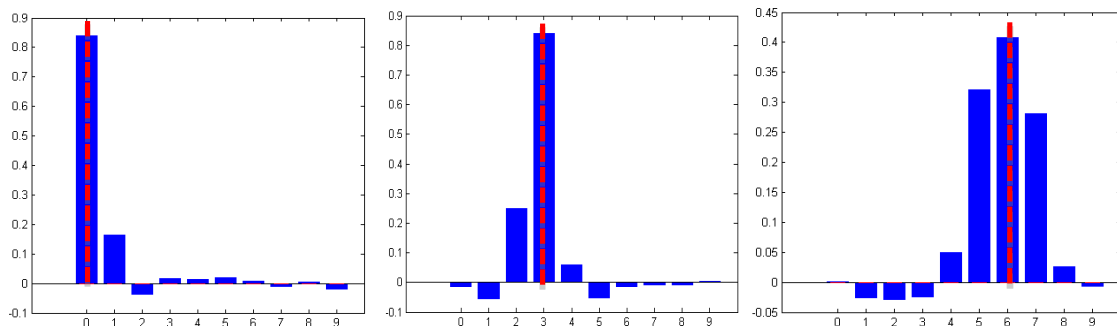


Figure 7-7: Profiles obtained (blue) when the turbulence was introduced by each DM (red dashed line) independently. First altitude average was 636m for the DM located at 0km, second was 4.477km for the DM located at 4.5 km, and the third was 9.242 km for the DM located at 9km.

8. DATA ANALYSIS

The first problem encountered when processing the data was their tremendous degree of contamination due to fratricide effect or noisy subapertures caused by partial illumination (critical in the outer ring). The final mask we defined, presented on Figure 3-10, was the result of the analysis of the real on-sky data. A plot of the standard deviation clearly allows detecting the noisy sub-apertures (see Figure 8-1).

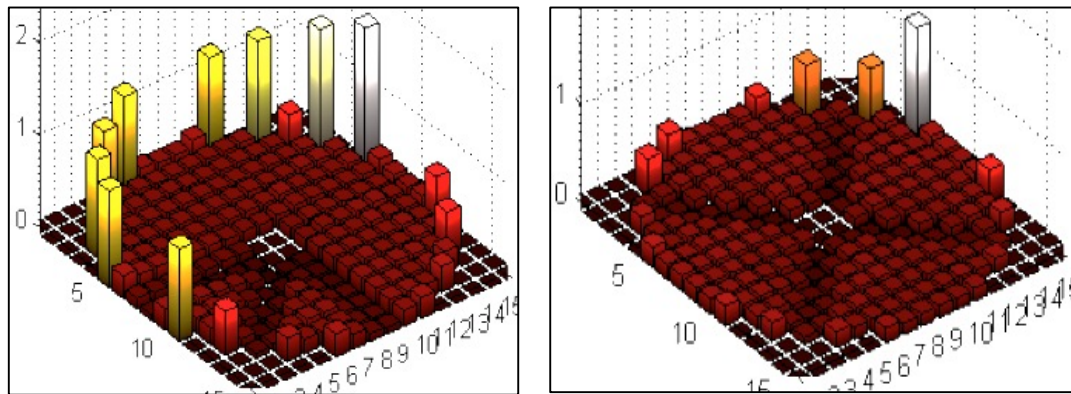


Figure 8-1: Standard deviation of the WFS2 (left) and WFS0 (right). The low values correspond to the fratricide effect, that is saturated, and the high values correspond to the subapertures that are partially illuminated.

After removing the noisy data, we performed a first level check of the data before processing them in order to keep only the ones taken in correct conditions for our study. Indeed, as the data were taken during commissioning time, they were not always taken in optimal conditions: data acquired with issues with the laser, problem with the alignment or other kind of problems that resulted in the data not being useful. The variability of the sodium layer in the atmosphere and some initial problems with the spot size of the laser also affected the data. It was also important to check that the data were taken while the AO loop was correctly closed.

Another problem was the presence of clouds during the data recording. This resulted in the scattering becoming higher and the effect could easily be seen on the WFS data, as presented by Rigaut (Rigaut & Neichel, 2011). The presence of clouds is easier to detect on the intensity sub-aperture data (Figure 8-2), but the data recorded for analysis

only contained the slopes, and it was then necessary to check the variance and average of the data to detect possible problems.

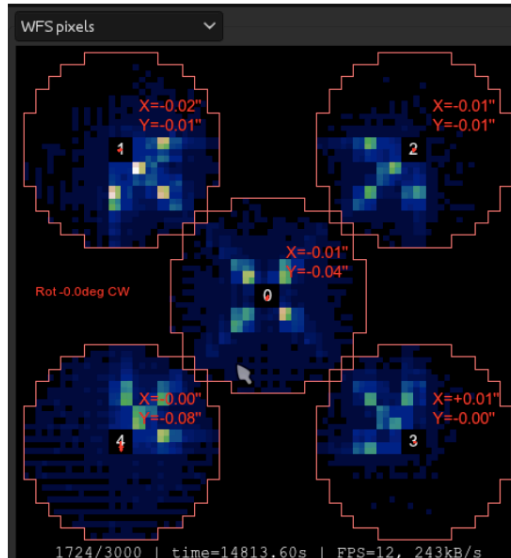


Figure 8-2: The 5 WFS subaperture intensity in presence of clouds. (Rigaut & Neichel, 2011).

During the first commissioning, it was also noticed that some actuators on the DM0 were dead, and that the dying rate was increasing, ending with up to 17 dead actuators. This required a drastic solution. It was decided to remove this DM and sent it back to the manufacturer for repair, and the DM4.5 was moved to replace it. This did not impact our previous analysis, as the only effect was a small increase in the slopes value, but most of the corrections performed by the removed DM were absorbed by the other two.

The validity check performed on the data, i.e. to include them or not in the further analysis, was based on the quality of the slopes, as was often missing information about the conditions of the night, as the data were recorded by a third person. Without extra information about the conditions or the quality of the data, was necessary to define the selection criteria, complicated by the fact that a similar effect in the data could have different origins. For example, a very high variance could be the result of clouds or open loop operation (when the gain is zero), with the possibility of having data outside of the linearity range. Fortunately, the amount of data was big enough to

perform the analysis. The data check was focused on the quality of the slopes, as can be seen in the following figure:

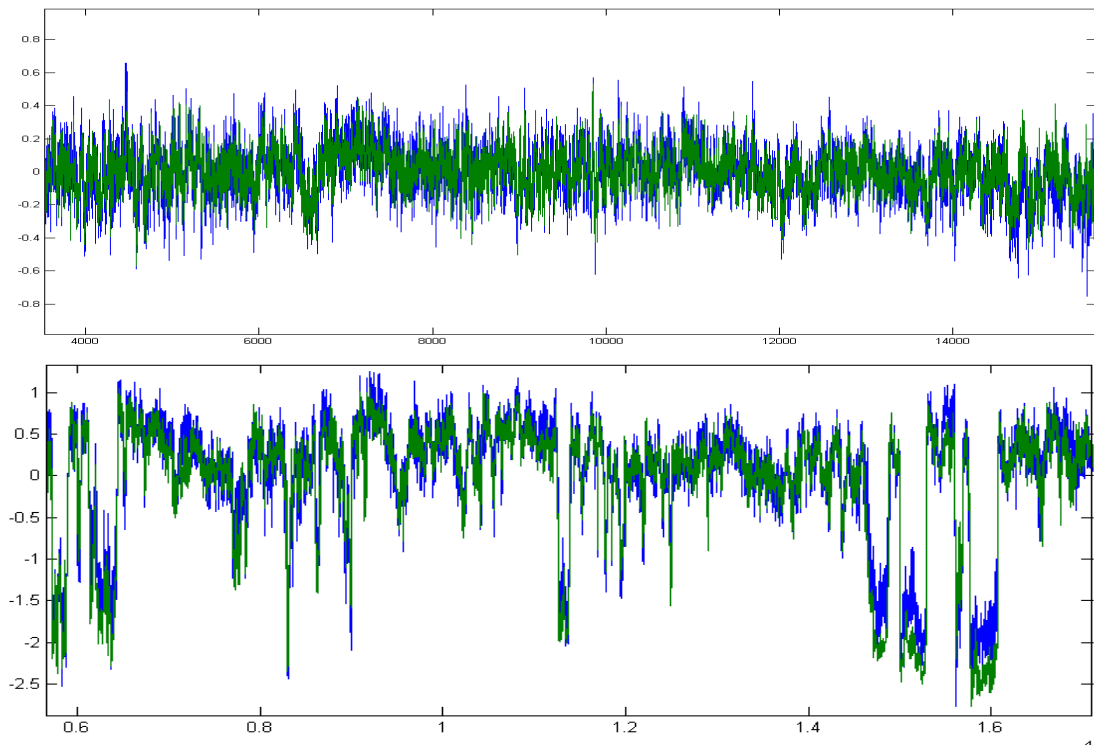


Figure 8-3: Two examples of sub-aperture slopes, top: a good set of data; bottom: a bad example of data set with high variance.

The wind profiler technique gives good results in the analysis of the turbulence profile (see Figure 8-4 and Figure 8-5). The difficulty is in the estimation of the velocity and direction of the layers, which requires to track the moving spot, which can be complicated if there is not a strong correlation between the WFSs measurements.

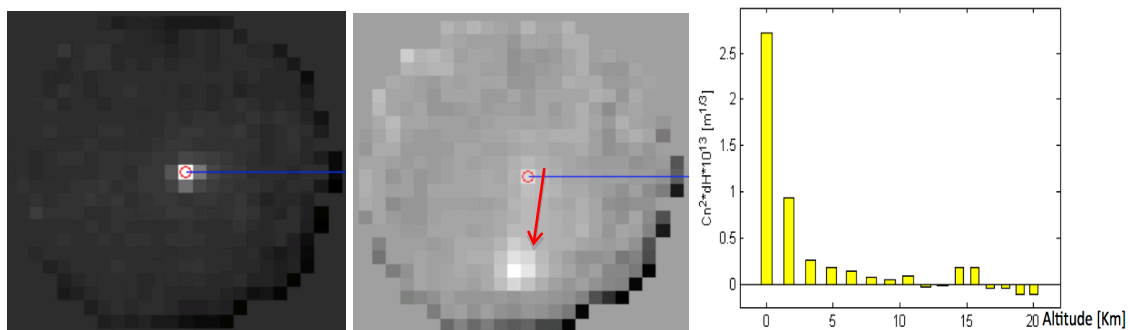


Figure 8-4: Right: Wind Profiler results, for baseline WFS1&2 and WFS4&3 (High Resolution). Left and center: temporal cross-correlation for t=0s, and for t=40s.

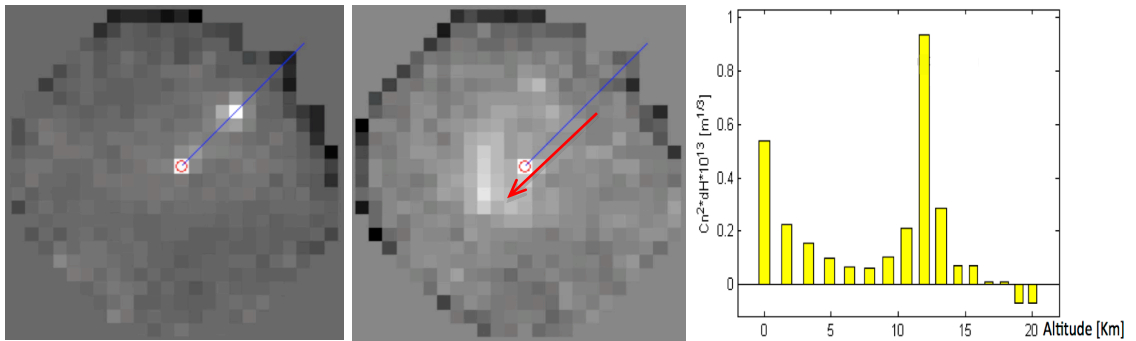
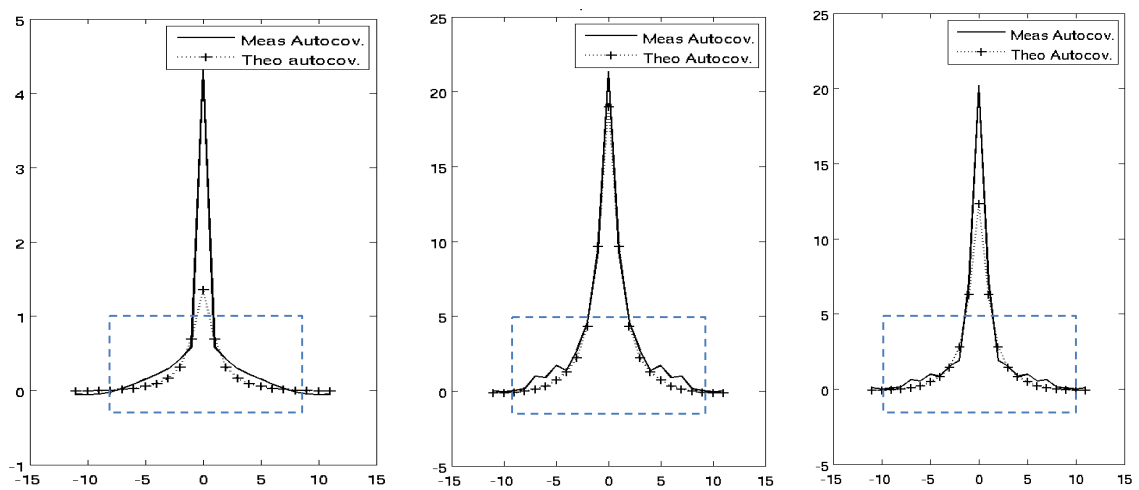


Figure 8-5: Right Wind Profiler results, for baseline WFS0&2 and WFS4&0 (Low Resolution). Left and center: temporal cross-correlation for $t=0s$, and $t=25s$.

In Figure 8-5, it can be seen that with the time the strong point of the correlation starts to fade, looking as if the turbulence is spreading out as it starts moving away from the center. This corresponds to the high peak at around 12 km, which could be attributed to the jet stream, known to be located between 7-16 km (Miller, Gans, & Kleidon, 2011). After analyzing all the data, we found that the profile of the covariance map on the real data sometimes presented a weird shape. Deeper study led us to conclude that this was probably due to a non-Kolmogorov turbulence.



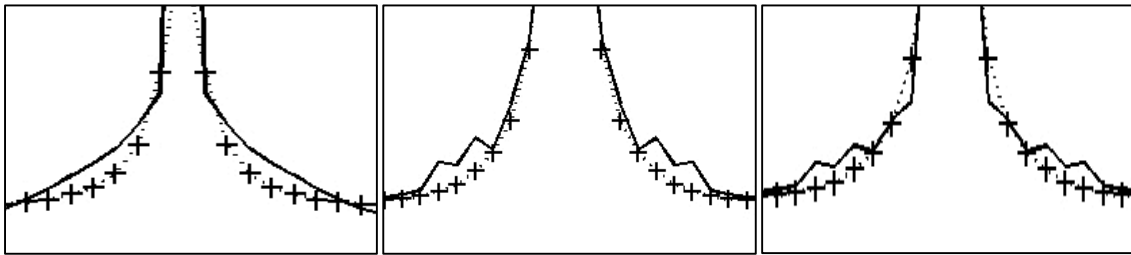


Figure 8-6: Top: Covariance submap section, where the non-Kolmogorov shape can be seen. Files observed on: (left) Nov 28th 2011 at 11:44, (middle) Dec 13th 2011 at 00:30 and (right) Dec 14th 2011 at 00:01. Bottom: zoom of the same data.

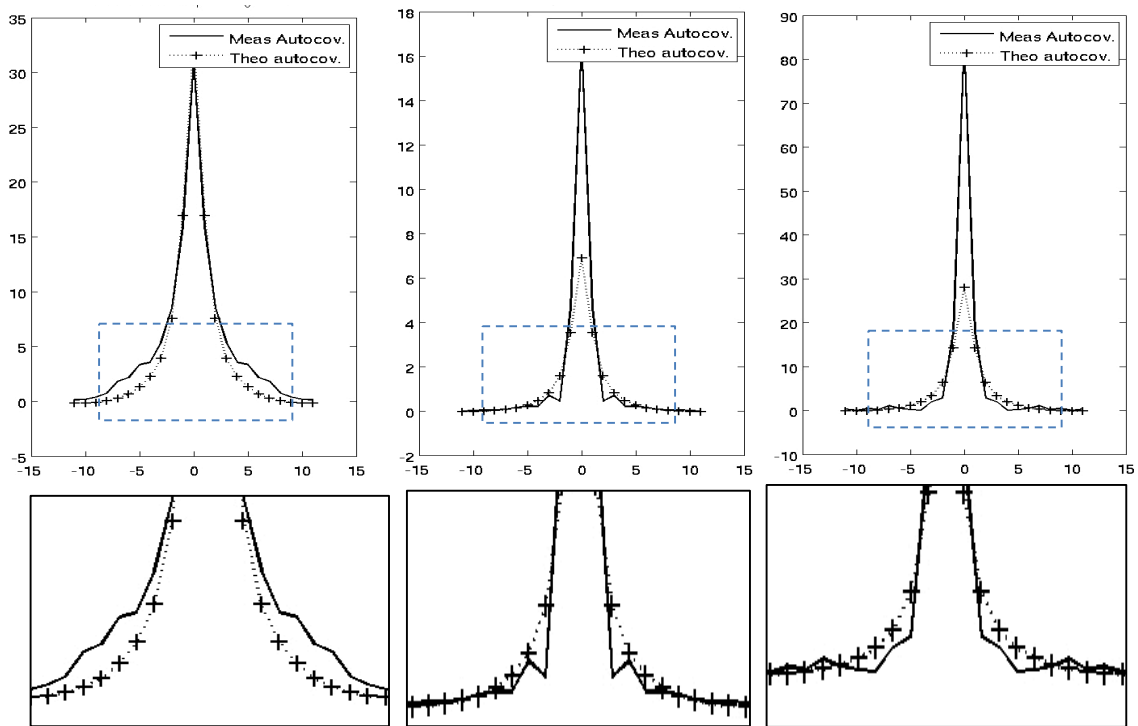


Figure 8-7: Top: Covariance submap section, where the non-Kolmogorov shape can be seen. This generated a problem for the fit, creating some negative values in the layers profile to compensate for this weird shape. Files observed on: (left) Dec 14th 2011 at 04:35, (middle) Dec 14th 2011 at 23:59 and (right) Feb 10th 2012 at 20:53. Bottom: zoom of the same data.

Figure 8-6 and Figure 8-7, show covariances results obtained from non-Kolmogorov turbulence can be seen. One can note that they don't all have the same shape, but most of them correspond to a decrease of the impulse response followed by an small increase in the wings, like both graph located in the middle show. The non-Kolmogorov data represented around 50% of the ones analyzed during this research. The dome turbulence is known to correspond to Kolmogorov turbulence, so it could be

interesting to correlate these data with the wind speed of a measurement external to the telescope dome.

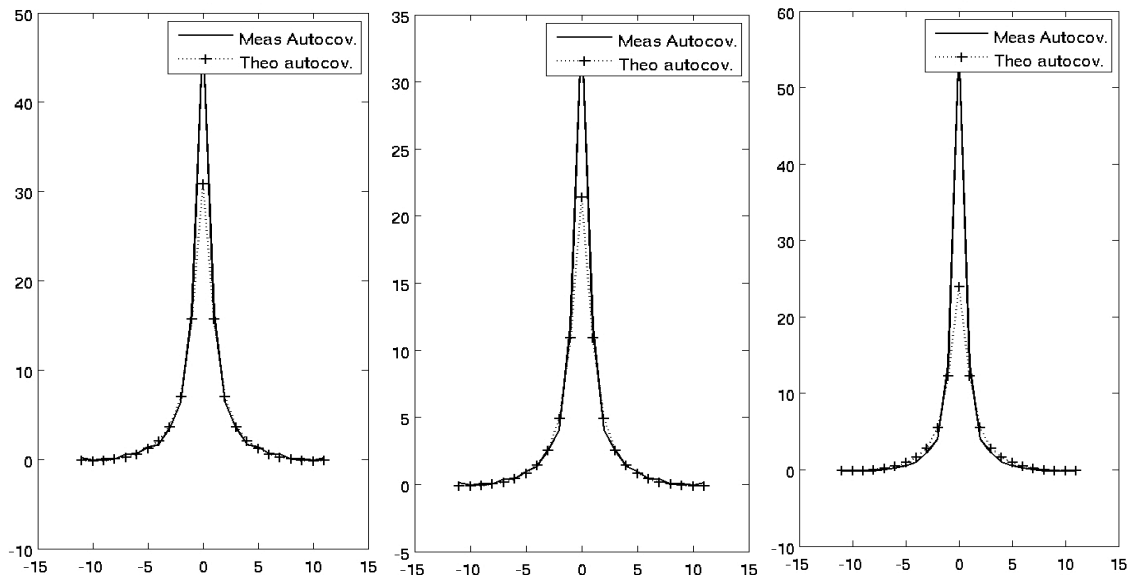


Figure 8-8: Examples of good profiles. When the covariance submap had this shape, the wind profiler had no problems finding a good fit. For these cases, we can say that the turbulence follows a Kolmogorov model.

When we obtained covariance submaps as presented in Figure 8-8, getting the profile did not present any problems (as negative values for examples). Through the analysis, we realized that it was important to look particularly at this section of the covariance submap, but also at the entire covariance submap, to get a general status of the system. Examples of submap check can be seen on Figure 8-9. The left image is a good case for comparison. The one in the middle had a very strong noise, so the autocorrelation presents a very high peak that makes the other values disappear. The right image has very weak values for all the cross-correlation with the WFS4, which could be due a problem with these WFS or the corresponding LGS.

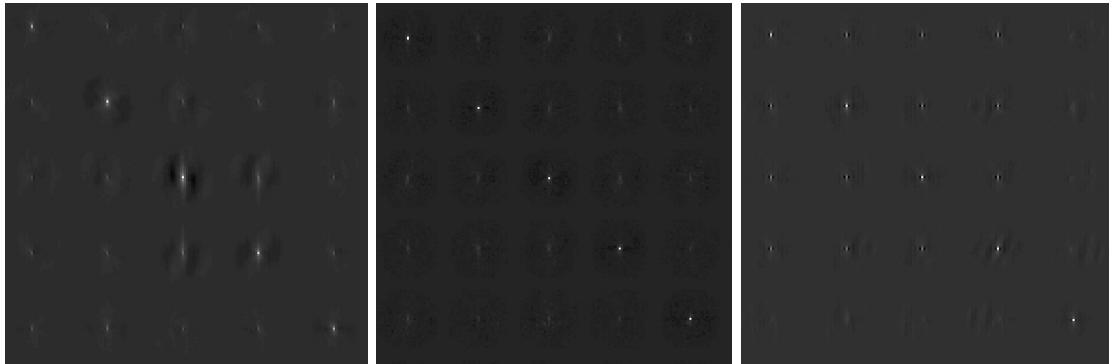


Figure 8-9: Different covariance maps, left corresponds to a normal map, the one in the center shows a very high value at the center that represent strong noise, and the one at the right presents a problem with the WFS4 (bottom left corner).

We concluded that it was important to look deeply at the values obtained to determine if we could utilize the data for the analysis. This was possible by the fact that the algorithm behaved as expected, giving two kinds of results: Kolmogorov turbulence with a nice profile, and the non-Kolmogorov turbulence with some negative values in the profile.

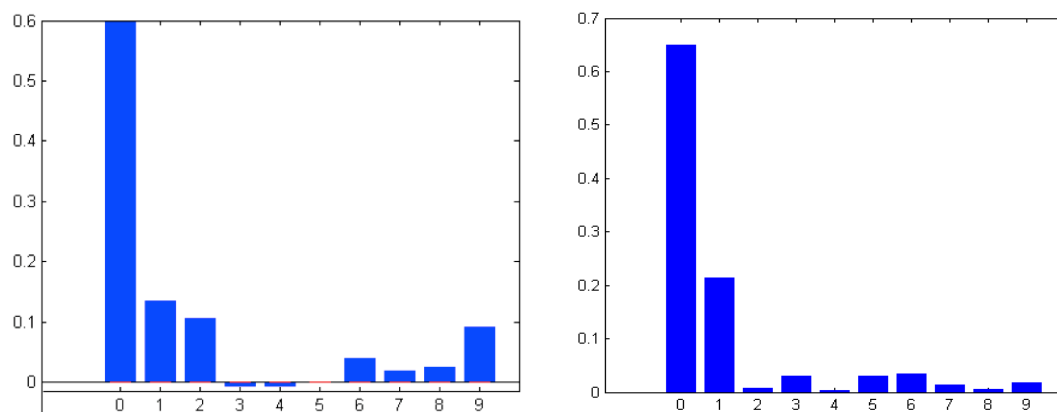


Figure 8-10: Left: Fitting of on-sky data from March 23rd 2011 at 02:26, CB close loop. Right: Fitting of on-sky data from March 27th 2011 at 01:02, best on-sky set. The values on the x axis correspond to the number of the layer.

Figure 8-10 and Figure 8-11 shows the profile obtained from good data, as it can be seen, the image on the left, had two small negative values, but this mean only a small difference in the shape of the covariance map. We also can see, is common to see some turbulence at high altitude, corresponding probably to the jet stream.

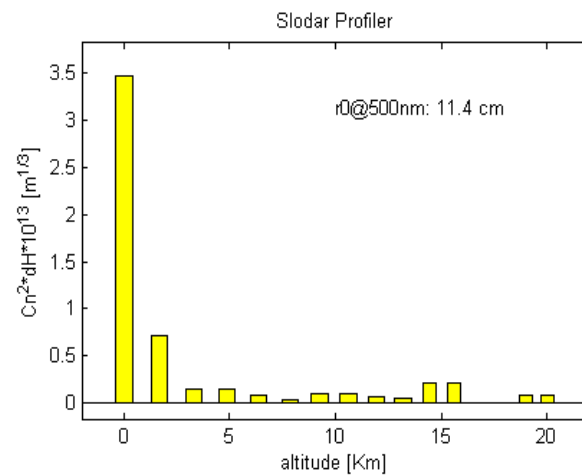


Figure 8-11: Good Profile example: here we have a strong turbulence in the ground layers that decay rapidly with the altitude giving a Fried parameter of 11.4 cm.

8.1 Results and discussion

First, we compared the results of the fit between RTD data and CB data, as the data were different in sampling and frequency. As the data were sampled at different moments, we could not perform a perfect comparison, but by taking data close enough in time we conclude that using one set or the other had no big impact on the results. Figure 8-12 and Figure 8-13 correspond to RTD data from two different moments close in time, and Figure 8-14 correspond to CB data. No important or perceptible effects were observed by using one kind of data or the other.

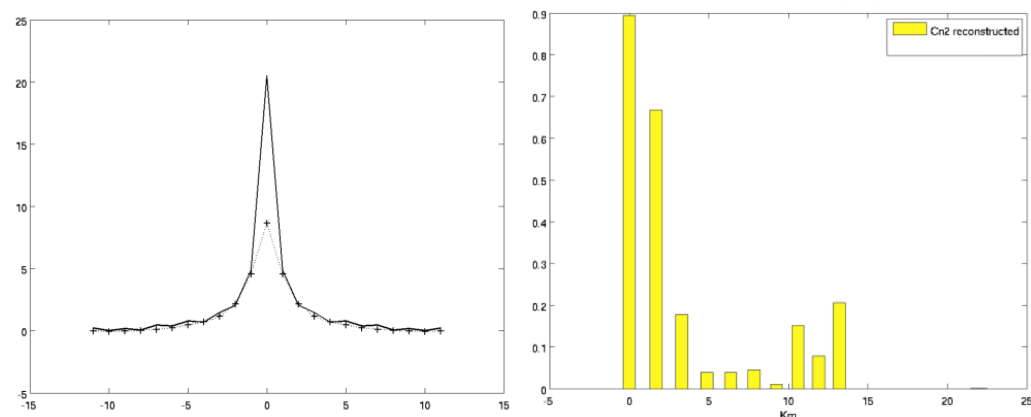


Figure 8-12: Left: central slice of the theoretical and measured submap X direction. Right: Estimated profile. RTD data, Jan 12th 2012 – 03:10:43.

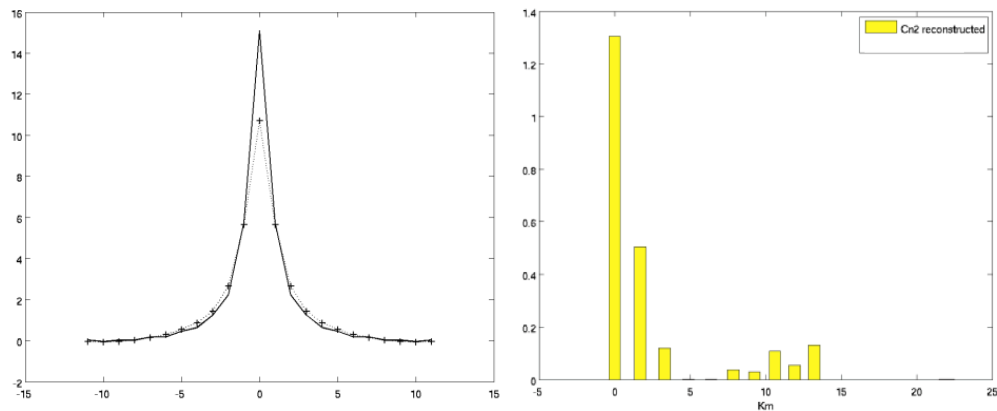


Figure 8-13: Left: central slice of the theoretical and measured submap X direction. Right: Estimated profile (good measurement here). RTD data, Jan 12th 2012 at 03:12:30.

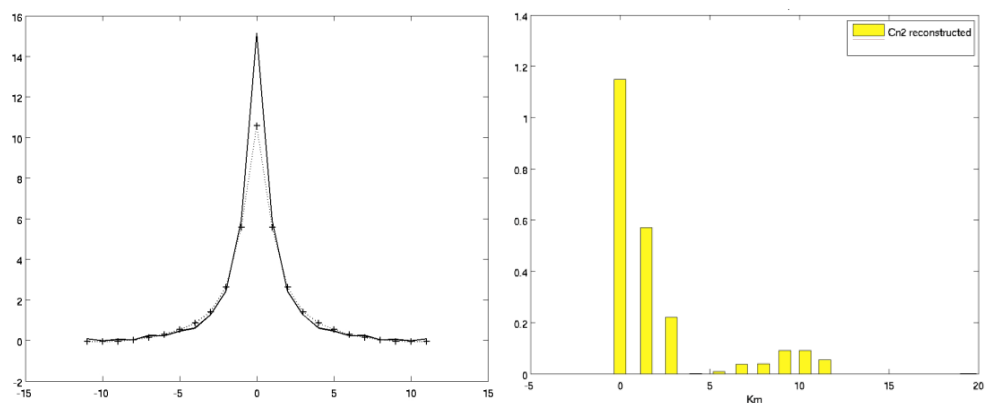


Figure 8-14: Left: central slice of the theoretical and measured submap X direction. Right: Estimated profile (good measurement here). CB data, Jan 12th 2012 at 00:12:27.

8.2 Good and bad profiles

In general, an average good profile for Gemini South, estimated with the SLODAR technique, and the GeMS data, will be close to the one presented in Figure 8-11, with a strong turbulence at the ground layer and some energy in the turbulence around 15 km above the telescope.

We also found that this data analysis allows to detect the existence of potential problems in the system. By looking at the shape of the autocorrelation submaps for every WFS, non-standard forms will appear. Examples of this behavior are shown in Figure 8-15, Figure 8-6 and Figure 8-7.

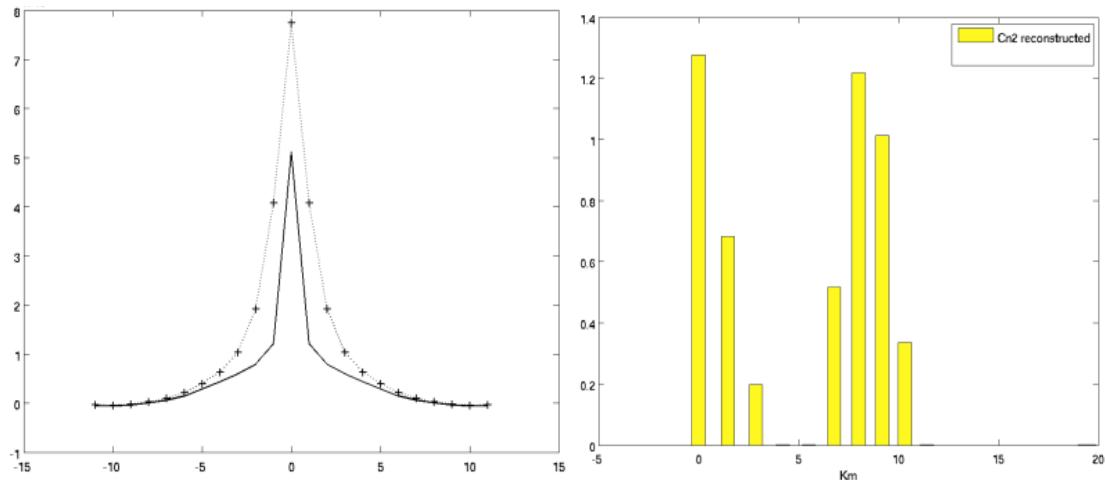


Figure 8-15: Weird data, observed on November 15th 2011 at 20:29. Left: Cross section of the autocovariance submap, Right: Obtained profile.

8.3 Validation of the techniques

One of the frequently asked questions about this work when it was presented in conferences was the comparison of the profiles obtained with this method to the ones obtained with other types of instrument and methods i.e. cross validation of the techniques. The only available option for comparison was a MASS/DIMM, located near Gemini South. The comparison was complicated by the fact that the MASS/DIMM only measured 8 layers of turbulence and did not measure the turbulence below 500 meters. But the bigger problem was that we had no control on the target observed by the different instruments, so both telescopes were observing different stars at different areas in the sky. Then, considering the dome turbulence, and positioning on the sky, it cannot be expected to have similar results.

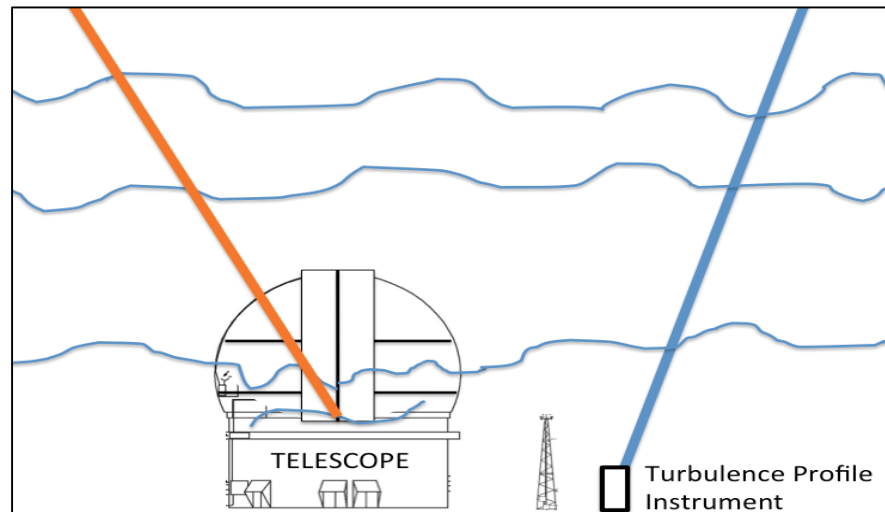


Figure 8-16: Gemini Telescope pointing in one direction (orange line), and MASS/DIMM pointing in another direction (blue line), showing how different the sampled turbulence could be, even being at close location.

Although not exhaustive, a short qualitative comparison was carried out with MASS/DIMM data, despite the different altitudes of the layers, the different resolutions, and the difference of pointing direction in the sky. It was suggested to carry out comparisons using the accumulative profile whose description follows. However due to the limited scope of this analysis, no final conclusions can be drawn and further work is required in the future

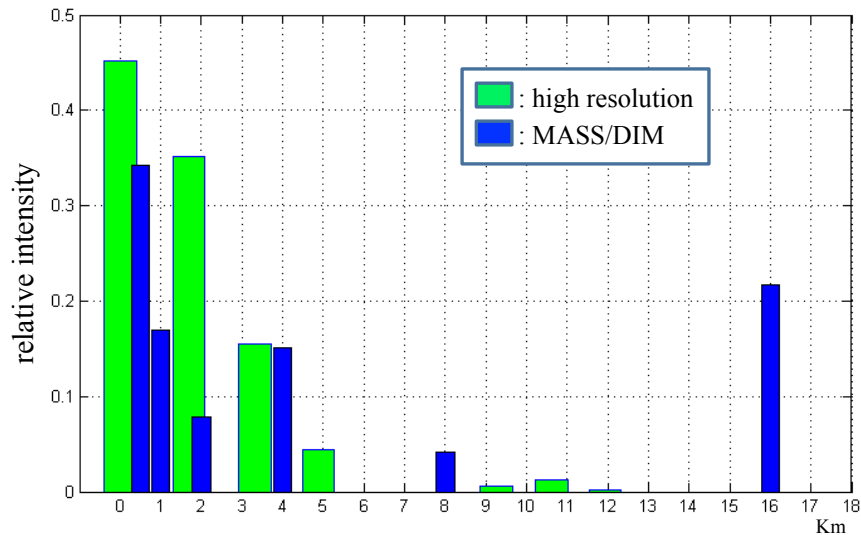


Figure 8-17: Comparison between MASS/DIM accumulative profile and spatial cross-correlation High Resolution accumulative profile. They show a good agreement at lower layers. But it is important to mention that they were observing different stars on sky. Data from April 15th, 2011, 23:55.

Finally the most reasonable comparison that we were able to perform, was using the same data set with the two different methods presented in this thesis. In general terms, it can be said that both methods perform similarly under well-behaved turbulence that is turbulence with Kolmogorov or Von-Karman statistics. For other types of statistics describing this phenomenon, we found that they can differ substantially. Take for instance Figure 8-18, where profiles are computed for turbulence having a strong dome seeing. Due to the dependence of the SLODAR approach on the assumed model (Kolmogorov or Von-Karman), a distorted profile is obtained; having even negative values. On the contrary, the wind profiler approach shows a much more robust performance. The explanation for this is it uses the measured slopes to estimate the characteristics of the turbulence; specifically by computing the autocorrelation of the slopes, which contain not only the information about the seeing but also on the outer scale (L_0) of the turbulence.

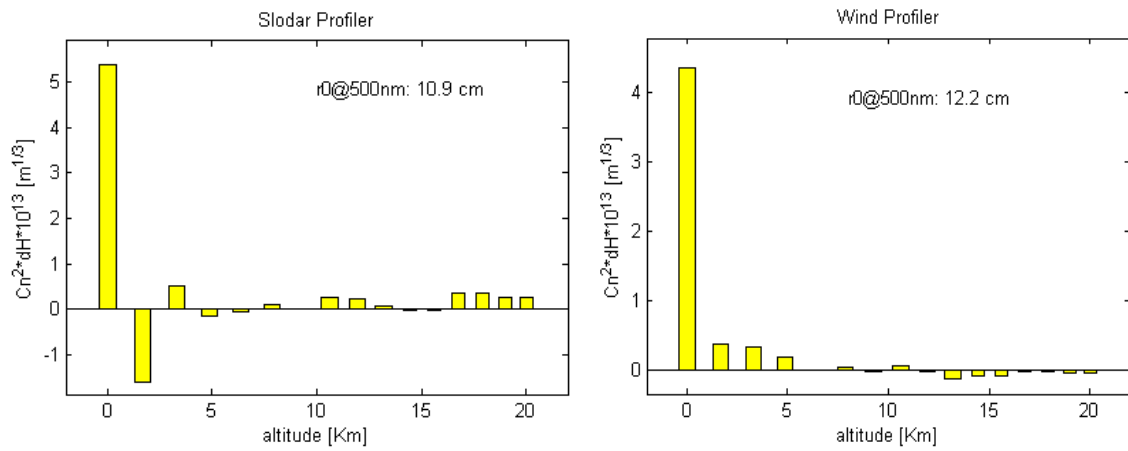


Figure 8-18: Comparison between the profiler obtained with the SLODAR method (left), and obtained with the Wind Profiler (right).

9. CONCLUSIONS AND FUTURE WORK

From the analysis made with the two profilers, we can conclude that it is possible to obtain the turbulence profile using LGSs, and the method embedded in a MCAO system.

If we agree on the importance of studying the universe, then knowing the limitations of the technical and economic resources imposed on the scientific community, we must understand that for the moment looking to the sky is, in most cases, restricted to ground based telescopes. Then a tool that corrects for atmospheric aberrations is mandatory and the answer is adaptive optics. For the new generation of telescopes and instruments, we will need to perform these corrections as fast as possible and covering the biggest field of view possible. The key for future astronomical instruments demand probing the turbulence, characterizing it and being able to compensate its negative effects fast and effectively. Currently, two paths are followed in the studies of the atmosphere: measuring it in a very fast and accurate way, and predicting its behavior and evolution by modeling.

The work presented here was focused on measuring the turbulence using the available resources in a more optimal way. We proposed to use a method derived from SLODAR, an instrument developed for turbulence profiling. Similar methods have been developed based on the use of natural guide stars, but we develop an algorithm using laser guide stars, adapted to be used with the GeMS AO facility located in the Gemini South 8-meter telescope.

For validation of the results, we compared the SLODAR based profiling with another method called “wind profiler”. Both methods were tested for the data sets but the latter also provides the wind speed and direction of every layer above the telescope. Using these two independent methods allowed us to validate our results via cross-checking the profiles obtained.

The simulation process was used to develop and validate the process, the results obtained with the simulations were consistent with the theory. In the second phase of analyzing the instrument data, we could determine the parameters limiting the quality of the analysis. We first started eliminating the non-valid sub-apertures either excessive or unrealistically low values for the standard deviation of the measured slopes. We also developed a process to select only the useful data sets, i.e. ensuring that they were taken with adequate observing conditions to deliver meaningful results.

Having the LGS launched from behind the M2 as in the system used is responsible for the fratricide effect, resulting in losing 224 sub-apertures (approximately 20% of the total). This effect can be avoided with a design where the LGS are launched from the edge of the primary mirror.

An important result of the method is its ability to determine the existence of dome seeing together with its strength, a result which was developed further in another study (Guesalaga et al., 2014).

Another important outcome was the analysis of the shape of the covariance map, giving us an idea of how it resembles a Kolmogorov one. A good future work to follow-up on this result would be to develop a model of turbulence fitting the actual measured shape of the covariance map.

It was observed that only about half of the time Kolmogorov turbulence was observed. This could be explained by the presence of a strong dome seeing that we could also observe in the analysis. A study between the appearance of non-Kolmogorov turbulence and dome seeing should be studied in-depth, so its use on the design and testing of the dome structure can also be considered in the future. In the future this could also be correlated with the wind speed to study the importance of the dome construction and the ventilation design.

Statistical analysis should also become a standard function in regular operations, determining the effect of season and wind parameters on turbulence and performance of the AO system. Statistical studies have only been

performed on a limited scale (Rodríguez et al., 2014). To perform this study on a permanent basis, one will need to define a process and conditions of recording to ensure the validity of all measurements for the study.

An important contribution of this thesis to the astronomical instrumentation community is that its results and associated code are currently being implemented in other important projects of wide field adaptive optics that use multiple guide stars, such as Raven (Correia et al., 2014), MMT (Milton, Lloyd-Hart, Bernier, & Baranec, 2007), AOF-VLT (Valenzuela, Garcia-risssmann, Gonte, Mackenna, & Curie, 2014) and the ARGOS system (Mazzoni, Busoni, & Esposito, 2014).

The most important conclusion to be drawn from this thesis is that a better knowledge of the foes to adaptive optics is required. The key for the future designs of these instruments is the understanding of the turbulence, the characterization of the sites where the telescopes will be constructed. This will allow to feed-forward turbulence information to the control system in order to optimize the correction of the incoming light waves.

BIBLIOGRAPHY

Ashcroft, D. (2013). *Space Exploration: All That Matters* (p. 160). Hodder & Stoughton.

Assémat, F., Wilson, R., & Gendron, E. (2006). Method for simulating infinitely long and non stationary phase screens with optimized memory storage. *Optics Express*, *14*(3), 988–99. Retrieved from <http://www.ncbi.nlm.nih.gov/pubmed/19503419>

Babcock, H. W. (1953). The Possibility of Compensating Astronomical Seeing. *Publications of the Astronomical Society of the Pacific*, *65*, 229. doi:10.1086/126606

Bec, M., Rigaut, F. J., Galvez, R., Arriagada, G., Boccas, M., Gausachs, G., ... Vucina, T. (2008). The Gemini MCAO bench: system overview and lab integration Matthieu, *7015*(2008), 701568–701568–13. doi:10.1117/12.790354

Boreman, G. D., & Dainty, C. (1996). Zernike expansions for non-Kolmogorov turbulence. *Journal of the Optical Society of America A: Optic*, *13*(3), 517–522. doi:10.1364/JOSAA.13.000517

Butterley, T. (2006). *Laser Guide Stars and Turbulence Profiling for Extremely Large Telescopes Extremely Large Telescopes*. University of Durham.

Butterley, T., Wilson, R. W., & Sarazin, M. (2006). Determination of the profile of atmospheric optical turbulence strength from SLODAR data. *Monthly Notices of the Royal Astronomical Society*, *369*(2), 835–845. doi:10.1111/j.1365-2966.2006.10337.x

Campbell, M. (2009). Atmospheric Turbulence and its Influence on Adaptive Optics. Retrieved from http://www.roe.ac.uk/ifa/postgrad/pedagogy/2008_campbell.pdf

Celik, I. (1999). Introductory turbulence modeling. *Western Virginia University*, (December), 94. Retrieved from http://www.fem.unicamp.br/~im450/palestras&artigos/ASME_Tubulence/cds13workbook.pdf

Correia, C., Jackson, K., Véran, J.-P., Andersen, D., Lardièrre, O., & Bradley, C. (2014). Static and predictive tomographic reconstruction for wide-field multi-object adaptive optics systems. *Journal of the Optical Society of America. A, Optics, Image Science, and Vision*, *31*(1), 101–13. Retrieved from <http://www.ncbi.nlm.nih.gov/pubmed/24561945>

Cortes, A., Neichel, B., Guesalaga, A., Osborn, J., Rigaut, F., & Guzman, D. (2012). Atmospheric turbulence profiling using multiple laser star wavefront sensors. *Monthly Notices of the Royal Astronomical Society*, 427, 2089–2099. Retrieved from <http://mnras.oxfordjournals.org/content/427/3/2089.full.pdf>

David G. Andrews. (2010). *An Introduction to Atmospheric Physics* (Second Edi., p. 248). Cambridge University Press. Retrieved from http://www.cambridge.org/gb/knowledge/isbn/item2712587/?site_locale=en_GB

Ellerbroek, B. L. (2003). MCAO for Gemini South. *Proceedings of SPIE*, 4839, 55–66. doi:10.1117/12.459692

ESA. (n.d.). Hubble History: The Spherical Aberration Problem. Retrieved February 05, 2004, from http://www.spacetelescope.org/about/history/aberration_problem/

ESO. (n.d.). FAQ VLT/Paranal. Retrieved February 05, 2014, from <https://www.eso.org/public/about-eso/faq/faq-vlt-paranal/#25>

Fried, D. (1975). Differential angle of arrival: theory, evaluation, and measurement feasibility. *Radio Science*, 10(1), 71–76. Retrieved from <http://onlinelibrary.wiley.com/doi/10.1029/RS010i001p00071/full>

Fried, D. L. (1990). Greenwood frequency measurements. *Journal of the Optical Society of America A*, 7(5), 946. doi:10.1364/JOSAA.7.000946

García-Lorenzo, B., & Fuensalida, J. J. (2011). Atmospheric optical turbulence at the Roque de los Muchachos Observatory: data base and recalibration of the generalized SCIDAR data. *Monthly Notices of the Royal Astronomical Society*, 416(3), 2123–2129. doi:10.1111/j.1365-2966.2011.19186.x

Golub, G., & Loan, C. Van. (1980). An analysis of the total least squares problem. *SIAM Journal on Numerical Analysis*, 17, 883–893. Retrieved from <http://epubs.siam.org/doi/abs/10.1137/0717073>

Gratadour, D., & Rigaut, F. (2007). Online Centroid Gain Determination for LGS AO Systems. In *Adaptive Optics: Analysis and Methods/Computational Optical Sensing and Imaging/Information Photonics/Signal Recovery and Synthesis Topical Meetings on CD-ROM, OSA Technical Digest (CD) (Optical Society of America, 2007)* (p. PMA4). Washington, D.C.: Osa. doi:10.1364/AOPT.2007.PMA4

Guesalaga, A., Neichel, B., Cortes, A., Bechet, C., & Guzman, D. (2014). Using the Cn2 and wind profiler method with wide-field laser-guide-stars adaptive optics to

quantify the frozen-flow decay. *Monthly Notices of the Royal Astronomical Society*, 440(3), 1925–1933. doi:10.1093/mnras/stu366

Hardy, J. W. (1998). *Adaptive Optics for Astronomical Telescopes*. Oxford University Press. Retrieved from http://books.google.cl/books?id=-0aAWyckS_8C

Hecht, E. (2002). *Optics* (4th Editio., p. 704). San Francisco: Addison Wesley.

Johnston, R., Dainty, C., Wooder, N., & Lane, R. (2002). Generalized scintillation detection and ranging results obtained by use of a modified inversion technique. *Applied Optics*, 41(32), 6768–6772. Retrieved from <http://www.opticsinfobase.org/abstract.cfm?uri=ao-41-32-6768>

Karman, T. Von. (1937). On the statistical theory of turbulence. *Proceedings of the National Academy of Sciences ...*, 98–105. Retrieved from <http://www.ncbi.nlm.nih.gov/pmc/articles/PMC1076876/>

Kolmogorov, A. N. (1941). The local structure of turbulence in incompressible viscous fluid for very large Reynolds numbers. *Doklady Akademii Nauk Ssr*, 30(1890), 301–305. doi:10.1098/rspa.1991.0075

Lallo, M. D. (2012). Experience with the Hubble Space Telescope: 20 years of an archetype. *Optical Engineering*, 51(1), 011011. doi:10.1117/1.OE.51.1.011011

Linnik, V. P. (1994). On the Possibility of Reducing the Influence of Atmospheric Seeing on the Image Quality of Stars. In Merkle (Ed.), *European Southern Observatory Conference and Workshop Proceedings* (pp. 535–537). Retrieved from <http://adsabs.harvard.edu/abs/1994ESOC...48..535L>

Lukin, V., Fortes, B., & Physicist, M. (2002). *Adaptive beaming and imaging in the turbulent atmosphere* (p. 2011). Washington, D.C.: SPIE. Retrieved from http://spie.org/x648.html?pf=true&product_id=452443&origin_id=x23271

Marchetti, E., Brast, R., Delabre, B., Donaldson, R., Fedrigo, E., Frank, C., ... Bagnara, P. (2007, September). On-sky Testing of the Multi-Conjugate Adaptive Optics Demonstrator. *ESO Messenger*, 129(September), 8–13. Retrieved from <https://www.eso.org/sci/publications/messenger/archive/no.129-sep07/messenger-no129-8-13.pdf>

Masciadri, E., & Vernin, J. (1997). Optical technique for inner-scale measurement: possible astronomical applications. *Applied Optics*, 36(6), 1320–7. Retrieved from <http://www.ncbi.nlm.nih.gov/pubmed/18250806>

Mazzoni, T., Busoni, L., & Esposito, S. (2014). Implementation of SLODAR atmospheric turbulence profiling to the ARGOS system. In *SPIE* (pp. 9148–9245).

McGlamery, B. (1976). Computer simulation of atmospheric turbulence and compensated imaging systems. ... *Opt. Propagation in the Atmosphere 17 P (SEE ...*, V, 225–233. Retrieved from <http://adsabs.harvard.edu/abs/1976opa..agarS....M>

Miller, L. M., Gans, F., & Kleidon, a. (2011). Jet stream wind power as a renewable energy resource: little power, big impacts. *Earth System Dynamics Discussions*, 2(1), 435–465. doi:10.5194/esdd-2-435-2011

Milton, N. M., Lloyd-Hart, M., Bernier, J. a., & Baranec, C. (2007). Real-time atmospheric turbulence profile estimation using modal covariance measurements from multiple guide stars. In R. K. Tyson & M. Lloyd-Hart (Eds.), *SPIE, Astronomical Adaptive Optics System and Applications III* (Vol. 6691, p. 66910B–66910B–9). doi:10.1117/12.734377

Morris, T. J. (2005). *An Experimental Rayleigh Laser Guide Star Ground Layer Adaptive Optics System for the William Herschel Telescope*. University of Durham.

Neichel, B., Rigaut, F., Serio, A., Arriagada, G., Boccas, M., D’Orgeville, C., ... Diaz, H. (2012). Science readiness of the Gemini MCAO system: GeMS. In B. L. Ellerbroek, E. Marchetti, & J.-P. Véran (Eds.), (p. 84470W–84470W–24). doi:10.1117/12.925915

Osborn, J. (2010). *Profiling the turbulent atmosphere and novel correction techniques for imaging and photometry in astronomy*. Durham University. Retrieved from <http://ethos.bl.uk/OrderDetails.do?uin=uk.bl.ethos.524848>

Owens, J. C. (1967). Optical refractive index of air: dependence on pressure, temperature and composition. *Applied Optics*, 6(1), 51–9. Retrieved from <http://www.ncbi.nlm.nih.gov/pubmed/20057695>

Rigaut, F., & Neichel, B. (2011). GeMS sees star light. *AO4ELT2*, 10. Retrieved from <http://ao4elt2.lesia.obspm.fr/sites/ao4elt2/IMG/pdf/073rigaut.pdf>

Rigaut, F., & Neichel, B. (2012). GeMS: first on-sky results. *SPIE ...*, (January 2011). Retrieved from <http://proceedings.spiedigitallibrary.org/proceeding.aspx?articleid=1358879>

Rocca, A., Roddier, F., & Vernin, J. (1974). Detection of atmospheric turbulent layers by spatiotemporal and spatioangular correlation measurements of stellar-light

scintillation. *JOSA*, 64(7), 1000–1004. Retrieved from <http://www.opticsinfobase.org/abstract.cfm?uri=josa-64-7-1000>

Roddier, C., & Roddier, F. (1975). Influence of exposure time on spectral properties of turbulence-degraded astronomical images. *JOSA*, 65(6), 664–667. Retrieved from <http://www.opticsinfobase.org/abstract.cfm?uri=josa-65-6-664>

Roddier, F. (1981). The effects of atmospheric turbulence in optical astronomy. *Progress in Optics.*, 19, 281–376. doi:10.1016/S0079-6638(08)70204-X

Roddier, F. (1999). *Adaptive Optics in Astronomy*. (F. Roddier, Ed.). Cambridge: Cambridge University Press. doi:10.1017/CBO9780511525179

Rodríguez, I., Neichel, B., Béchet, C., Guzmán, D., Guesalaga, A., Université, A. M., ... Umr, D. M. (2014). Statistics of atmospheric turbulence at Cerro Pachon using the GeMS profiler. In *SPIE* (pp. 9148–9240).

Saint-Jacques, D. (1998). *Astronomical seeing in space and time*. University of Cambridge. Retrieved from <http://scholar.google.com/scholar?hl=en&btnG=Search&q=intitle:Astronomical+Seeing+in+Space+and+Time#0>

Sarazin, M., & Roddier, F. (1990). The ESO differential image motion monitor. *Astronomy and Astrophysics*, 227, 294–300. Retrieved from <http://adsabs.harvard.edu/full/1990A&A...227..294S>

Schmidt, J. D. (2010). *Numerical Simulation of Optical Wave Propagation with Examples in MATLAB* (p. 201). 1000 20th Street, Bellingham, WA 98227-0010 USA: SPIE. doi:10.1117/3.866274

Schöck, M. (1998). *An Analysis of Turbulent Layers with a Wave Front Sensor*. The University of Wyoming.

Schöck, M., Le Mignant, D., Chanan, G. a, Wizinowich, P. L., & van Dam, M. a. (2003). Atmospheric turbulence characterization with the Keck adaptive optics systems. I. Open-loop data. *Applied Optics*, 42(19), 3705–20. Retrieved from <http://www.ncbi.nlm.nih.gov/pubmed/12868804>

Schöck, M., & Spillar, E. (2000). Method for a quantitative investigation of the frozen flow hypothesis. *Journal of the Optical Society of America. A, Optics, Image Science, and Vision*, 17(9), 1650–8. Retrieved from <http://www.ncbi.nlm.nih.gov/pubmed/10975375>

Schöck, M., & Spillar, E. J. (1999). An analysis of turbulent atmospheric layers with a wave front sensor : Testing the frozen flow hypothesis. In *Proc. SPIE 3762, Adaptive Optics Systems and Technology*, 225 (September 27, 1999) (Vol. 3762). doi:10.1117/12.363577

Serabyn, E., Wallace, K., Troy, M., Mennesson, B., Haguenaer, P., Gappinger, R., & Burruss, R. (2007). Extreme Adaptive Optics Imaging with a Clear and Well-Corrected Off- Axis Telescope Subaperture. *The Astrophysical Journal*, 658(2), 1386–1391. doi:10.1086/511949

Shepherd, H. (2012). *Turbulence characterisation for Astronomical Observatories*. Durham University.

Shimizu, M., Yoshimura, S., Tanaka, M., & Okutomi, M. (2008). Super-resolution from image sequence under influence of hot-air optical turbulence. *2008 IEEE Conference on Computer Vision and Pattern Recognition*, 1–8. doi:10.1109/CVPR.2008.4587525

Shöck, M. (1998). *An Analysis of Turbulent Layers with a Wave Front Sensor*. The University of Wyoming.

Tatarskii, V. (1961). *Wave propagation in turbulent medium*. (I. Dover Publications, Ed.) *Wave Propagation in Turbulent Medium, by ...* (p. 154). New York. Retrieved from <http://adsabs.harvard.edu/abs/1961wptm.book.....T>

Tatarskii, V. I. (1971). *The effects of the turbulence atmosphere on wave propagation* (p. 482). Jerusalem: IPST.

Taylor, G. (1938). The spectrum of turbulence. *Proceedings of the Royal Society of ...* Retrieved from <http://rspa.royalsocietypublishing.org/content/164/919/476.full.pdf>

Tokovinin, A. (2004). New instruments to see the “seeing.” *NOAO/NSO Newsletter* 77, (77), 32–34. Retrieved from <http://www.ctio.noao.edu/~atokovin/profiler/massdimm.pdf>

Tokovinin, A., Bustos, E., & Berdja, A. (2010). Near-ground turbulence profiles from lunar scintillometer, *I2*(January), 1–12.

Tokovinin, A., Kellerer, A., & Coudé Du Foresto, V. (2008). FADE, an instrument to measure the atmospheric coherence time. *Astronomy and Astrophysics*, 477(2), 671–680. doi:10.1051/0004-6361:20077996

Tyson, R. (2011). *Principles of Adaptive Optics*. (T. & F. Group, Ed.) *Contemporary Physics* (3rd ed., p. 314). CRC Press. Retrieved from <http://www.tandfonline.com/doi/abs/10.1080/00107514.2011.583687>

Valenzuela, J., Garcia-rissmann, A., Gonté, F., Mackenna, V., & Curie, J. (2014). Turbulence Profiling Methods Applied to ESO's Adaptive Optics Facility. In *SPIE* (pp. 9148–9166).

Van der Laan, H., Ardeberg, A., Vernin, J., Weigelt, G., & Wohl, H. (1986). *SITE TESTING FOR THE VLT, Data Analysis Part I: Seeing* (p. 94). Retrieved from http://www.eso.org/sci/libraries/historicaldocuments/VLT_Reports/VLTrep55.pdf

Vernin, J., & Pelon, J. (1986). Scidar/lidar description of a gravity wave and associated turbulence: preliminary results. *Applied Optics*, 25(17), 2874. Retrieved from <http://www.ncbi.nlm.nih.gov/pubmed/18235545>

Vernin, J., & Roddier, F. (1973). Experimental determination of two-dimensional spatiotemporal power spectra of stellar light scintillation. Evidence for a multilayer structure of the air turbulence in the upper troposphere. *JOSA*, 63(3), 270–273. Retrieved from <http://www.opticsinfobase.org/abstract.cfm?uri=josa-63-3-270>

Vidal, F., Gendron, E., Brangier, M., Sevin, a., Rousset, G., & Hubert, Z. (2010). Tomography reconstruction using the Learn and Apply algorithm. *1st AO4ELT Conference - Adaptive Optics for Extremely Large Telescopes, 07001, 07001*. doi:10.1051/ao4elt/201007001

Wang, L. (2007). *Atmospheric Turbulence Profiling using Multiple Adaptive Optics Wavefront Sensors*. University of California, Irvine. Retrieved from <http://www.mendeley.com/profiles/lianqi-wang1/>

Wang, L., Otarola, A., & Ellerbroek, B. (2010). Impact of sodium laser guide star fratricide on multi-conjugate adaptive optics systems. *JOSA A*, 27(11), A19–A28. Retrieved from <http://www.opticsinfobase.org/abstract.cfm?URI=josaa-27-11-A19>

Wang, L., Schöck, M., & Chanan, G. (2008). Atmospheric turbulence profiling with SLODAR using multiple adaptive optics wavefront sensors. *Applied Optics*, 47(11), 1880–92. Retrieved from <http://www.ncbi.nlm.nih.gov/pubmed/18404187>

Wang, X. (2013). *Contrôle de forme d'un miroir spatial par actionneurs piézoélectriques*. Université de Toulouse. Retrieved from http://depozit.isae.fr/theses/2013/2013_Wang_Xuan.pdf

Wilson, R. (2002). SLODAR: measuring optical turbulence altitude with a Shack–Hartmann wavefront sensor. *Monthly Notices of the Royal Astronomical Society*, 337(1), 103–108. Retrieved from <http://onlinelibrary.wiley.com/doi/10.1046/j.1365-8711.2002.05847.x/full>

Wilson, R., & Jenkins, C. (1996). Adaptive optics for astronomy: theoretical performance and limitations. *Monthly Notices of the Royal ...* Retrieved from <http://mnras.oxfordjournals.org/content/278/1/39.short>

Wilson, R. W., Butterley, T., & Sarazin, M. (2009). The Durham/ESO SLODAR optical turbulence profiler. *Monthly Notices of the Royal Astronomical Society*, 399(4), 2129–2138. doi:10.1111/j.1365-2966.2009.15409.x

Zou, W., & Rolland, J. P. (2006). Quantifications of error propagation in slope-based wavefront estimations. *Journal of the Optical Society of America. A, Optics, Image Science, and Vision*, 23(10), 2629–38. Retrieved from <http://www.ncbi.nlm.nih.gov/pubmed/16985547>